

Evaluation of Spatial-Spectral Filtering in Non-Paraxial
Volume Holographic Imaging Systems

by

Jonathan M. Watson

B.S., University of Wisconsin at Eau Claire (2004)
B.M.E., University of Minnesota (2004)

Submitted to the Department of Mechanical Engineering
in partial fulfillment of the requirements for the degree of

Master of Science

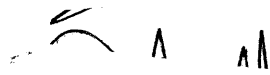
at the

MASSACHUSETTS INSTITUTE OF TECHNOLOGY


June 2008

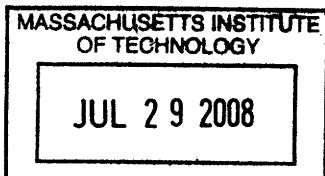
© 2008 Massachusetts Institute of Technology

The author hereby grants to Massachusetts Institute of Technology permission to
reproduce and
to distribute copies of this thesis document in whole or in part.

Signature of Author .. 
Department of Mechanical Engineering
9 May 2008

Certified by 
George Barbastathis
Associate Professor of Mechanical Engineering
Thesis Supervisor

Accepted by 
Professor Lallit Anand
Chairperson, Department Committee on Graduate Students



ARCHIVES

Evaluation of Spatial-Spectral Filtering in Non-Paraxial Volume Holographic Imaging Systems

by

Jonathan M. Watson

Submitted to the Department of Mechanical Engineering
on 9 May 2008, in partial fulfillment of the
requirements for the degree of
Master of Science

Abstract

In this thesis, the properties of transmission-mode volume phase holograms as spatial-spectral filters in optical systems for microscopic medical imaging are evaluated. In experiment, the relationship between the angle of incidence and diffraction efficiency are investigated for wavelength-detuned multiplex holograms to establish the limits of the narrow bandwidth lateral field of view. The depth selectivity of the microscope with a volume hologram pupil is also measured and found to vary significantly with recording parameters and lateral shift of the probe point source in object space. This experiment is modified to incorporate controlled levels of spherical aberration, where the effect on the depth selectivity is evaluated. A novel resolution target designed specifically for the evaluation of this imaging system is described and imaged. A flexible approach based on the 1st-order Born approximation is implemented to simulate all aspects of the imaging system with a multiplex volume hologram pupil. The simulation is then used to verify and expand upon the experimental results. A mathematical treatment of the nature of the anomalous apparent curvature of the diffraction image is performed, showing that a volume grating recorded in plane has weak out-of-plane spatial filtering behavior.

Thesis Supervisor: George Barbastathis

Title: Associate Professor of Mechanical Engineering

Contents

Acknowledgements	9
1 Introduction	10
1.1 The volume hologram and imaging	10
1.1.1 Recording volume holograms	11
1.1.2 Imaging with volume holograms	13
1.1.3 Projection of 3-D spectral data	15
1.2 A short survey of 3-D optical microscopy systems	18
1.2.1 Confocal microscopy	18
1.2.2 Two-photon microscopy	20
1.2.3 Optical coherence tomography (OCT)	20
1.2.4 Summary	22
1.3 A summary of this research	23
1.3.1 Experimental efforts	23
1.3.2 Simulation efforts	26
1.3.3 Matlab [®] and Zemax [®]	26
2 Evaluating the Performance of VHI Systems	28
2.1 Resolution target	28
2.1.1 Target design	28
2.1.2 Fabrication methods	32
2.2 Lateral point spread function	35
2.2.1 Interference terms for field reconstruction	36

2.2.2	PSF reconstruction method	38
2.3	Angular selectivity and diffraction efficiency	42
2.3.1	Experimental procedure	43
2.3.2	Results and discussion	46
2.4	Depth selectivity	52
2.4.1	Experimental procedure	53
2.4.2	Results and discussion	56
2.5	Aberrated beams and depth selectivity	63
2.5.1	Experimental procedure	65
2.5.2	Results and discussion	66
2.6	VHI micrographs	70
2.6.1	Resolution target images	70
2.6.2	Onion peel images	74
2.6.3	Image processing	74
3	Simulating VHI Systems	78
3.1	Weak diffraction and transmission volume holograms	79
3.1.1	The K-sphere	79
3.1.2	Weak diffraction	80
3.2	Weak diffraction simulation with Matlab [®] , pMatlab, and Zemax [®]	92
3.2.1	Simulation architecture and design	93
3.2.2	MDO, MZDDE, and Zemax [®]	97
3.2.3	Distributed block 2-D FFT and spatial-spectral sampling	98
3.2.4	Parallel processing with pMatlab and LLGrid	105
3.3	Simulation Study	106
3.3.1	Angular selectivity and diffraction efficiency	111
3.3.2	Aberrated beams and depth selectivity	118
3.3.3	Simulation performance	134
4	Discussion and Conclusions	138
4.1	Summary of results	138

4.2 Discussion	140
4.3 Future work	141
A Matlab[®] Code Samples	149

List of Figures

1-1	Recording geometry for volume holograms.	13
1-2	VHI system configuration.	14
1-3	Imaging broadband point sources with the VHI system.	16
2-1	CdSe-ZnS quantum dot absorption and emission spectra	31
2-2	NBS-1952 resolution target	32
2-3	Resolution pattern dimensional drawing	33
2-4	Conventional microscope image	34
2-5	Mach-Zehnder for PSF measurement	38
2-6	Interferogram and components for PSF	39
2-7	Reconstructed phase angle	40
2-8	Reconstructed lateral PSF	41
2-9	Bragg slit dimensions for lateral PSF	41
2-10	Angular selectivity experiment configuration	43
2-11	Angular selectivity curves for grating S9	47
2-12	Angular selectivity curves for grating F3A#1	47
2-13	Angular selectivity curves for grating F3A#2	48
2-14	Angular selectivity curves for grating F3B#1	48
2-15	Angular selectivity curves for grating F3B#2	49
2-16	Paraxial simulation of angular selectivity	50
2-17	Angular selectivity experiment configuration	55
2-18	Configuration of objective optics	56
2-19	Depth selectivity; F3A#1 633nm.	57

2-20	Depth Selectivity, F3A#2 633nm.	58
2-21	Depth Selectivity, F3B#1 488nm.	58
2-22	Depth Selectivity, F3B#2 488nm.	59
2-23	Depth Selectivity, F3B#1 633nm.	59
2-24	Depth Selectivity, F3B#2 633nm.	60
2-25	Depth Selectivity, F17#3 488nm.	60
2-26	Depth Selectivity, F17#3 633nm.	61
2-27	Depth Selectivity, F17 (All Gratings) 633nm.	62
2-28	Aberration experiment configuration	66
2-29	Aberrated diffraction, F3B#1.	67
2-30	Aberrated diffraction, F3B#2	67
2-31	Gain versus aberration coefficient.	69
2-32	FWHM versus aberration coefficient.	70
2-33	Resolution target position	71
2-34	Two-grating VHI image of resolution target	72
2-35	Five grating image of resolution target	73
2-36	Onion peel image	75
2-37	Defocussed object image for processing	76
2-38	3-D reconstruction of images in Fig. 2-35	77
2-39	3-D reconstruction of images in Fig. 2-36.	77
3-1	K-sphere diagram	80
3-2	Phase angle convention.	81
3-3	Simulation of Bragg-slit curvature.	91
3-4	Hologram recording geometry.	96
3-5	Schematic of the block-FFT algorithm.	100
3-6	Phase object spectra versus sample size.	102
3-7	Paraxial and non-paraxial transfer functions.	103
3-8	Simulation Flowchart	107
3-9	Recording geometry for the VH simulation study.	109
3-10	Zemax [®] generated recording wavefronts.	110

3-11	Zemax generated probe wavefronts.	111
3-12	Diffraction efficiency versus angular selectivity – hologram S9.	113
3-13	Diffraction efficiency versus angular selectivity – grating F3 #1.	113
3-14	Diffraction efficiency versus angular selectivity – grating F3 #2.	114
3-15	Image plane intensity for grating F3#1	115
3-16	Image plane intensity for grating F3#2	116
3-17	Simulation vs. experiment for S9 angular selectivity.	116
3-18	Simulation vs. experiment for F3#1 angular selectivity.	117
3-19	Simulation vs. experiment for F3#2 angular selectivity.	117
3-20	VHI response to five primary aberrations.	119
3-21	Real versus paraxial objective lens.	120
3-22	Depth selectivity versus objective lens shape factor.	121
3-23	Unslanted grating response versus lens shape factor.	122
3-24	Response to point source displacement along \hat{x} and \hat{z}	123
3-25	Depth selectivity simulation methods, grating F3#1.	125
3-26	Depth selectivity simulation methods, grating F3#2.	125
3-27	Image plane intensity for hologram F3, $\Delta z_p = 0$	127
3-28	Image plane intensity for hologram F3, $\Delta z_p = +50, +105\mu\text{m}$	127
3-29	Aberrated response of F3#1: single #0 cover slip.	129
3-30	Aberrated response of F3#2: single #0 cover slip.	129
3-31	Aberrated response of F3#1: four #0 cover slips.	130
3-32	Aberrated response of F3#2: four #0 cover slips.	130
3-33	Aberrated response of F3: microscope slide.	131
3-34	Microscope slide response for modified simulation result.	132
3-35	Summary of simulation results.	132
3-36	Activity of regions in the hologram aperture.	134
3-37	Defocus response with apodizing masks.	135
3-38	Execution time and simulation error.	136
4-1	Simultaneous VHI and VH projection device.	142

Acknowledgements

The author would like to acknowledge the support of his advisor, Professor George Barbastathis at the Massachusetts Institute of Technology, in providing guidance and valuable input in the execution of this work. The author acknowledges with gratitude the sponsorship of the National Institute of Health for providing the funding for the research described herein. Also invaluable and much appreciated was the support from the MIT Lincoln Laboratory – Lincoln Scholars Program and the Lincoln Scholars Committee, who provided financial backing for the author for the duration of this research, and the support from Lincoln mentor Franz Busse along with Joaquin Otazo, Eric Austin, and Donald Coe in the Group 38 office. Very valuable were the contributions of the research team at the University of Arizona in the Electrical and Computer Engineering department – Professor Raymond Kostuk and colleagues Paul Gelsinger and Yuan Luo who applied their skills to the successful experiments in this work and hosted the author in Tucson to perform these experiments. The author would also like to acknowledge the indispensable support of the 3-D Optical Systems research team at MIT: Jose Dominguez-Caballero for his assistance with the block-FFT processing method, Tony Nichol, Nader Shaar, and Hyun Jin In for their assistance in fabricating resolution targets, and the Nano-Structures Laboratory at MIT for providing facilities that made the fabrication work possible. The author would also like to thank his fiancée Amy and his family and friends for their incredible level of support during the progress of this research.

Chapter 1

Introduction

The purpose of this work is the imaging epithelial tissue containing a marker fluorophore with a minimum resolution of $15\mu\text{m}$ in each dimension, and a field of view of at least 1mm square laterally by 0.5mm in depth and a 100nm spectral bandwidth at 700nm and spectral resolution of 10nm . These goals were to be met by imaging a tissue sample with a new type of microscope incorporating a diffractive element, a volume hologram (VH) in place of the pinhole used in conventional confocal microscopy. As such, most of the work in this thesis is performed with respect to these parameters, and involves large numerical apertures and short objective focal lengths, as the specific application is microscopy of highly scattering biological tissue. The eventual goal is to image such tissue with sharp contrast between volume elements (voxels) for three-dimensional reconstruction at near video rate (10Hz) enabling real-time analysis of tissue structure and composition by a physician.

1.1 The volume hologram and imaging

A hologram is a recording of the interference pattern generated by the interference of coherent waves, allowing both the amplitude and phase of the original object wave to be recorded as first developed by Gabor in 1948 [1]. While holograms can be produced by numerous methods, the holograms relevant to this work are permanent recordings of the interference between electromagnetic waves whose frequency is in the visible spectrum, forming an optical hologram. Such a hologram can be recorded in any medium that is sensitive to visible radiation, and typ-

ically, holograms are recorded with photographic film or a slight variation of such. A hologram recorded in silver halide photographic emulsion on polymer film or photographic plate is an amplitude hologram as the bright portions of the interference fringes will darken the emulsion. It is also a thin hologram*, as the photographic emulsion is typically on the order of 6-7 μ m in thickness, depending on the specific film involved [35]. A hologram that is considered "thin" diffracts in the Raman-Nath regime, meaning it has thickness on the order of the wavelength used in probing the hologram, and certainly does not have sufficient thickness to support changes in the interference fringes along its depth. Volume holograms are recorded in media that have substantial thickness with respect to the recording wavelength and diffract in the Bragg regime. Bragg diffraction occurs when there is significant thickness in the grating to cause mutual interference in the diffracted beam such that certain features seen in thin gratings, such as higher diffraction orders, are not propagated.

1.1.1 Recording volume holograms

The mutual interference of two or more beams of spatially coherent electromagnetic radiation in the visible spectrum is the means of recording optical holograms in this document. The vector representation of two-beam interference occurs as:

$$I = |A_{ref} + A_{sig}|^2 = |A_{ref}|^2 + |A_{sig}|^2 + 2|A_{ref} \cdot A_{sig}| \quad (1.1)$$

$$A = ae^{i\tilde{\mathbf{k}} \cdot \tilde{\mathbf{r}}}$$

Where $\tilde{\mathbf{k}}$ is the wave vector of a particular beam, whose direction is parallel to the propagation direction of the radiation and the magnitude is proportional to the frequency of the radiation. In this work, all magnitudes $|\tilde{\mathbf{k}}|$ for recording usually representative of visible wavelengths at 488nm. The two interfering beams in equation 1.1 are referred to as the reference and signal beam. Typically, in holography the signal beam is the beam from an object that contains information, and the reference is a tightly-controlled, usually planar wavefront beam that provides a base band of spatial frequencies to encode the object wavefront in the photosensitive holographic medium. In this work, this convention is also followed, although the purpose of imaging with

*Depending on the probe wavelength, these may be either "thick" or "thin", more on this later.

holographic filters is to reconstruct the *reference* beam. When holographic filters are used as imaging elements, the object beam is not produced by diffraction from a physical object; rather the two beams are optimized such that when the hologram (after exposure and processing) is probed by an arbitrary wavefront, the diffracted field carries an information-optimized projection of the illumination onto the reference. The VHs described in this work are invariably phase holograms recorded in phenanthrenquinone-doped poly(methyl-methacrylate) (pq-PMMA), although thick holograms may be recorded in other materials exhibiting the photorefractive effect, such as lithium niobate (LiNbO_3) [2][35][5], Ce:KNSBN [8], $\text{Ba}[\text{Fe}(\text{CN}_5)\text{NO}] \cdot 3\text{H}_2\text{O}$ [10], $\text{Sr}_{0.61}\text{Ba}_{0.39}\text{Nb}_2\text{O}_6:\text{Ce}$ [11], and others. Although thick transmission holograms can also be amplitude gratings, the maximum theoretical diffraction efficiency from these materials is 3.7%, versus 100% for phase gratings [35], as periodic absorption is the means for generating diffraction in an amplitude grating. The physical mechanism for the change in refractive index is a two-stage process whereby a photochemical reaction with the doping agent in the media causes polymerization in the bright fringes, thereby creating a diffusion gradient in the material that draws additional monomers into the illuminated regions [12]. The dot product in equation 1.1 describes the local vector of the periodic interference pattern $\tilde{\mathbf{K}}$, which is also the vector describing the index of refraction modulation Δn recorded in the photosensitive polymer. To be precise, Δn as a function of this dot product is not direct but uniformly phase-shifted by $\frac{\pi}{2}$ and usually nonlinear with intensity [35], but the assumption here is that the relationship is a direct one. Therefore, $\tilde{\mathbf{K}}$ can be expressed as:

$$\tilde{\mathbf{K}} = \tilde{\mathbf{k}}_{ref} + \tilde{\mathbf{k}}_{sig} \quad (1.2)$$

$$|\tilde{\mathbf{K}}| = 2\pi \frac{\sin(\theta_{ref}) - \sin(\theta_{sig})}{\lambda}, \quad (1.3)$$

where λ is the recording wavelength and θ is the local angle of the reference or signal beam with respect to the optical axis, defined as the z -axis. Figure 1-1 shows the relationship between recording beams and the resulting grating for some representative recording conditions. In the case of parallel imaging, multiple incoherent reference beams are recorded in the VH media. This requires multiplexing, which means recording multiple two-beam interference patterns in the photosensitive medium as serial, mutually incoherent exposures. For example, an unslanted

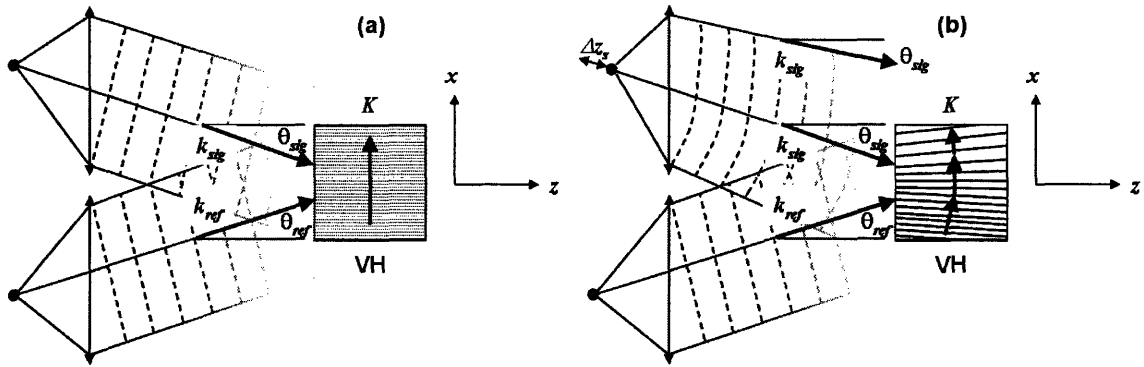


Figure 1-1: Recording geometry for (a) two plane waves, (b) planar reference and defocused point source in the signal arm. The recording geometry in (a) produces an unslanted grating with a constant grating vector \vec{K} over the whole hologram volume. The configuration (b) causes interference between a planar and spherical wave, producing local variations in \vec{k}_{sig} and therefore \vec{K} . The dark lines in the VH are representative of the relative spacing and orientation of the interference fringes recorded in the material.

grating may be recorded as in Fig. 1-1(a), then the signal point source may be moved as in Fig. 1-1(b) but with a new θ_{ref} , and another grating exposed before the material is developed. This process can be repeated many times for different recording configurations, until the material becomes saturated and insensitive to further exposure. A further penalty to increasing the number of gratings is the decrease in the diffraction efficiency of subsequent gratings [6][7][9]. The multiplexing of holograms is critical to the speed of imaging required for the application of real-time medical imaging. Of course, the recording process need not take place in a two-dimensional (2-D) plane as pictured, but exists in three-dimensional (3-D) space, so the choice of point source positions is expanded. In this work however, the geometries are arbitrarily restricted to the $x - z$ plane. At least in the case of the planar-wavefront grating, there is no grating structure along \hat{y} (pointing out of the page), therefore the grating has not recorded any information regarding the y -coordinate of either point source.

1.1.2 Imaging with volume holograms

The concept of utilizing a thick phase grating in transmission as a replacement for a confocal pupil in imaging was first proposed by Barbastathis et. al. [2]. When utilized as optical elements

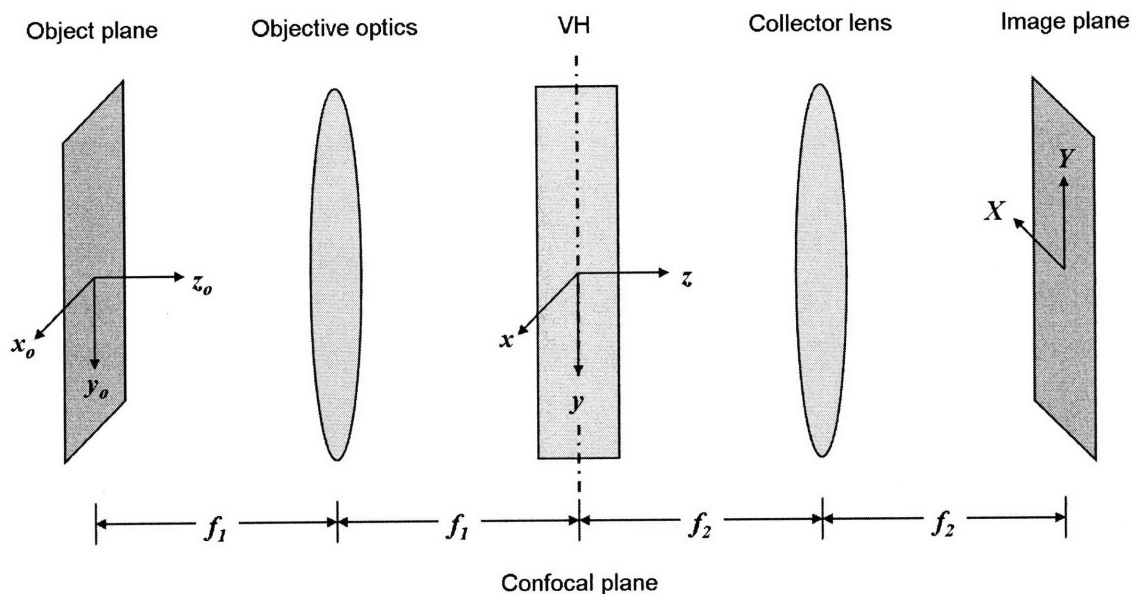


Figure 1-2: Configuration of the basic imaging elements in a VHI system.

in an imaging system, multiplex VHs heterodyne the optical field in three spatial dimensions as well as wavelength, allowing the physical positions and spectral contents of mutually incoherent point sources in an object field to be determined with high accuracy. In other words, a VH placed in the pupil of an imaging system acts as a highly position and wavelength dependent aperture. The general configuration of a volume holographic imaging (VHI) system used in this work is shown in figure 1-2. A point source located at a spatial-spectral position that allows for the maximum possible reconstruction of a reference beam is located at a Bragg-matched position, from the Bragg diffraction that characterizes the thick hologram. Assume an unslanted planar grating as in Fig. 1-1(a). As the hologram was recorded with a spatial carrier with components along \hat{x} , this is known as the Bragg-selective axis of the hologram as displacements of a probe source from the recording position along this axis will cause the reconstruction to be highly attenuated. Conversely, as the grating contains no information along \hat{y} , this is known as the Bragg-degenerate direction, as the grating does not produce any heterodyne behavior in this direction. This is not precisely correct, as the degeneracy will be shown later to be a more complicated effect. However, this assumption is reasonable as the

radius of the degeneracy is typically very large and is normal to the recording plane at the point of intersection. Degeneracy also affects the reconstruction of point sources that are located away from the object plane in the longitudinal direction. In a traditional imaging system, the depth of a point source is indeterminate; defocus produces a diffuse disk on the image plane instead of a sharp point, and all of the energy received by the optical system is conserved in this spot, defocused or not. Conversely, the VHI system only reconstructs the portion of the wavefront generated by a point source that is Bragg-matched to the hologram, attenuating the energy received at the image plane to a degree that is proportional to the amount of defocus or the degree of mismatch. This attenuation occurs for any change in the wavefront phase reaching the VH from the object volume that would affect the Bragg-matched condition in any part of the hologram aperture, including some lateral displacements and wavefront aberrations. Recording multiple gratings, each recorded with a controlled level of defocus in the signal arm and a change in reference beam angle, allows the depth position of a point source to be determined from the resulting intensity map on the image plane. As such, each volume region or voxel imaged by the VHI system has the shape of a column with the long axis aligned with the Bragg degenerate direction. Each multiplexed exposure in the hologram will have its own column assuming sufficient angular separation exists between the reference beams [3]. As such, the multiplexed VHI system is analogous to a parallel confocal microscope, with a pinhole replaced by a variable slit whose width depends upon the spectral bandwidth of the object scene [2][5].

1.1.3 Projection of 3-D spectral data

The object plane of the multiplexed VHI system is ill-defined as the spatial region being imaged is now a volume. The consequence of this arrangement is that the 3-D position plus the spectral coordinate of each point source in the object volume must be represented as a 2-D intensity map on the surface of a detector array in the image plane, as in figure 1-3. Because of the nature of projecting four-dimensional information on a two-dimensional surface, some ambiguity in categorization is present. Like any diffraction grating, the volume hologram acts to decompose the constituent wavelengths of a broadband source over some spatial extent in the image plane. This will occur for each set of columns recorded as multiplexed gratings. Assume that the image plane contains a broadband detector composed of many pixels and suppose that a source object

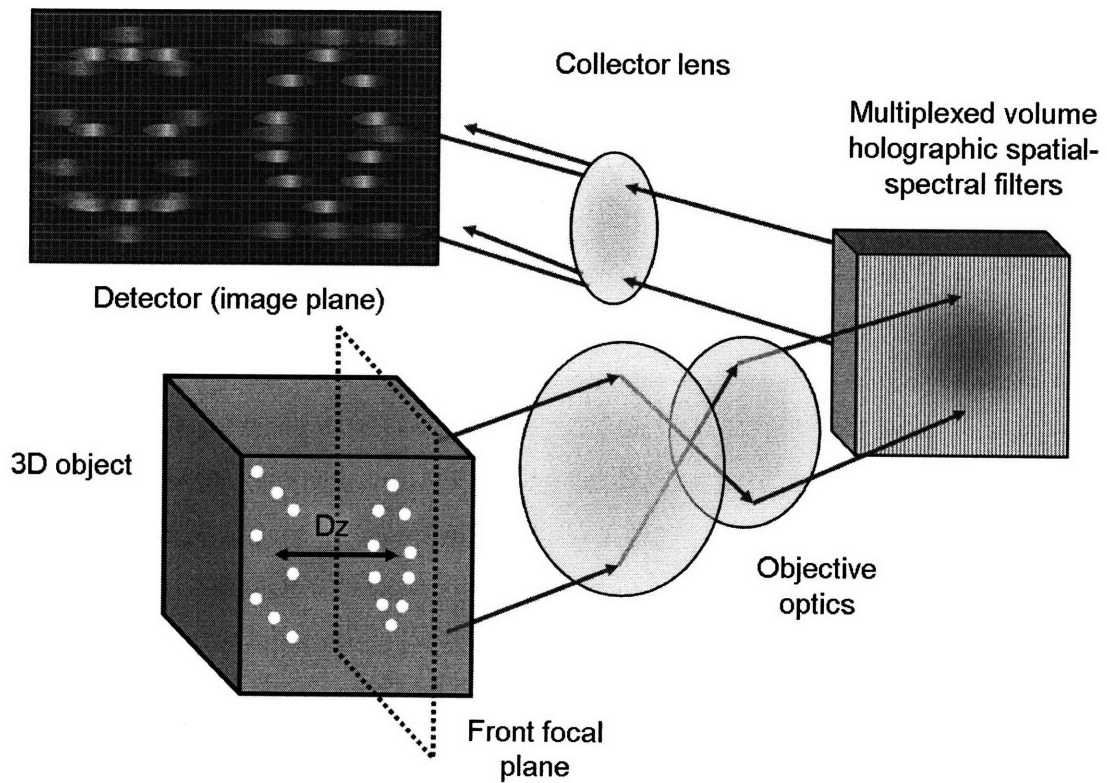


Figure 1-3: Imaging scheme for VHI. The broadband point sources in the 3-D object are reconstructed in the image plane. The spectral content of each point source is spread across the plane, and the point sources are reconstructed at different lateral positions on the image plane corresponding to their depth in the object volume. Unavoidable grating cross-talk causes "ghosting", where a fainter out of focus image of the point source is reconstructed at an image plane position corresponding to an incorrect physical location.

is composed of several closely-spaced point sources emitting over a broad range of wavelengths. Now the problem becomes obvious; determining which region of illumination on the detector corresponds to the physical location of a particular source, or the spectral content of another. On the outset, one could assume that the hologram is recorded in such a way that the various regions illuminated on the image plane are separated to such a degree that there is no spatial-spectral “crosstalk” thereby causing ambiguity in the image processing step, and that the hologram is very thick, allowing the columns to be extremely thin, such that each column can contain only a single column of emitters. While this would certainly solve the described problem, it would make for a rather impractical imaging system as the number of multiplexed Bragg gratings would necessarily be very high relative to the imaged volume. Additionally, a large fraction of the image plane would not be used for sensing such that the imaged columns could be properly spaced. Because the inclusion of such spaces may be impractical, some amount of spatial-spectral ambiguity is likely to be present in the system. Computational inverse algorithms can be applied to further improve imaging accuracy and resolution as well as to provide a means for decomposing the superposition of intensities corresponding to spatially and spectrally separated sources. For example, in the case of biomedical imaging, the spectral content of scattered light from a source might be assumed to be the source bandwidth multiplied by the absorptivity of water over the same range. The construction of such an inverse algorithm is outside of the scope of this work, however. The utility of the VH as an imaging element has been demonstrated with a confocal microscope using a single-grating VH for spatial filtering instead of a pinhole [2], a real-time 3-D hyperspectral microscope [3], a high-resolution profilometer for use at long working distances [4], and others [5]. VHS have also been demonstrated in a non-imaging slitless spectrometer [36][37]. A parallel 2-D hyperspectral imaging system has been proposed that is not VHI, but has some similar aspects [13]. This system makes use of a thin hologram with multiplexed exposures and multiple diffraction orders to reduce the degeneracy between the spatial and spectral coordinates in image space. As this system makes use of a hologram that produces multiple diffracted orders, and so does not produce Bragg diffraction, i.e. a single diffraction order, this system does not have a strong depth-selective quality.

1.2 A short survey of 3-D optical microscopy systems

The term 3-D optical microscope is a shorthand definition used here to describe any device designed to optically image the scattering potential of a 3-D volume at the micro-scale. Attention is paid to this class of imaging as it is most relevant for comparison with the multiplexed VHI method in medical imaging applications. A 3-D microscope is differentiated from a profilometer which could be classified as $2\frac{1}{2}$ -D, as only the reflected light from a single surface is collected. A number of methods are available both commercially and otherwise for this type of imaging, and the important ones are described here.

1.2.1 Confocal microscopy

The confocal microscope was first described in a U.S. Patent filed by Marvin Minsky in 1957 [28], then expanded upon by others, notably Sheppard [14][16][17][27]. The concept of the confocal microscope is quite simple. The object under study is illuminated by a point source behind a condenser lens. The point source may be created by passing the light from an incoherent source such as a tungsten lamp or a coherent laser beam through a pinhole. This arrangement creates an image of the point illumination inside the object. Another pinhole, usually $< 5\mu\text{m}$ in diameter [17], is placed at the confocal position of a standard four focus (4-f) imaging system, such that any light passing through the objective lens that is out of focus will produce a diffuse spot overfilling the pinhole. This is the mechanism by which a confocal microscope achieves depth selectivity, as out of focus light becomes heavily attenuated in the image plane [27]. This property makes the confocal microscope very attractive as a solution for imaging $2\frac{1}{2}$ -D or 3-D objects. The intensity of the response at the detector on the optical axis

$$I(u) = \left(\frac{\sin(u)}{u} \right)^4 \quad (1.4)$$

is described by Sheppard as the variation in detector response I for a displacement along the normalized optical axis u where

$$u = \frac{2z(NA)^2}{\lambda}, \quad (1.5)$$

z is the displacement along the optical axis, NA is the numerical aperture of the objective optics, and λ is the wavelength. The integrated intensity at the image plane versus u is given by

$$I_{int}(u) = \int_0^\infty \left| \int_0^1 J_0(v\rho) \times \exp\left[-\frac{1}{2}iu\rho^2\right] \rho d\rho \right|^4 dv \quad (1.6)$$

where v is the radial coordinate normal to the optical axis and ρ is the normalized pupil coordinate, resulting in a full-width at half maximum (FWHM) value of the depth of field of 1.4λ for a numerical aperture (NA) of unity [16]. Sheppard also notes that a conventional microscope has the response function

$$I_{int}(u) = 1 \quad (1.7)$$

showing that the energy in defocused light is conserved and acts to reduce contrast. As originally described in the patent [28], this microscope builds an image from successive scans of the object in three dimensions, hence it is known as a scanning confocal microscope. In this case the instantaneous field of view of the microscope is equal to the size of the imaging element. Sheppard makes note of a "direct-view" confocal microscope in [14], and instrument based on the principle of the confocal microscope yet featuring a field of view comparable to a traditional microscope. This is accomplished by rotating a pair of matched perforated disks, also known as a "Nipkow disk" [15], inside the instrument at high speed, using the motion blur of the individual imaging elements to simulate a parallel reconstruction. Of course, in the case of incoherent illumination by a tungsten lamp, the system is strongly limited by the amount of illumination that can be projected into the sample because of the need for very small pinholes. However, according to [14], this illumination scheme is sufficient in the case of the direct-view microscope as multiple pinholes are utilized in the Nipkow disk. Recently, a method for correcting the pinhole alignment error in the direct imaging of thick phase objects, such as biological tissues, has been introduced in [15]. The alignment problem is a direct result of the variable focus error introduced by the anisotropic refractive index of such materials, and the solution in [15] is to use computer-controlled electronic pinholes behind the objective coupled to a feedback loop consisting of a camera and a simple min-max image processing algorithm. This method demonstrates clear imaging of thick biological specimens with the confocal method in such a way as to be similar to VHI. Of course, this method requires the specimen to be physically

mounted inside the two halves of the mechanism, and is therefore inferior to VHI in terms of in vivo imaging, as VHI is capable of operating in any conventional microscope design, including endoscopes.

1.2.2 Two-photon microscopy

An advance in 3-D imaging based on the confocal microscope is two-photon microscopy, which does not require a matched pinhole set in the illumination and imaging system. Rather, this method relies on illumination at very high flux levels and infrared wavelengths to produce two-photon excitation of a fluorescent object and subsequent fluorescence in the visible spectrum. Two-photon excitation is the means by which a fluorophore may be excited into an unstable high-energy state by means of two long wavelength photons being absorbed by a fluorophore in the same quantized event. The illuminating beam is focused into the object by the objective lens, and the flux level is such that the two-photon excitation only occurs in the region of the focal point of the objective, which is the mechanism that renders the pinhole pair unnecessary. This in turn means that a larger amount of emitted light passes through the imaging optics. The disadvantages of this method are a typically lower resolution than standard confocal microscopy due to the longer wavelengths involved, the high flux levels required, and localized bleaching or photo-damage to the object being imaged. The required high flux levels may be realized with pulsed lasers that have a low average power, improving the practicality of the two-photon method [18][19].

1.2.3 Optical coherence tomography (OCT)

The concept of optical coherence tomography is relatively new, having been first described in 1991 [29]. OCT is a scanning method as confocal microscopy, however the method of depth discrimination is based on the properties of coherent light rather than confocal optics and vignetting. OCT is best used when imaging optically thick objects that have scattering or reflective internal features, as many types of biological tissue. Time-domain (TD) OCT is the earliest method developed and generally the easiest to implement. A Michelson-type interferometer is constructed with a mirror on a translation stage placed in the reference arm, and the object to be imaged behind an objective lens in the signal arm. A low-coherence light source,

such as a super-luminescent light emitting diode (LED) or a pulsed laser, is placed in the interferometer to illuminate both arms while a single-element detector is located at the output. As the mirror in the reference arm is scanned along the optical path, a certain position may be reached where the light reflected from the object interferes with the reference, signifying that light from the focal spot in the signal arm has the same optical path length as the reference, providing depth information [21]. The depth resolution of an OCT system is directly related to the coherence length of the source, as shorter coherence length provides less ambiguity in the correlation position and greater resolution. Given a center wavelength λ_o and a spectral bandwidth FWHM of $\Delta\lambda$, the free-space correlation length is given by [20]

$$l_c \approx 0.44 \frac{\lambda_o^2}{\Delta\lambda} \quad (1.8)$$

for a Gaussian source. As with confocal microscopy, the lateral resolution of OCT is typically a function of the spot size of the objective only; lateral resolution can develop a relationship to the depth resolution with very large spectral bandwidths [20]. Therefore, OCT is theoretically capable of very high lateral and axial resolutions. A large NA objective provides a high lateral resolution and a reduction in coherent speckle noise, however this increases the effect of optical aberrations, reducing the sensitivity of the method and increasing the correlation length. The main limitation of TD-OCT is a heavy reliance on mechanical scanning methods to reconstruct an object volume of scatterers. This increases acquisition time, measurement errors, required power, and system size. Acquisition time for a 2-D slice (axial and one lateral dimension) with mechanical scanning is related to the scanning parameters by [21]

$$T_{acq.} = \epsilon \frac{\text{scan depth}}{\text{scan velocity}} (\# \text{ transverse pixels}), \quad (1.9)$$

where ϵ is an efficiency parameter specific to a particular scanning mechanism, ~ 1.125 in [21]. Clearly, a means of eliminating the scanning requirement of this method is important. One popular method of expanding upon TD-OCT to reduce scanning is Fourier-domain (FD) OCT. This method involves substituting a spectrometer containing a linear array of detectors for the single-element detector of TD-OCT. The spectrometer records the "correlogram", or the correlation spectrum of the object at a particular point. The Fourier transform of the

correlogram provides the depth-dependent response profile of the object, allowing the reference mirror to remain fixed [20]. Of course, FD-OCT still requires lateral scanning of the objective optics to create a depth profile. As the cost and performance of available low-coherence sources improves, OCT will likely become even more attractive in the future.

1.2.4 Summary

A quantitative comparison of the major 3-D optical microscopy systems to VHI is given in table 1-1.

	Confocal [27]	OCT [29]	VHI
Lateral Resolution	$0.72\mu\text{m}^\dagger$	$9\mu\text{m}^\ddagger$	$<7.5\mu\text{m}^\S$
Axial Resolution (FWHM)	$5\mu\text{m}^\P$	$17\mu\text{m}^\ddagger$	$32\mu\text{m}^\parallel$
Field of View	Time-Limited	Time-Limited	$340\times 1280\mu\text{m}^\S$
Time / Image $340\times 1280\mu\text{m}$ Plane	Similar to OCT	34s Achieved**, 0.04s Possible	$0.45\text{s}^{\dagger\dagger}$
Lateral Scanning	Yes	Yes	No
Axial Scanning	Yes	Yes - TD; No - FD	No

Table 1-1: Comparison of various passive 3-D imaging microscopy methods.

From this table, it is clear that VHI has the potential to be competitive with confocal microscopy and OCT, especially in the time domain, as multiplex VHI can capture and process light from an object volume in parallel and theoretically requires no scanning. Theoretical lateral resolution of VHI is equal to confocal; the experimental result noted here is discussed further in section 2.6.1. Additionally, the depth selectivity of VHI is a function of lateral source position in object space; in most cases the axial resolution is roughly equal to OCT.

[†]Diffraction-limited spot size, NA 0.54, $\lambda = 0.633\mu\text{m}$ $\left[\frac{0.61\lambda}{NA}\right]$

[‡]In air, $\lambda_{center} = 0.830\mu\text{m}$

[§]NA 0.55, $\lambda_{center} = 0.599\mu\text{m}$, bandwidth FWHM $<40\text{nm}$

[¶]NA 0.54, $\lambda = 0.633\mu\text{m}$

^{||}In air, NA 0.55, $\lambda = 0.633\mu\text{m}$, Grating (F3B#1)

**Estimated value, $\sim 1\times 2.4\text{mm}$ plane scanned in reference at 2mm depth

^{††}All available depth planes

1.3 A summary of this research

In this work there are two distinct goals. First, to create and execute a series of experiments or methods for determining the imaging performance of the VHI system. These tests should be somewhat general, as the specific metrics of image quality that may be applicable to VHI systems are not well defined, and also because a more general imaging test allows the VHI system to be compared with other imaging modalities. Second, the objective of this work is to develop a means for accurately simulating the imaging performance of VHI systems as it relates to the experiments themselves. These means should be flexible enough such that they can be adapted to more specific image quality or performance metrics as they are developed. As such, the simulation must embody the necessary structure to enable design flexibility so that it would not be constrained to idealized system parameters. The simulation tools should have sufficient accuracy to produce meaningful results for these metrics. Speed is also an issue, such that a simulation might be applied to an optimization routine that allows the designer of a VHI system to push the boundaries of its capabilities for any given figure of merit. Because the eventual goal of this research is to create an imaging system for the purpose of medical imaging, a very demanding application, the simulation must be able to function effectively in this regard as optimizations will be quite necessary. In terms of functions effectively characterizing system performance, it is hoped that this work will contribute to a better qualitative and quantitative understanding of the nature of VH imagery such that relevant merit functions might be realized.

1.3.1 Experimental efforts

In terms of experiment, there were two different tests that were chosen, as both affect the performance of VHI. As the special property of VHI is spatial and spectral heterodyne behavior, also intermittently referred to here with the broad term "selectivity", the experimental efforts were primarily designed to understand the capabilities of the VHI system in terms of point source position versus the accompanying reconstruction generated by the hologram. In terms of defining a sort of space-dependent aperture function, this is the strongest part of the system transfer function that characterizes VHI. However, within the boundaries of a space-dependent aperture, VHI systems are subject to the same constraints of a conventional imaging system.

The ability of VHI to reconstruct a point source in this region can be evaluated in terms of image quality just as a conventional imaging system would be, and here the usual terms like field of view, spot size, MTF, etc. become the relevant terms. The experiments performed, although somewhat basic in nature, fulfil the need to understand both the VHI-specific and non-specific parameters of image quality. Because VHs may be constructed in a variety of recording schemes, and may involve multiplexing of different gratings to a large number, an extremely large taxonomy of possible forms exist; each one is potentially useful to some variation of a specific imaging task. This is somewhat different from conventional imagers, where typically the size and location of an aperture holds a similar meaning, and apertures are usually round and clear, save an apodizing filter or phase contrasting techniques. This fact was considered, and while it is not possible to test all recording and probe geometries and parameters for all conceivable VH configurations, a representative set was chosen, as shown in table 1-2.

Name	F1	S9	F3A	F3B	F17
Gratings^{††}	1	1	2	2	5
Exposure Wavelength	488nm	488nm	488nm	488nm	488nm
Thickness	1.65mm	1.61mm	1.54mm	1.54mm	2.17mm
Nominal Recording Angle	$\pm 32^\circ$	$\pm 34^\circ$	$\pm 34^\circ$	$\pm 34^\circ$	$\pm 34^\circ$
Δz Per Grating	-	-	$50\mu\text{m}$	$50\mu\text{m}$	$50\mu\text{m}$
$\Delta\theta$ Per Grating	-	-	2.230°	2.543°	$\sim 2.5^\circ$

Table 1-2: Holographic filters used for evaluation in this document.

All of these holograms consist of phase gratings written in pq-PMMA photopolymer. This set includes two single grating holograms, F1 and S9; along with three multiplex grating holograms: F3A and F3B with two gratings each, and F17 with five. This set is a useful one for generally understanding VHI performance, as the single grating holograms are somewhat idealized versions of the individual gratings in a multiplex hologram. The five-grating hologram is examined here in a more qualitative fashion than the other gratings, although in section 2.6 it

^{††}The author would like to acknowledge the efforts of Yuan Luo and Paul Gelsinger at the University of Arizona for the fabrication of these holograms.

will be used extensively to image various volumetric objects. The experiments used to evaluate these gratings were as follows:

- Angular selectivity
- Depth selectivity or depth point-spread function (z-PSF)
- Lateral point-spread function (PSF)
- Lateral resolution

The first two items were performed with VHI-specific goals in mind, as they demonstrate the ability of the VHI system to reject sources outside a small volume of space or voxel in the object plane. The last two experiments would be consistent with any other conventional image system, that is, determining the limit on the smallest lateral feature spacing that allows the VHI system to unambiguously separate features. Also in a related test, to measure the image of a point source to determine the impulse response of the system when imaging a point source inside a Bragg-matched voxel. The angular selectivity experiment was performed with the hologram placed on a rotation stage and probed with a planar wavefront laser beam. Then, the diffracted intensity was monitored as a function of angle between the hologram and the incident beam. This test provides insight into the field of view of each grating in the hologram, as in this test the characteristics of the hologram as a field stop are measured. This test will be discussed in section 2.3. The depth selectivity experiment involves the use of a point source generated by a microscope objective attached to a lateral translation stage. The diffracted intensity was monitored as a function of position along the optical axis. This test will be discussed in section 2.4. In each case, the tests will demonstrate that the VHI system exhibits strong angular and depth selectivity, suitable for spatial heterodyning. The depth selectivity experiments are carried further in section 2.5, where the beam entering the objective optics is deliberately aberrated to investigate the sensitivity of the depth selectivity to distorted or mismatched wavefronts. For each of these tests, the alignment of the hologram is crucial to success, as the hologram functions in a similar manner as a pinhole in a confocal microscope; the results of the experiment are tightly coupled to the orientation and position of the hologram with respect to the incident beam. This problem was solved by placing the hologram on a tip-tilt mount and

Careful alignment. The lateral point-spread function as described in 2.2 was measured with an interferometric technique, and shows that the hologram is capable of generating a diffraction-limited reconstruction of a point source within the Bragg-matched voxel. Also discussed are some interesting features of the measured PSF that are peculiar to the VHI method and are matched with theoretical predictions. The lateral resolution of the VHI system will be given a cursory examination in section 2.6.1. This measurement was performed by imaging a narrow-band fluorescent resolution target simultaneously with both gratings of hologram F3B. A lower bound for lateral resolution is determined by examination of the focal plane images of the target. The resolution target used in this experiment is fluorescent, nearly transparent, and volumetric with regular detail. The design and manufacture of this novel target is described in section 2.1 in more detail. As the first two experiments were the most relevant and useful for this work, they are more thoroughly studied.

1.3.2 Simulation efforts

In keeping with the overall necessities of the design project, the simulation effort has been developed along the lines of flexibility. This work endeavors to produce a simulation that can capture all aspects of a VHI system, from the lenses comprising the objective to the hologram itself. The simulation architecture that is described here is based around the weak diffraction approximation, or 1st-order Born approximation. This follows from Huygens principle describing an appropriate Green's function, and the Fourier relationship between the pupil plane centered inside the hologram and the image plane. The relevant formulae are discussed in section 3.1.2, where for the first time, the curvature in the Bragg slit is described. The weak diffraction technique allows flexibility as the thick hologram is assumed to be simply a linear system of independent thin holograms. Since the Fourier relationship is emphasized, the hologram can be an amplitude or phase grating with any arbitrary function describing the change in the material. This method is also useful as it utilizes a non-paraxial diffraction kernel.

1.3.3 Matlab[®] and Zemax[®]

This simulation was written in Matlab[®], and interfaces directly with the optical design code Zemax[®] to generate and probe virtual holograms based on the representation of recording

and imaging optics in the Zemax[®] lens file. Of course, the holograms in table 1-2 are quite large in volume, and to mitigate any limitations arising from memory or processing time, the simulation has been fully parallelized with a special parallel version of Matlab[®] such that it has been run on a grid computer. The details of this method and the other aspects of the simulation architecture are described more fully in chapter 3. This simulation is used to study:

- Angular selectivity
- Depth selectivity
- Lateral PSF

As these are the aspects of imaging that are most heavily dependent upon the VH. In addition, the effect of objective lens aberration on the depth selectivity of VHI is investigated in detail in section 3.3.2, both to verify the experimental results and better understand the effect of aberration in a very controlled environment. Additionally, the results of a rigorous coupled-wave (RCW) simulation are provided when available for reference. These studies show that the weak diffraction (WD) method does a fair job of simulating the angular selectivity, and surprisingly, the diffraction efficiency as well. However, as shown later, the simulation is over-sensitive to defocus for the NA of the VHI system that is simulated, producing estimates of depth selectivity performance that are somewhat inaccurate, especially with large magnitudes of defocus. In terms of response to aberration the simulation performs better, and the relative change in depth selectivity with aberration is similar to the experimental result. This provides valuable insight into aberration that may be useful if, for example, a hologram were recorded by very well-corrected optics but used in an endoscope with gradient-index (GRIN) optics, and should prove useful in the optimization of such systems in the future.

Chapter 2

Evaluating the Performance of VHI Systems

2.1 Resolution target

In any imaging system, quantitative performance metrics are necessary to provide a measure of image quality, resolving power, or other relevant quantities of interest. The VHI system is no different, and a new approach to designing a resolution target was required to capture all aspects of the imaging modality. The VHI system is capable of simultaneous imaging in three dimensions of a weakly scattering transparent object with broadband fluorescent features, and the resolution target designed for the VHI system includes these attributes. The resolution target was designed to be able to test the resolving power of the VHI system at each lateral position in the object plane, as well as the ability of the VHI system to discriminate between fluorescent sources located in different depth planes. The fluorescent emission was desired to be narrow-band, so as to avoid degeneracy in the image plane. The design is also required to be very flexible, as the capabilities of holographic filters are evolving as work continues.

2.1.1 Target design

The resolution target design requirements are as follows:

- Lateral features should be sufficient to determine resolution at any radial position of the

object plane

- Placement of features in space must be conducted with high accuracy
- Fluorescent emission must have a center frequency near the presumed emission from bio-compatible fluorophores and/or backscatter from the illumination source
- Fluorescent emission must be powerful enough to generate a flux on the image plane such that the system is not detector noise-limited
- Target depth features must be unambiguous within the designed sectioning capabilities of the holographic filter
- Design flexibility

A number of potential construction methods were examined for this task. The selected target design is composed of three layers: Base, spacer, and active layer. A series of transparent active layers, containing a fluorescent or scattering pattern, are stacked against each other with spacers between active layers to control inter-layer thickness. This stack is then attached to the substrate layer for easy handling. Each active layer must be easily distinguishable from the next, and the implemented design uses alternating orientations of a non-symmetric pattern to achieve this. Alternatively, different patterns or fluorescent emission center wavelengths may be used in each layer. Within each active layer, photolithography is used to pattern the fluorescent medium in a highly controlled manner, achieving accuracy comparable to the 365nm wavelength of the patterning equipment. The transparent substrate for the fluorescent active layer is a thin glass cover slip. The base layer for the finished target is a glass microscope slide.

Fluorophore selection

A large variety of fluorescent materials were considered for use in the resolution target. Although certain commonly-used dyes, such as Texas Red and R-Phycoerythrin, have center emission wavelengths very close to 600nm and very high quantum efficiencies (51% and 68% respectively), they require careful filtering of excitation sources to minimize their spectral bandwidths [25]. This would prove difficult in a target involving multiple center wavelength emissions between layers. Instead, CdSe-ZnS Core-shell quantum dots (QDs) are used as the fluorescent

material in the active layers of the resolution target design. QDs offer the advantages of a high quantum efficiency, a narrow and symmetrical emission bandwidth, and a very wide absorption bandwidth. Additionally, QDs do not suffer from photochemical degradation and the emission bandwidth is not dependent upon the excitation wavelength. The core-shell architecture improves the quantum yield of the system by encircling the core CdSe semiconductor with a larger bandgap material, thus preventing non-radiative energy losses from the core material [24]. QDs with two different center wavelengths were used in various iterations of the resolution target. The QDs used in these phantoms are manufactured by Evident Technologies, and both varieties are dissolved in toluene.

Type	Adirondack Green	Fort Orange
Part #	ED-C11-TOL-0520	ED-C11-TOL-0600
Lot #	AMB63_50	LN51103A
Absorption wavelength	<502nm	<581nm
Center emission wavelength	521nm	599nm
Bandwidth	<40nm [22]	<40nm [22]
Concentration	1.16mg/mL, 93.84nmol/mL of Toluene	1.47mg/mL, 21.29nmol/mL of Toluene
Quantum Yield	>50% [22]	>50% [22]
Composition	CdSe core, ZnS shell	CdSe core, ZnS shell
Nominal Diameter	7.5nm [22] \pm 5% [24]	8.7nm [22] \pm 5% [24]

Table 2-1: Quantum dots used in the construction of the resolution target.

The recommended excitation wavelength for all Evident Technologies QDs is <400nm. Qualitatively, incoherent illumination at 365nm from a fluorescent UV lamp with only a few watts of power provides enough emission from the target for the layer patterns to be easily visible to the naked eye, even under bright room light. Shorter wavelengths, at 300nm and 254nm, tend to produce a diminished response from the target possibly due to greater absorption by the glass comprising the substrates of the various layers. The absorption and emission spectra are shown in Fig. 2-1.

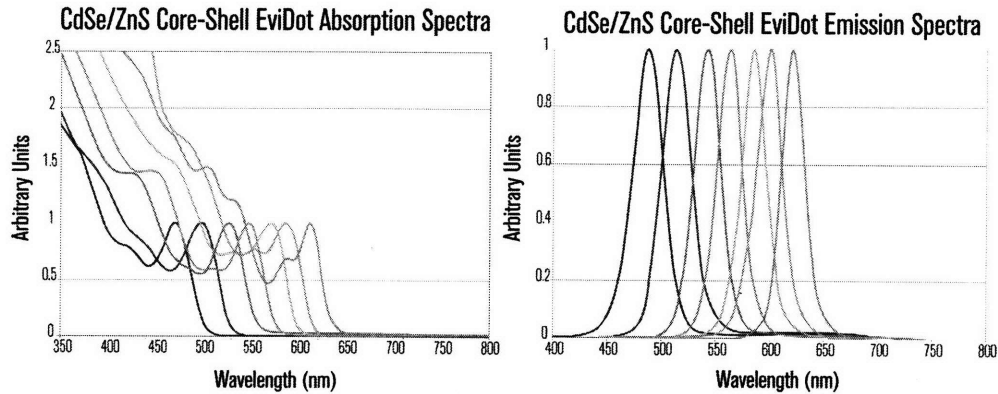


Figure 2-1: Absorption and emission spectra for CdSe-ZnS Core-Shell quantum dots. Fort Orange is the second curve from the right, Adirondack Green is second from the left. www.evidenttech.com

Pattern design

The pattern used in each active layer was loosely adapted from the NBS-1952 Resolution Test Chart (T-40) [26] shown in Fig. 2-2. This target features lines with a regular change in spatial frequency as radial distance increases from the center of the object plane. As with the NBS-1952 pattern, the target as designed contains two orthogonal sets of straight lines with varying spatial frequencies as a function of position; one set has high frequencies toward the center of the target, the other is reversed. This allows the lateral modulation transfer function (MTF) to be evaluated across the image plane. Toward the same goal, a pattern of small circles with high density toward the center and outside of the target is placed between the orthogonal lines. The circles in the pattern may also be useful in determining the nature of any off-axis primary aberrations. For example, coma present in the system will produce a distinct "tail" in a certain direction; astigmatism will cause the circle to be imaged as an ellipse. A dimensional drawing of the pattern is shown in Fig. 2-3. The pattern is created in the active layer by applying, via spinning in a liquid form on a turntable, a photosensitive mask material to the surface of the cover slip. This polymer material is then baked to polymerize, covered with a patterned mask, and exposed to UV light in a photolithography machine. When developed, the mask material exposed to light is removed leaving a bare glass pattern. The unprotected area of the slide is then etched with hydrofluoric (HF) acid to produce trenches in the form of the original mask

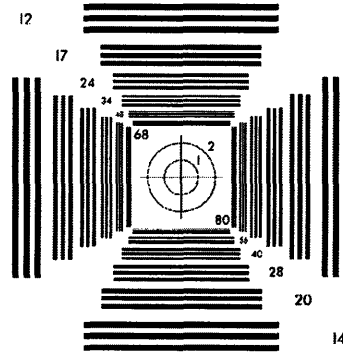


Figure 2-2: NBS-1952 resolution target.

pattern*.

2.1.2 Fabrication methods

At the outset, a number of fabrication methods were considered for the active layers. One of these included etching microfluid channels in the glass surface or alternatively, in the photoresist pattern. While feasible, this required a more complicated manufacturing process involving a more viscous SU-8 photoresist. Another involved mixing QDs in powder form into the SU-8. Yet another method that was attempted was to use the rough etched glass surface as a scattering layer with the QDs "painted" around the edges of the cover slip. This would guide the light emitted by the QDs through the cover slip, where it would be scattered out of plane by the rough glass. This was feasible but not reliable, as the surface left by the HF etch was not consistently rough. In the end, the following configuration was chosen for the resolution target: The base of the target assembly is a Fisher Scientific microscope slide, #12-549, 3in x 1in x 1mm. The active layer substrates are #0 glass cover slips, nominally 100 μ m thick and 25.4mm x 25.4mm square. The pattern etched into the active layer is generated by exposing the patterned masked surface of the substrate cover slip to HF for eight minutes. This process generates trenches in the exposed glass that are <1 μ m deep [39]. The glass layer is cleaned, and a drop of Fort Orange QDs suspended in toluene is placed on the surface of the etched glass

*The author would like to acknowledge the assistance of Tony Nichol, Nader Shaar, and the Nano-Structures Laboratory at MIT in patterning and etching the substrate layers.

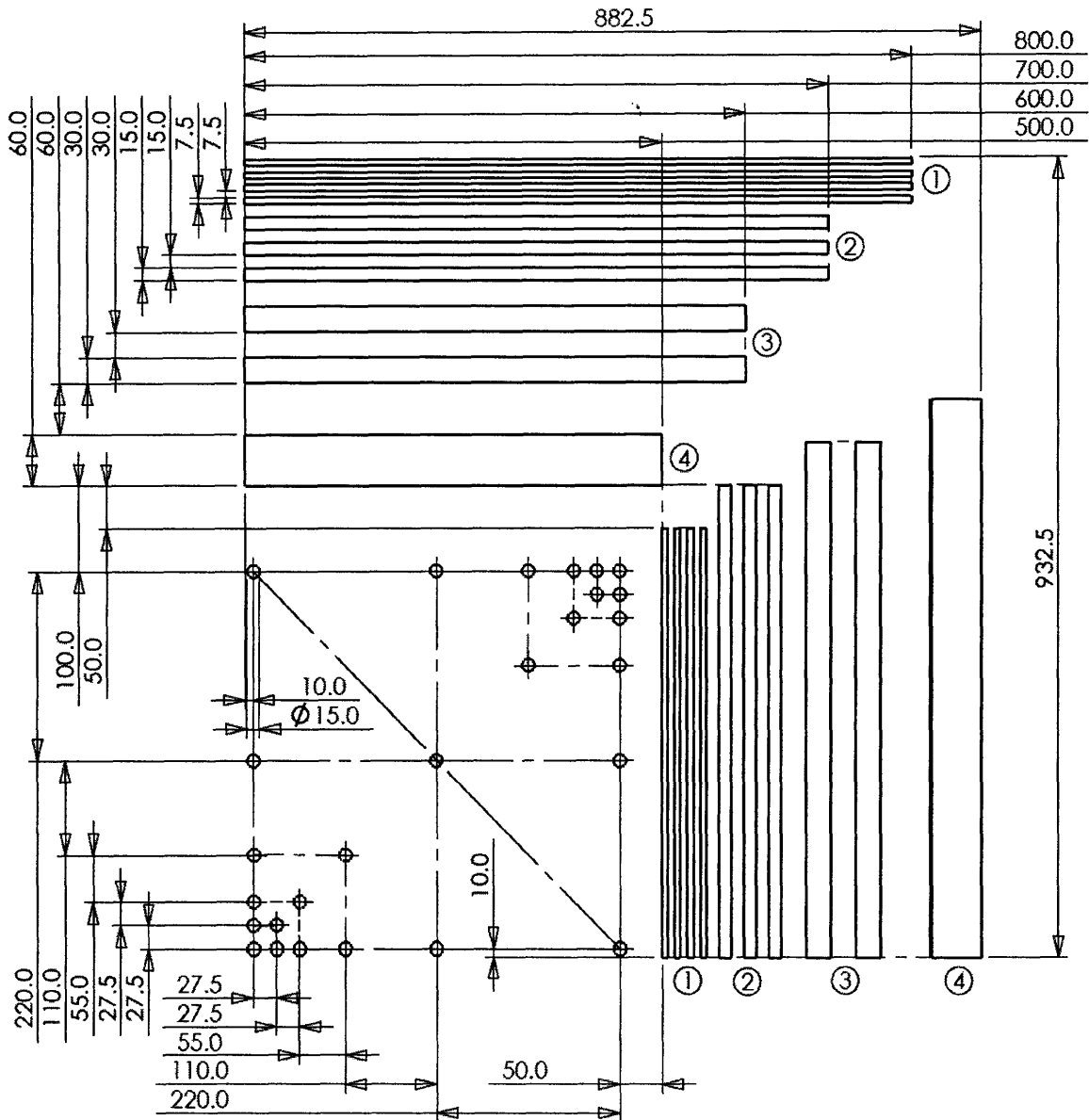


Figure 2-3: Pattern etched into the active layer of the resolution target. This design is meant to evaluate the MTF of the VHI system in the entire object plane while being non-symmetric. Units are in microns.

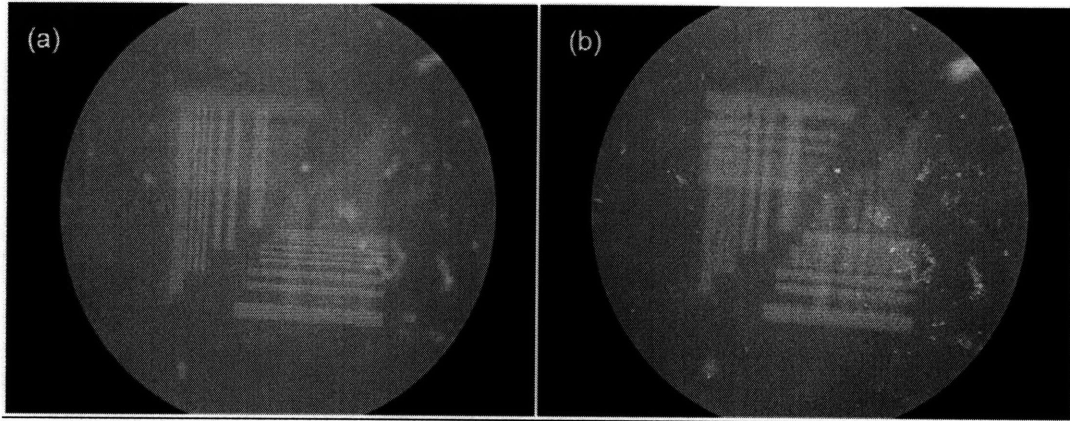


Figure 2-4: Microscope image focusing on (a) a single layer and (b) both target layers. A conventional microscope such as this cannot focus on both layers simultaneously while separating intensity contributions from each layer.

with a pipette. The toluene is allowed to evaporate, and the QDs are wiped across the surface of the slide with the edge of another glass slide, leaving those in the trenches in place. Adirondack Green QDs were also tried in this target design, however the toluene did not evaporate fully, leaving a QD film over much of the patterned area. The active layers are attached to each other and to the base with Dow Corning 3145 RTV adhesive. In the construction of some targets, this adhesive lies between the active layers and the base, and acts as the spacer layer, however the thickness between active layers cannot be carefully controlled with this method. This does provide a benefit of continuous index-matched material throughout the target as the adhesive is clear and colorless with a refractive index of 1.5 [23]. Alternatively, the target may be constructed with one or more layers of adhesive Kapton film forming the spacer between active layers. While this method does greatly increase the control over the thickness between layers, it becomes difficult to apply any index-matched material between the active layers that will achieve contact and not cause the QDs to flow out from the etched pattern. Another method of construction, perhaps with the QDs captured inside a solid layer, would alleviate this problem. A conventional microscope image of the target as constructed is shown in Fig. 2-4. The design objectives for the target as built were somewhat more modest than the initial project design requirements, reflecting the state of the development of holographic filters used

in the VH prototype imaging system. Nevertheless, a significant amount of work was required to meet the design goals.

	Design Goal	Achieved
Lateral Extent	1mm	1.285mm [†]
Minimum Layer Separation	15 μ m	12.5 μ m [‡]
Minimum Lateral Feature Size	15 μ m	7.5 μ m
Feature Depth	<7.5 μ m	<1 μ m
Emission Peak	600-700nm	490-1900nm [§]
Spectral Bandwidth	10nm	40nm

Table 2-2: Quantitative requirements for a pattern to successfully test the VHI microscope.

2.2 Lateral point spread function

One of the most basic of performance figures for an imaging system is the lateral point spread function (PSF). In linear system theory, the complete system response can be described as a linear combination of the response of the constituent elements. In a linear imaging system, the overall incoherent PSF may be obtained as a convolution of the PSF of the constituent lenses and stops that make up the system. In the VHI system discussed previously, the holographic element acts as the element restricting the amount of light (aperture stop) allowed to reach the collector lens, and consequently, the image plane. Also, the hologram filters the angular spectrum of incident light that is allowed to pass, acting as a field stop. Therefore, understanding the nature of the hologram PSF is vital to understanding and predicting the resolution limits of the VHI system in general. While the hologram PSF is strongly non-space-invariant, determining the on-axis PSF is still a very useful tool in predicting image quality at the center of the reference beam reconstruction. A widely-used and very accurate method for measuring the incoherent PSF of an imaging system is the knife-edge test, originally developed by Foucault in 1859. This test involves the imaging of a point source by the system under test while a knife edge

[†]Diagonal dimension; per layer

[‡]Only possible for pairs of adjacent layers

[§]QDs available from Evidentech in this range

is progressively drawn across the image and the intensity of the light passing the knife edge is monitored [30]. In the original test, the exit pupil is observed with the eye to discern any irregularities in the progressive obscuration that qualitatively indicate aberrations, integrating the total received intensity at various positions during this process provides a quantitative measure of the spatial derivative of the point image. This is helpful, however the holographic filter has little if any optical power, requiring a collector lens to be present. This would still give an accurate measurement of the PSF assuming that the response of the lens alone could be measured and removed from the overall response. This method, although fairly standard, depends upon very accurate lateral positioning. Based on a preliminary analytical treatment of the hologram response discussed earlier, it was assumed that the PSF would not be radially symmetric, requiring a much more difficult two-axis tomographic measurement. Instead, the measurement of the PSF was made with an imaging interferometer.

2.2.1 Interference terms for field reconstruction

The coherent sum of amplitudes that causes interference fringes in intensity is given by (2.1). This equation assumes that the polarization vectors of the interfering beams are parallel and involves a time-average of the modulating electric field

$$I = |A_{ref} + A_{obj}|^2 = |A_{ref}|^2 + |A_{obj}|^2 + 2|A_{ref} \cdot A_{obj}|. \quad (2.1)$$

Let $A_{ref}(x, y) = a_{ref}(x, y)e^{i\phi_{ref}(x, y)}$ and $A_{obj}(x, y) = a_{obj}(x, y)e^{i\phi_{obj}(x, y)}$, where $a_{ref}(x, y)$ and $a_{obj}(x, y)$ are positive real-valued functions. For a single beam, it can be seen from 2.1 that $I = |A|^2 = A \cdot A^* = a^2$ and

$$\begin{aligned} I &= I_{ref} + I_{obj} + 2|A_{ref} \cdot A_{obj}| \\ &= I_{ref} + I_{obj} + (A_{ref}^* \cdot A_{obj} + A_{obj}^* \cdot A_{ref}) \\ &= I_{ref} + I_{obj} + a_{ref}a_{obj} \left(e^{i(\phi_{obj} - \phi_{ref})} + e^{-i(\phi_{obj} - \phi_{ref})} \right) \\ &= I_{ref} + I_{obj} + 2a_{ref}a_{obj} \cos(\phi_{obj} - \phi_{ref}) \\ &= I_{ref} + I_{obj} + 2\sqrt{I_{ref}I_{obj}} \cos(\Delta\phi). \end{aligned} \quad (2.2)$$

Therefore

$$\begin{aligned}\frac{I - I_{ref} - I_{obj}}{2\sqrt{I_{ref}I_{obj}}} &= \cos(\Delta\phi) \\ \Delta\phi(x, y) &= \arccos\left(\frac{I - I_{ref} - I_{obj}}{2\sqrt{I_{ref}I_{obj}}}\right).\end{aligned}\quad (2.3)$$

The derivation of equation 2.2 can be found in [31]. If the reference is a plane wave such that $\phi_{ref}(x, y) = const$, then $\phi_{obj}(x, y) = \Delta\phi(x, y) + const$, and the constant phase term can be neglected, leaving $\phi_{obj}(x, y) = \Delta\phi(x, y)$. The object field for positive $a_{obj}(x, y)$ can then be reconstructed as

$$\begin{aligned}A_{obj}(x, y) &= a_{obj}(x, y)e^{i\Delta\phi(x, y)} \\ A_{obj}(x, y) &= \sqrt{I_{obj}(x, y)}e^{i\arccos\left(\frac{I - I_{ref} - I_{obj}}{2\sqrt{I_{ref}I_{obj}}}\right)}.\end{aligned}\quad (2.4)$$

Fourier transforming the object field gives the complex amplitude of the field at the focus of an ideal lens where ξ and η are spatial frequencies along x and y :

$$a_{PSF}(\xi, \eta) = \iint_{-\infty}^{\infty} \sqrt{I_{obj}(x, y)}e^{i\Delta\phi(x, y)}e^{-i2\pi(\xi x + \eta y)} dx dy \quad (2.5)$$

In the case of a discrete sampling of the intensities along x and y , the discrete transform is used instead. Let $\xi = \frac{u}{N\Delta x} = \frac{x'}{\lambda f}$, $u = 0, 1, 2, \dots, N - 1$ and $\eta = \frac{v}{N\Delta x} = \frac{y'}{\lambda f}$, $v = 0, 1, 2, \dots, N - 1$ for a square domain of $N \times N$ square pixels; λ is the wavelength of the light used to generate the interferograms and f is the focal length of the perfect lens. For a realistic representation of the system performance, this should match the focal length of the collector or eyepiece lens. The discrete form is shown in equation 2.6 where n and m are pixel indices in the original interferograms from $0, 1, 2, \dots, N - 1$.

$$\begin{aligned}a_{PSF}(u, v) &= \sum_{n=0}^{N-1} \sum_{m=0}^{N-1} \sqrt{I_{obj}(n, m)}e^{i\Delta\phi(n, m)}e^{-i2\pi\frac{(un+vm)}{N}} \\ a_{PSF}(x', y') &= \sum_{n=0}^{N-1} \sum_{m=0}^{N-1} \sqrt{I_{obj}(n, m)}e^{i\Delta\phi(n, m)}e^{-i2\pi\frac{\Delta x(x'n+y'm)}{\lambda f}}\end{aligned}\quad (2.6)$$

2.2.2 PSF reconstruction method

To measure the hologram PSF, a Mach-Zehnder interferometer was constructed. The interferometer was constructed as shown in Fig. 2-5. A HeNe laser at $\lambda = 632.8\text{nm}$ provided coherent illumination. Laser power was monitored from the first beam splitter. The laser beam was expanded and collimated by the spatial filter and convex lens. The beam quality was then checked with a shear-plate interferometer, then by using a mirror on both arms to interfere the reference with itself, minutely adjusting the beam quality until a perfectly flat interference pattern with no lateral fringes was obtained. The first half-wave plate and the polarizing beam splitter act to meter the amount of light that goes to each arm of the interferometer. The second half-wave plate then adjusts the polarization angle of the lower arm until it matches that of the upper arm. The first half-wave plate was adjusted until both arms had equal intensities immediately after the polarizing beam splitter. The second was adjusted until maximum fringe contrast was observed on the CMOS detector. The CMOS detector has a 4096×4096 format and a pixel pitch of $8\mu\text{m}$. It captures 8-bit monochromatic intensity data and was used with a shutter speed of 10ms. Hologram F1 was placed in one of the corners of the modified Mach-Zehnder, and was adjusted in angle until it produced the maximum diffracted power in the direction of the final beam splitter. The volume hologram was recorded at 488nm and contains a single recording of a plane wave grating at a 68° recording angle. The diffraction angle at 633nm is then $\sim 92^\circ$, so the arms were tilted slightly to form a parallelogram. The components in Fig. 2-5 are summarized in table 2-3.

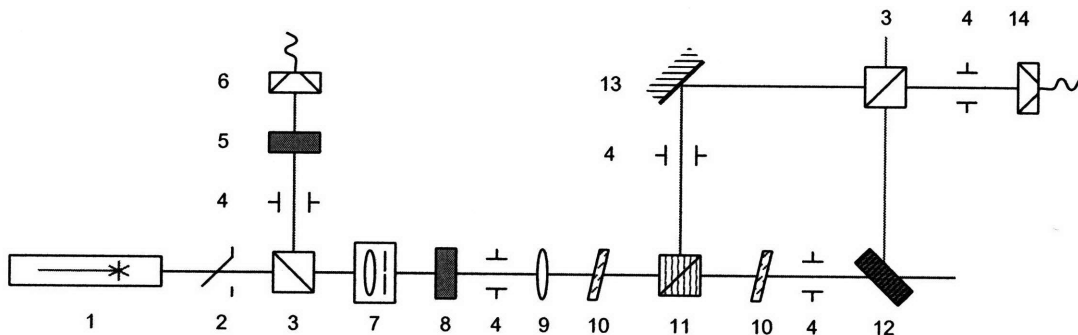


Figure 2-5: Modified Mach-Zehnder for PSF measurement. The components are described in table 2-3.

#	Description	#	Description
1	HeNe laser	8	ND filter, O.D.=1
2	Shutter	9	Biconvex lens
3	Non-polarizing beam splitter	10	$\frac{\lambda}{2}$ plate
4	Iris	11	Polarizing beam splitter
5	ND filter, O.D.=2	12	VH
6	Photodetector	13	Mirror
7	Spatial filter	14	CMOS detector array

Table 2-3: Summary of the components used in the modified Mach-Zehnder interferometer.

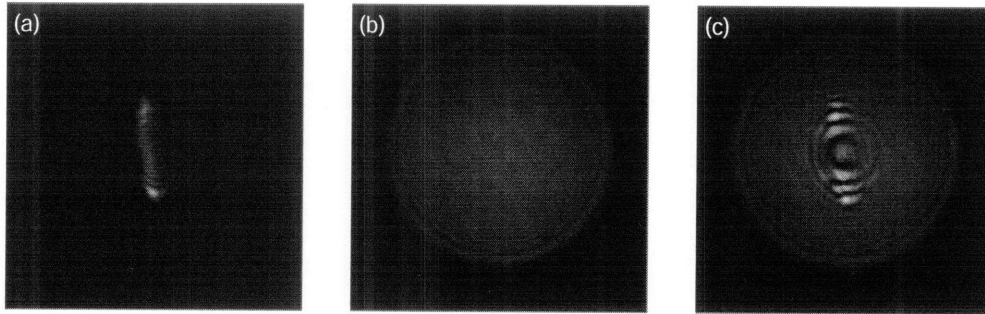


Figure 2-6: Interferogram and three components acquired from the interferometer setup in 2-5. (a) shows the diffracted beam from the hologram only, (b) is the reference only, and (c) is the interference pattern.

The interferogram and reference images were processed in Matlab[®] to reconstruct the phase angle. After the images were imported, several rows and columns on the edges of the images were removed from the calculation as they were zero-valued in each image. Additionally, all of the values in the images were normalized to the peak value in the interferogram. Despite this, there were a number of pixels with very low intensity around the edge of the illuminated region that had very low discrete values. These pixels, shown in Fig. 2-7(b), had a phase cosine above 1 or below -1. Because the CMOS detector is not continuous, and instead has 8 bits of precision, this behavior is possible where measured intensity is low. Nevertheless, this effect was limited to a very small number of pixels, and the real part of the phase angle in Fig. 2-7(a)

was used in the PSF reconstruction. The reconstructed PSF has some interesting structural

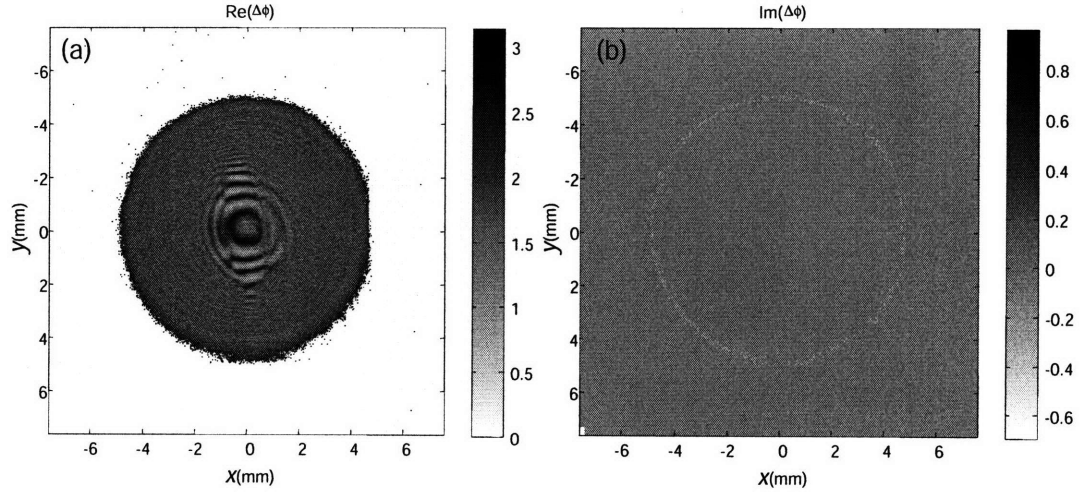


Figure 2-7: Phase angle reconstructed from the interferograms in figure 2-6. (a) is the real part of the phase angle, (b) is imaginary. A few pixels have imaginary phase components due to their low intensity values in each image and the discrete intensity levels of the camera.

elements. The central peak has a diameter that is just under one micron, which is essentially diffraction-limited for the wavelength used to probe the hologram. The sidelobes however are irregular beyond the vicinity of the central peak and show symmetry about a roughly vertical axis, but not radial symmetry. The dim vertical stripe in the sidelobes is the sinc-like Bragg slit that is aligned with the Bragg-degenerate axis of the hologram. The size and location of the Bragg slit can be predicted by formula 2.7 from [33].

$$w = \text{sinc}^2 \left[\frac{L \sin \theta_s}{\lambda} \left(\frac{x'}{f} - \theta_s \right) \right] \quad (2.7)$$

With parameters $L = 1.65\text{mm}$, $\lambda = \frac{633\text{nm}}{1.5}$, $f = 3.6\text{mm}$, and $\theta_s = 2 \arcsin \left(\frac{\sin(32^\circ)}{1.5} \right) = 41.38^\circ$, the FWHM of the central peak shown in Fig. 2-9 as a function of relative angle, is predicted to be $3.88\mu\text{m}$; this matches very well with the apparent width of the vertical stripe in the reconstructed PSF. Examination of the features in the reconstructed PSF reveals that the theoretical basis for expressing the various imaging properties of a VHI system is sound and well-matched with this experiment. To be even more thorough, it would be revealing to slightly tilt the

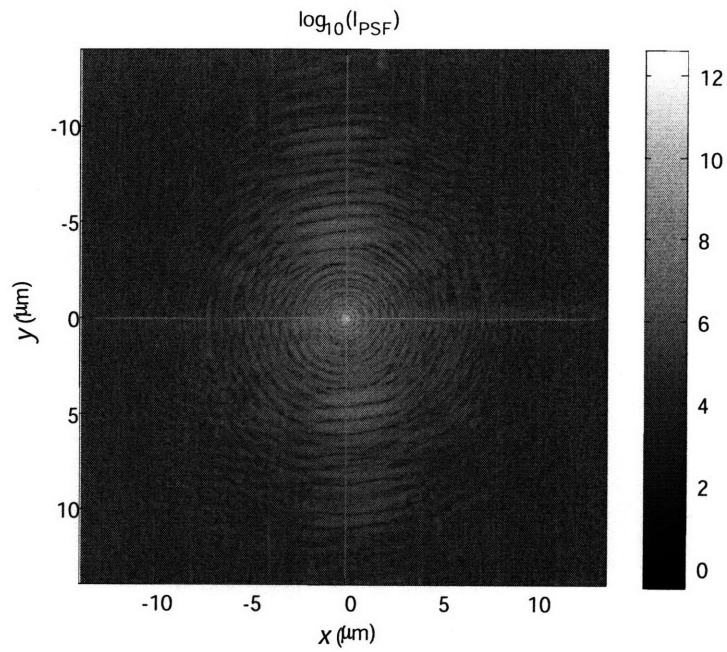


Figure 2-8: Reconstructed lateral PSF for hologram F1. The thin crosshair in the image is an artifact from the space-limited square domain of the DFT. Assumed focal length of the perfect collector lens was 3.6mm. Units are microns.

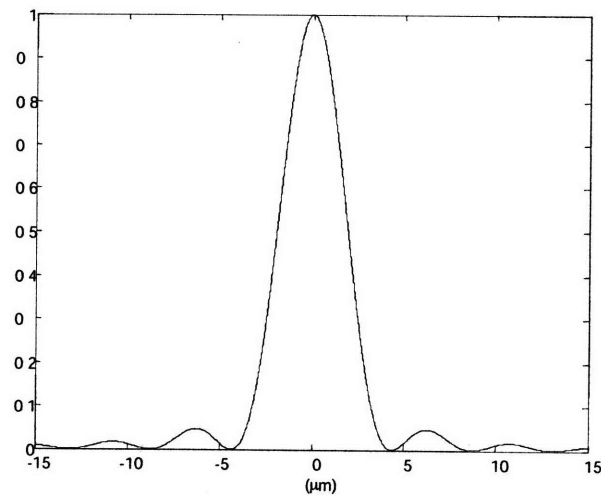


Figure 2-9: Theoretical cross-section of the holographic slit along the Bragg-selective axis transverse to the slit.

hologram with respect to the Bragg-matched position and then reconstruct the lateral PSF, which should reveal the Bragg slit shifting with respect to the central peak. Also, each grating of a multiplexed hologram could be evaluated in this way, and it would be interesting to see how the spherical wavefront reconstruction would interfere in the Mach-Zehnder. This would provide data that could possibly be used to improve simulations of depth selectivity or z-PSF.

2.3 Angular selectivity and diffraction efficiency

One of the defining behaviors of thick holograms is diffraction in the Bragg regime. The characteristic of Bragg diffraction is that constructive interference between structural features in a material can only occur under the particular circumstance in equation 2.8 from [31], where d is the unit distance between features, θ is the angle of the incident beam, and n is an integer.

$$2d \sin \theta = n\lambda \tag{2.8}$$

If the grating were infinitely thick, the function of diffracted power versus incidence angle for a plane wave would be a series of delta functions at $\pm n$. Under the condition of finite thickness however, we find that we do not have an infinitely narrow incidence angle for constructive interference. There is an angular range, albeit small, where reconstruction occurs. The strength of the reconstruction depends upon the thickness of the hologram and the refractive index modulation in the grating; it also depends upon factors that locally affect the grating vector such as the recording angle and wavelength, and also wavefront aberrations, including defocus, in both recording and reading the hologram. It is for this reason that it is worthwhile to investigate the range of acceptance angles, or angular selectivity, of the hologram. This reveals information about not only the grating quality and the efficiency of the hologram, but also information about field of view and sensitivity to alignment when the hologram is used in an imaging system. This quality directly affects the performance of the hologram as the system field stop.

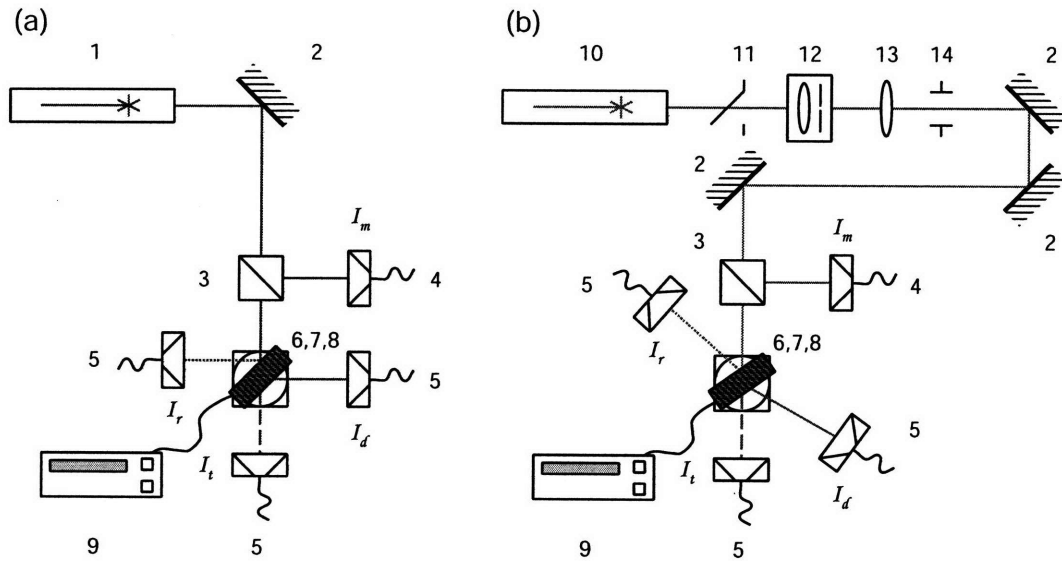


Figure 2-10: Configuration for performing the angular selectivity experiments. (a) is the setup used for probing the hologram at $\lambda = 632.8\text{nm}$; (b) $\lambda = 488\text{nm}$

2.3.1 Experimental procedure

The experiment to determine angular selectivity and efficiency for the holograms under test was performed at two different wavelengths: $\lambda = 488\text{nm}$ using a Coherent Innova 305 Ar^+ laser at 276mW, and $\lambda = 632.8\text{nm}$ using a Thor Labs HRP050 HeNe laser at 5.0mW. For each hologram, the angular selectivity was measured using a collimated beam probing the hologram along the conjugate axis, that is, reconstructing the signal beam by probing along the original reference, which is the opposite arrangement from the imaging case. This was done to ensure that the reconstruction was fully Bragg-matched for each grating in a multiplexed hologram, as a reconstruction of the reference arm would require a spherical wavefront in certain cases to match the recording conditions. If this is not done, the Bragg slit shifts across a large defocused spot, resulting in an unnaturally large angular selectivity. This method also had the benefit of being able to isolate individual gratings in the multiplexed case, as the signal arm reconstructions would occur individually for a given probe angle, rather than simultaneously. Fig. 2-10 shows the experimental setup for this test. Note that the Ar^+ laser emits into a shutter and a spatial filter assembly. The spatial filter was necessary for wavefront correction in expanding the laser beam.

These elements were also used to enhance safety by reducing the laser power, as it was very high directly out of the aperture. Another benefit to this arrangement is that the collimated beam in 2-10(b) is expanded and slightly larger than in 2-10(a); enough to completely fill the hologram aperture. Table 2-4 outlines the equipment used in this experiment.

#	Description	#	Description
1	HeNe laser	8	Tip-tilt mount (not shown)
2	Mirror	9	Newport ESP-300 Motion Controller
3	Non-polarizing beam splitter	10	Ar ⁺ laser
4	Photodetector → Keithley 480 picoammeter	11	Shutter
5	Photodetector → Keithley 6485 picoammeter	12	Spatial filter
6	VH	13	Convex lens
7	Newport ESP rotation stage	14	Iris

Table 2-4: Summary of the components used in the angular selectivity experiment.

The 6485 picoammeter has an operating accuracy of $\pm 0.5\mu\text{A}$ in the range used for these experiments. The 480 picoammeter was much more stable in the typical range used when monitoring laser power, its accuracy was $\pm 0.1\mu\text{A}$. The positioning accuracy of the ESP system was $\pm 0.001^\circ$, however the system had a drive backlash of about 0.03° , so care was taken to start a measurement series from the same direction and with sufficient overshoot. The dark current in the detector was found to be $< 0.1\mu\text{A}$, and therefore not significant in this experiment. The procedure used in the experiment is as follows. After the laser was stable, a photodetector was placed at the estimated diffraction angle. The hologram was then placed in the tip-tilt mount on the rotation stage and adjusted with all available degrees of freedom to produce the maximum detector current at I_d . This position was noted and then the rotation stage was set to a starting location some angular distance from this point and stepped toward and past the fully Bragg-matched angle until the detector current had returned to the level of the starting position, or to an equal distance from the peak as the starting position, whichever was farther from the peak. This was used to gather I_d data, the diffracted intensity. For each I_d data point, the monitor detector current I_m was read. This value was used to normalize the values of I_d

for fluctuations in laser power. This data set was repeated for a second time in each data set. Once this data was taken, the hologram was rotated back to the position of peak diffracted intensity and the detector was moved to a position in-line with the incident beam to measure I_i , the incident power and a monitor current reading, I_{mi} , was taken. Then the detector was moved to measure the reflected power from the front and back surface of the hologram, I_r . Again, a monitor current measurement, I_{mr} , was taken. Finally, the hologram was rotated to an angle just off from normal to the beam, and the detector was moved to the position directly behind the hologram to measure the photocurrent from the transmitted beam, I_t , and a monitor current measurement I_{mt} was read. To calculate the grating efficiency, the current at the diffraction and reflection positions was normalized with respect to the incident current using the monitor currents as in equation 2.9.

$$\begin{aligned}
 I_d^* &= I_d \cdot \frac{I_{mi}}{I_{md}}, \quad I_r^* = I_r \cdot \frac{I_{mi}}{I_{mr}}, \quad I_t^* = I_t \cdot \frac{I_{mi}}{I_{mt}} \\
 \eta &= \frac{I_d^*}{I_i - I_r^*}
 \end{aligned} \tag{2.9}$$

The transmitted intensity was used to estimate the absorption coefficient of the hologram, although this was only done for one of the holograms as the absorption was not deemed significant. The position of the detector for recording I_t was carefully selected so as to collect the reflection from the front and back surfaces of the hologram. This method does not calculate the two-pass attenuation of the reflected light from the second surface as it passes through the material. This effect was assumed to be negligible, but can be estimated using the theoretical reflectance of the material interface given by [52]:

$$R_{\perp} = \left(\frac{\sin(\theta_i - \theta_t)}{\sin(\theta_i + \theta_t)} \right)^2 \quad R_{\parallel} = \left(\frac{\tan(\theta_i - \theta_t)}{\tan(\theta_i + \theta_t)} \right)^2 \tag{2.10}$$

Given that the Ar^+ laser used in the experiment had a vertical polarization vector and the pq-PMMA of the holograms was uncoated, a good theoretical value of reflectance from the interface at $\lambda_p = 488\text{nm}$ is $R = 0.0624$. For $\lambda_p = 633\text{nm}$ however, the polarization vector was uncontrolled. With $R_{\perp} = 0.0951$ and $R_{\parallel} = 0.0064$; a precise theoretical value of the reflectance cannot be predicted if the polarization is unknown. The absorption was calculated

using equation 2.11, where T is the thickness of the hologram.

$$\begin{aligned} I_t^* &= (I_i - I_r^*) e^{-\alpha T} \\ \alpha &= \frac{-\ln\left(\frac{I_t^*}{I_i - I_r^*}\right)}{T} \end{aligned} \quad (2.11)$$

The error in the measured detector current was propagated to the calculated efficiency and absorption values using equation 2.12, where I_n is the intensity measured at various locations.

$$\Delta\eta(\theta) = \sqrt{\left(\sum_n \left[\frac{\partial\eta}{\partial I_n(\theta)} \Delta I_n\right]^2\right)} \quad (2.12)$$

2.3.2 Results and discussion

The experimental results are shown here in Fig. 2-11 through Fig. 2-15, and also summarized in tables 2-5 and 2-6. Summary data in table 2-5 were obtained using a spline interpolation, as data points did not fall exactly at the half maximum position, nor did they necessarily lie exactly at the angular position corresponding to peak diffracted intensity. These plots show the diffraction efficiency versus angle for both 488nm and 633nm reconstruction wavelengths. These plots are diffraction efficiency versus relative angle; that is, angle with respect to the peak efficiency value. For a symmetric planar wave hologram recorded at 488nm with a beam half-angle of 34.0° and reconstructed at 633nm, the diffraction angle is 46.5° , while it will remain at 34° if the reconstruction were to occur with $\lambda = 488\text{nm}$. Additionally, the multiplexed holograms were recorded with a 2.5° angular displacement in the reference arm between gratings, so the spherical and planar gratings do not reconstruct at the same lateral position. It should be made clear that the previous plots are therefore not showing the efficiency of the grating versus absolute angle. Table 2-7 contains data on the relative displacements between gratings for different wavelengths. These figures all show a response that is strongly Gaussian in appearance. Any apparent sidelobes are weak and are only visible in the 488nm result from hologram S9. The result of the angular selectivity experiment was expected to be generally described by equation

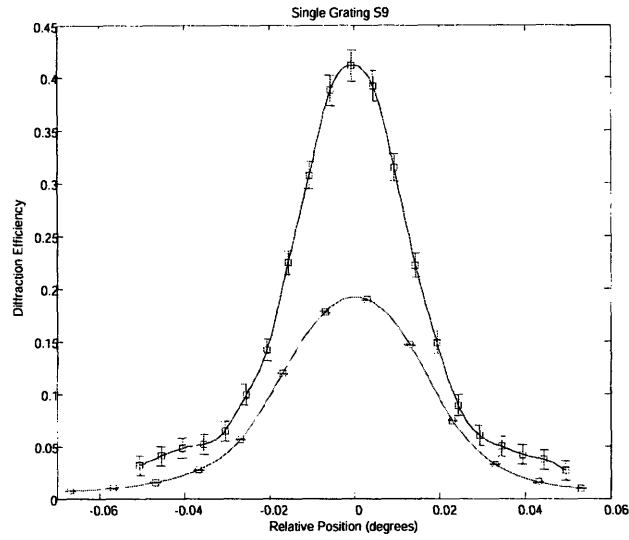


Figure 2-11: Diffraction efficiency versus relative angle for grating S9. Reconstruction at 488nm is shown in blue; 633nm in red.

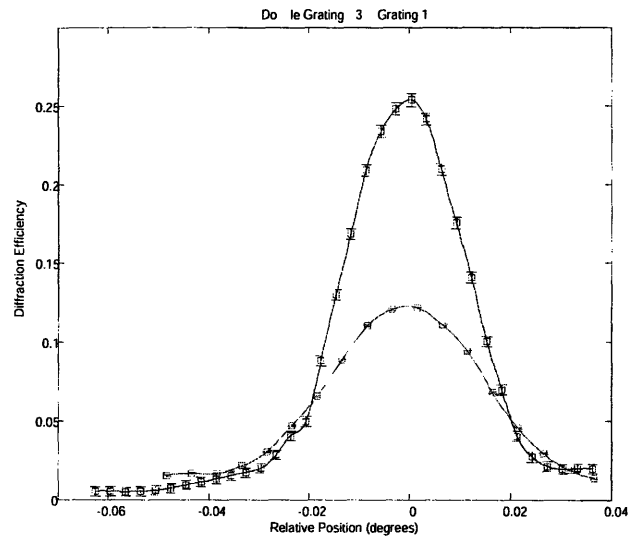


Figure 2-12: Diffraction efficiency versus relative angle for multiplexed grating F3A #1, a planar wave grating. Reconstruction at 488nm is shown in blue; 633nm in red.

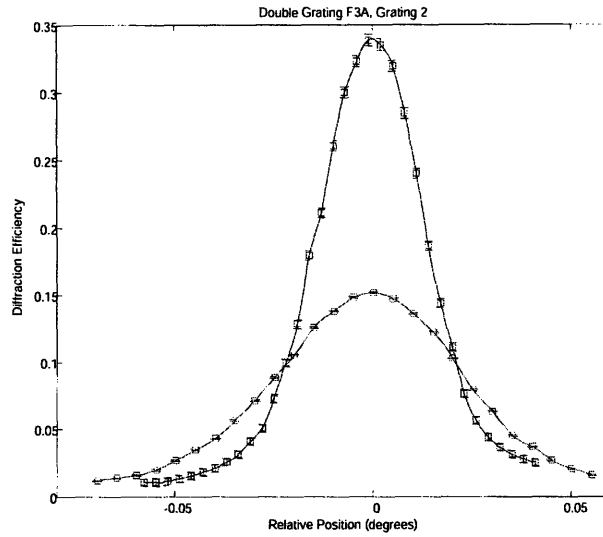


Figure 2-13: Diffraction efficiency versus relative angle for multiplexed grating F3A #2, a spherical wave grating. Reconstruction at 488nm is shown in blue; 633nm in red.

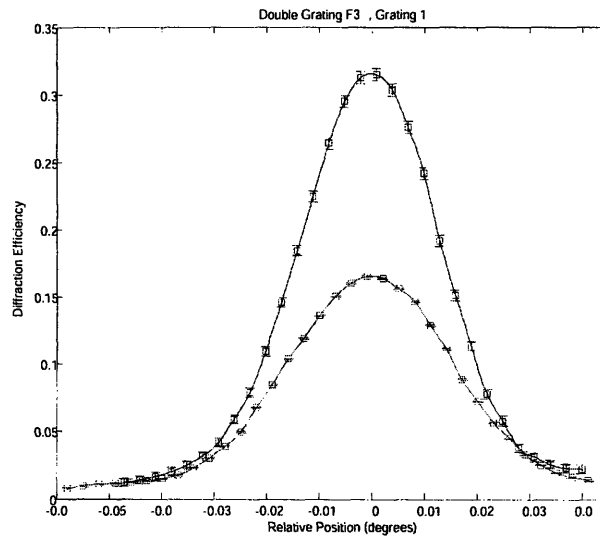


Figure 2-14: Diffraction efficiency versus relative angle for multiplexed grating F3B #1, a planar wave grating. Reconstruction at 488nm is shown in blue; 633nm in red.

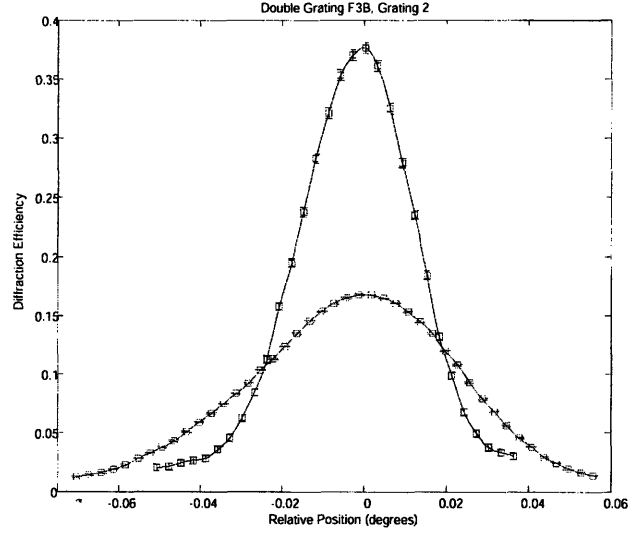


Figure 2-15: Diffraction efficiency versus relative angle for multiplexed grating F3B #2, a spherical wave grating. Reconstruction at 488nm is shown in blue; 633nm in red.

2.13 which is valid for a paraxial planar wave grating [34].

$$I_{\theta}(x) = \iint \left| \frac{\text{sinc}\left(r \frac{(x'+x_r)+(x-x_s)}{\lambda f_2}\right) \text{sinc}\left(r \frac{y'}{\lambda f_2}\right)}{\text{sinc}\left(L \frac{(x_r^2-x'^2)+(x^2-x_s^2)}{2\lambda f_2^2}\right)} \right|^2 dx' dy' \quad (2.13)$$

The paraxial prediction for the angular selectivity of hologram S9 at $\lambda_p = 488\text{nm}$ is shown in Fig. 2-16. The prediction uses $r = 1.8\text{mm}$, $L = 1.61\text{mm}$, and a construction half-angle of 34° . Note the similarity in curve shape, although the FWHM of the prediction at 0.041° is 0.009° larger than the measured value. Significant sidelobes may be present in the Bragg slit, however they are not pronounced in the angular selectivity curve as this function is the integral of the superposition of three separate sinc functions. Reconstruction at 633nm shows a weak similarity among all of the holograms studied; the FWHM versus 488nm reconstruction is ~ 1.5 times larger, and the peak diffraction efficiency is diminished by roughly 50%. The change in

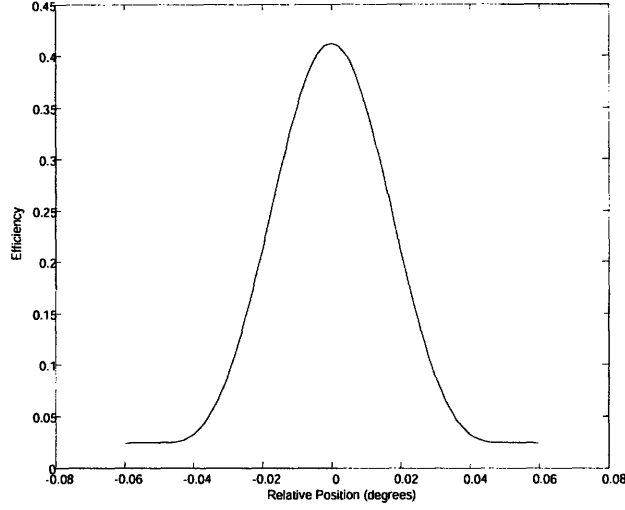


Figure 2-16: Paraxial simulation of hologram S9 at 488nm. Integrated intensity at the image plane as a function of angle produced by equation 2.13. More detailed non-paraxial simulations are discussed in chapter 3.

diffraction efficiency can be predicted by the Kogelnik equation 2.14:

$$\eta = \exp \left[-\frac{\alpha L}{\cos(\theta)} \right] \sin^2 \left(\frac{\pi L \Delta n}{\lambda \cos(\theta)} \right) \quad (2.14)$$

The peak-to peak change in refractive index $2\Delta n$ can be predicted by placing the recording terms in the equation: Let $\alpha = 4.5 \times 10^{-5}/\mu\text{m}$, $\lambda = \frac{.488\mu\text{m}}{1.5}$, $L = 1610\mu\text{m}$, $\theta = \arcsin \left(\frac{\sin(34^\circ)}{1.5} \right) = 21.89^\circ$, and $\eta = 0.412$. Then $2\Delta n = 8.72 \times 10^{-5}$. Using this value, we then solve for the efficiency at $\lambda' = \frac{.633\mu\text{m}}{1.5}$ with a new internal Bragg angle $\theta' = \arcsin \left(\frac{\sin(46.5^\circ)}{1.5} \right) = 28.92^\circ$ and the absorption coefficient $\alpha' = 3.76 \times 10^{-5}/\mu\text{m}$. This results in a diffraction efficiency $\eta = 0.295$ at 633nm, compared to the measured value of $\eta = 0.192$. Using the error analysis tool in 2.12, this prediction of efficiency has an error of ± 0.013 given the measured parameters it is based on.

Grating	$\lambda(\text{nm})$	FWHM (avg.)	η_{max}
S9 (planar)	488	$0.032 \pm 0.001^\circ$	0.412 ± 0.015
	633	$0.040 \pm 0.001^\circ$	0.192 ± 0.001
F3A #1 (planar)	488	$0.028 \pm 0.001^\circ$	0.254 ± 0.004
	633	$0.037 \pm 0.001^\circ$	0.123 ± 0.001
F3A #2 (spherical)	488	$0.032 \pm 0.001^\circ$	0.339 ± 0.006
	633	$0.055 \pm 0.001^\circ$	0.152 ± 0.001
F3B #1 (planar)	488	$0.032 \pm 0.001^\circ$	0.315 ± 0.005
	633	$0.037 \pm 0.001^\circ$	0.166 ± 0.001
F3B #2 (spherical)	488	$0.033 \pm 0.001^\circ$	0.376 ± 0.005
	633	$0.059 \pm 0.001^\circ$	0.168 ± 0.001
Ideal	488	0.041°	0.412
	633		0.295 ± 0.013

Table 2-5: Angular FWHM and maximum efficiency for each grating.

The low efficiency at long wavelengths is still unexplained at this time. It is possible that shrinkage or warping of the bulk hologram material induced some low frequency baseband into the grating that was not present in recording and to which the shorter wavelengths are not sensitive. It is also possible that pq-PMMA phase holograms have a strongly wavelength-dependent Δn not accounted for in eq. 2.14. It seems likely that the relatively large error in measuring the absorption coefficient of exposed pq-PMMA at $\lambda = 488\text{nm}$ contributes, however this error was propagated through eq. 2.14 and is not significant.

Location	$\alpha; \lambda = 488\text{nm}$	$\alpha; \lambda = 633\text{nm}$
F3B, Unexposed Region	$0.041 \pm 0.009/\text{mm}$	$0.0217 \pm 0.0007/\text{mm}$
F3B, Grating Region	$0.045 \pm 0.011/\text{mm}$	$0.0376 \pm 0.0008/\text{mm}$

Table 2-6: Absorption coefficients for grating F3B.

Hologram	$\lambda(\text{nm})$	$\Delta\theta$
F3A	488	$2.230 \pm 0.002^\circ$
	633	$2.778 \pm 0.002^\circ$
F3B	488	$2.543 \pm 0.002^\circ$
	633	$3.378 \pm 0.002^\circ$
Ideal	488	2.500°
	633	3.415°

Table 2-7: Angular distances between multiplex grating reconstructions.

The values in table 2-7 for the ideal case at $\lambda = 633\text{nm}$ were calculated using an Ewald sphere model described in more detail in chapter 3. The variation in the actual offset distances between gratings at $\lambda = 488\text{nm}$ is due to recording inconsistencies; the table shows that the reconstruction at 633nm occurs very close to the predicted location for that wavelength, at least in the case of hologram F3B. This is indicative of a carefully recorded hologram. The interesting result here is that detuning the hologram in wavelength also happens to detune the hologram in angle. That is, with a longer wavelength used in reconstruction than recording, a larger probe angle is required in order for the reconstruction to be Bragg-matched. This is true even between gratings in multiplexed holograms as shown above. The consequence in terms of imaging is that the reconstructions at different depths will also be laterally shifted under wavelength detuning; the imaged volume of material will have a parallelepiped geometry rather than cuboid.

2.4 Depth selectivity

The function of the hologram can be thought of as a phase-modulated transmission; the hologram contains pre-recorded information (the reference) on top of a local oscillator (the signal). When the signal arm of the hologram is probed, the incoming beam mixes with the pre-recorded local oscillator. If the spatial frequency of the probe beam matches the oscillator, part of the probe beam and the oscillator cancel each other and the information, the reference, is reproduced as it was recorded. One of the consequences of recording holograms in ever-thicker media

is that the bandwidth of spatial frequencies in this local oscillator becomes increasingly narrow, such that the reconstruction of the recorded information can only occur under similarly tighter conditions. This is the process behind the angular selectivity discussed in the previous section. Because this process occurs over the limited spatial extent of the hologram exposed to the probe beam, it applies to the entire spatial bandwidth, so the reconstruction is actually dependent on the quantity of the probe spatial bandwidth that matches the oscillator. In the case of a hologram probed by a point source through an objective lens where the point is placed away from the focal plane, the phase of the probe beam encountered by the hologram takes on a spherical shape. Depending upon how far the point source is defocused, the spectrum of the probe beam contains a variable amount energy that overlaps the bandwidth of the signal and produces diffraction in the hologram. This is the depth selective nature of VHs and was evaluated in the following experiment.

2.4.1 Experimental procedure

The purpose of this experiment is to determine the amount of diffracted energy produced when probing the VHI system with a point source at various locations around the objective focus. The depth selectivity experiment was carried out such that the hologram was kept in a fixed position while a point source, created in air by projecting a collimated beam through a corrected microscope objective, was translated across a grid of points positioned on a plane formed between the optical axis (\hat{z}) and the Bragg-selective axis of the hologram. This is the same plane that was formed between the two recording beams of a particular grating, and is also parallel to the horizontal plane in this experiment. A diagram of the component positions is shown in Fig. 2-17, and a list of the components is in table 2-7. Two wavelengths were used to probe the VH under test: $\lambda = 488\text{nm}$ using a Coherent Innova 305 Ar⁺ laser at 276mW, and $\lambda = 632.8\text{nm}$ using a Thor Labs HRP050 HeNe laser at 5.0mW. The hologram was nominally probed along the direction of its signal beam, just as in the imaging configuration for the holographic filter. These lasers were configured such that they each had a well-collimated and expanded beam from individual spatial filters. The beams from both lasers were combined using a non-polarizing beam splitter, and each beam was carefully aligned to ensure that both were coaxial. Once the beams were aligned, the rest of the optical train was emplaced. Careful

alignment and positioning of the VH is essential, so the hologram was placed on a computer-controlled rotation stage and inside a tip-tilt mount. To perform the experiment a single laser is un-blocked and beam is allowed to enter the optical system without the hologram. The translation stages are moved until the beam exiting the objective optics is parallel to the original beam path and is again collimated, at which point the VH is placed into its mount on the rotation stage. The rotation stage is then moved until a reconstruction is observed at the predicted angle for the given probe wavelength providing a rough angle for the Bragg-matched reconstruction. Then, the microscope objective located on the translation stages is removed, presenting the hologram with a beam converging to the rear focus of the objective optics. It is vital to position the hologram at the conjugate focal point, otherwise the probe beam cannot create a fully Bragg-matched reconstruction with the hologram, and may experience significant vignetting. Because of this, the beam waist is positioned as close to the center of the hologram aperture as possible, and centered between both external faces of the holographic material. In the experiment, the Ar^+ laser was used for this purpose as it was powerful enough to cause the pq-PMMA to fluoresce and the beam waist was easily observable. Once the hologram has been placed in the correct position, the microscope objective is replaced, and the hologram is rotated and tilted until the maximum diffracted intensity is measured. This is the fully Bragg-matched condition, and is the reference position for the point source displacements in further measurements. The rest of the experimental procedure was to raster-scan the linear stages along the $x - z$ plane, effectively shifting the projected point source in space around the focal plane of the imaging objective. The expanded beams entering the first objective were large enough to prevent vignetting.

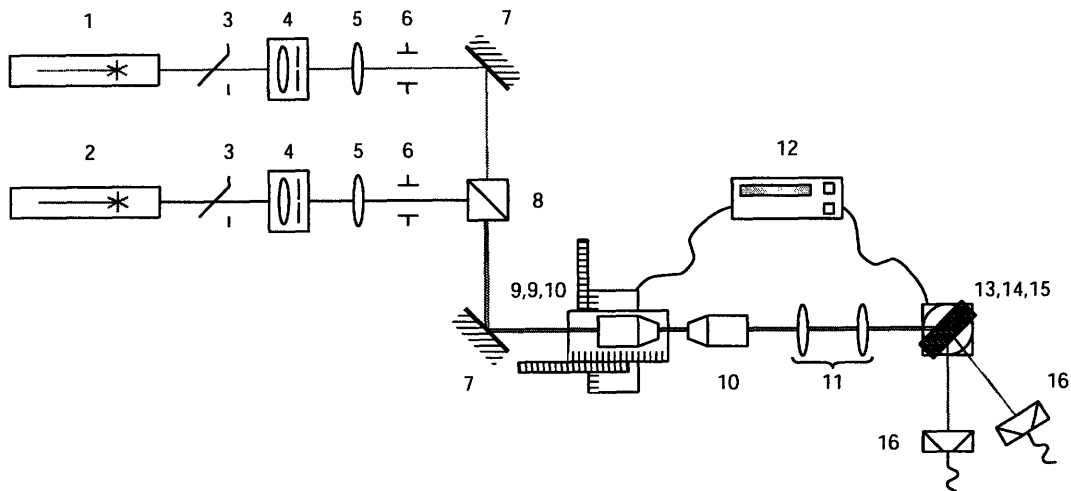


Figure 2-17: Configuration for performing the depth selectivity experiment. Beams were co-axial in the experiment, separation in the schematic is for visualization only.

#	Description	#	Description
1	Ar ⁺ laser	9	Newport ESP linear stage (x2)
2	HeNe laser	10	Microscope objective
3	Shutter	11	Relay optics
4	Spatial filter	12	Newport ESP-300 Motion Controller
5	Convex lens	13	Tip-tilt mount (not shown)
6	Iris	14	Newport ESP rotation stage
7	Mirror	15	VH
8	Non-polarizing beam splitter	16	Photodetector → Keithley 6485 picoammeter

Table 2-7: Components used in the depth selectivity experiment.

The Keithley 6485 picoammeter has an operating accuracy of $\pm 0.5 \mu\text{A}$ in the range used for these experiments. The positioning accuracy of the ESP system linear stages was assumed to be $\pm 0.1 \mu\text{m}$, although the encoder had one further significant figure. The linear positioning system had a drive backlash of about $5 \mu\text{m}$, so care was taken to start a measurement series from the same direction and with sufficient overshoot. The objective lens of the imaging system was a

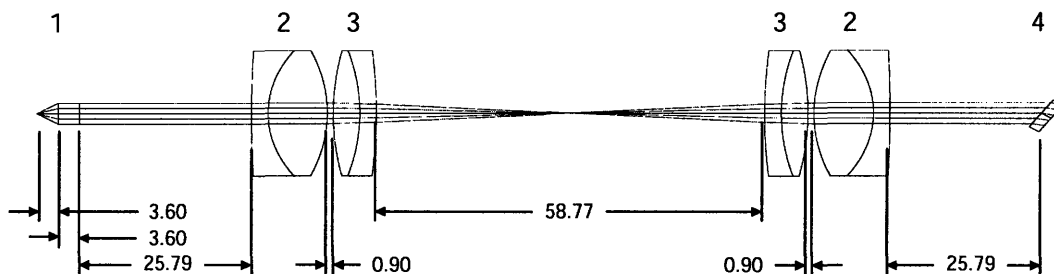


Figure 2-18: Configuration of the objective optics including the relay system. Figure was created from a ray tracing model in ZEMAX[®]. Units are millimeters.

microscope objective corrected for infinite conjugates with a numerical aperture of 0.55 and a focal length of 3.6mm. The ESP-300 motion controller as well as the picoammeter interfaced with a personal computer running a LabView program allowing the photocurrent and encoder data to be collected automatically. In each case, a grid of 40 points along \hat{x} by 50 points along \hat{z} were sampled. Holograms F3A, F3B, and F17 were evaluated in this experiment. The purpose of the relay system is to project the system stop to the hologram plane while minimizing beam diffraction and aberration. The configuration of the relay optics is shown in Fig. 2-18. These objective optics are the same as those used in recording the various gratings multiplexed in the hologram.

#	Description	#	Description
1	Corrected objective; $f = 3.6\text{mm}$, $NA = 0.55$	3	Thor Labs AC254-100-A1
2	Thor Labs AC254-050-A1	4	VH

Table 2-8: Components in the objective optics.

2.4.2 Results and discussion

The figures in this subsection show the detector current as a function of lateral and longitudinal position in the horizontal plane. In figs. 2-19 through , (a) shows the detector current as a function of $x - z$ position; the dashed white contour is the level where diffracted power is at 50% of the maximum. Units are in mA. (b) is a cross-section of all points sampled across

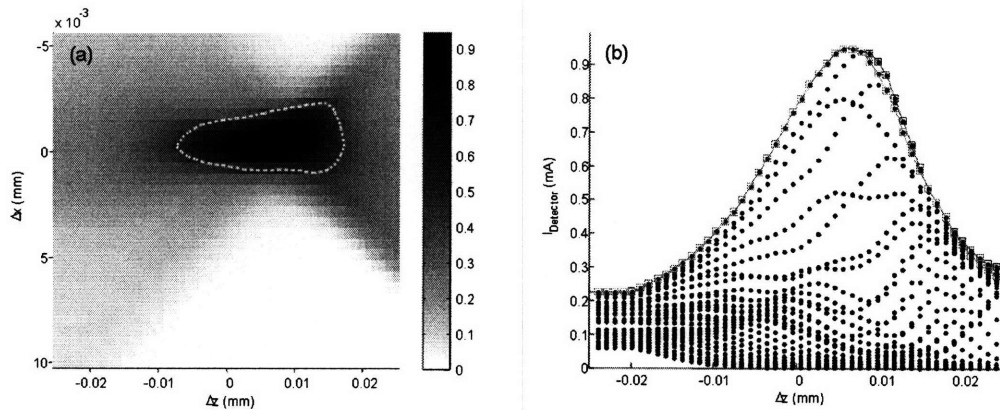


Figure 2-19: Response of VHI system using hologram F3A, grating #1 (planar) to a point source in the $x - z$ plane at $\lambda_p = 633\text{nm}$.

\hat{x} at sequential locations along \hat{z} . The envelope of maximum power recorded at a particular location z is shown in red. In other words, the red curve is the maximum possible response for a point source placed at a certain longitudinal position in object space. The green curve is the intensity along \hat{z} for the constant x -coordinate where the peak power was recorded; nominally an on-axis measurement. It is from these curves that the FWHM values in table 2-9 are found.

Grating	$\lambda(\text{nm})$	FWHM($x - z, \mu\text{m}$)	FWHM($z, \mu\text{m}$)	$I_d^{\text{max}}(\text{mA})$
F3A #1 (planar)	633	24.6 ± 0.1	24.6 ± 0.1	0.9480 ± 0.0005
F3A #2 (spherical)	633	22.5 ± 0.1	20.2 ± 0.1	1.8151 ± 0.0005
F3B #1 (planar)	488	12.9 ± 0.1	11.6 ± 0.1	33.212 ± 0.0005
F3B #2 (spherical)	488	10.1 ± 0.1	9.6 ± 0.1	75.623 ± 0.0005
F3B #1 (planar)	633	22.8 ± 0.1	18.2 ± 0.1	1.4928 ± 0.0005
F3B #2 (spherical)	633	21.7 ± 0.1	17.8 ± 0.1	2.0669 ± 0.0005
F17 #3 (planar)	488	10.5 ± 0.1	9.9 ± 0.1	30.296 ± 0.0005
F17 #3 (planar)	633	21.3 ± 0.1	17.6 ± 0.1	1.0289 ± 0.0005

Table 2-9: Summary of results from the depth selectivity experiment.

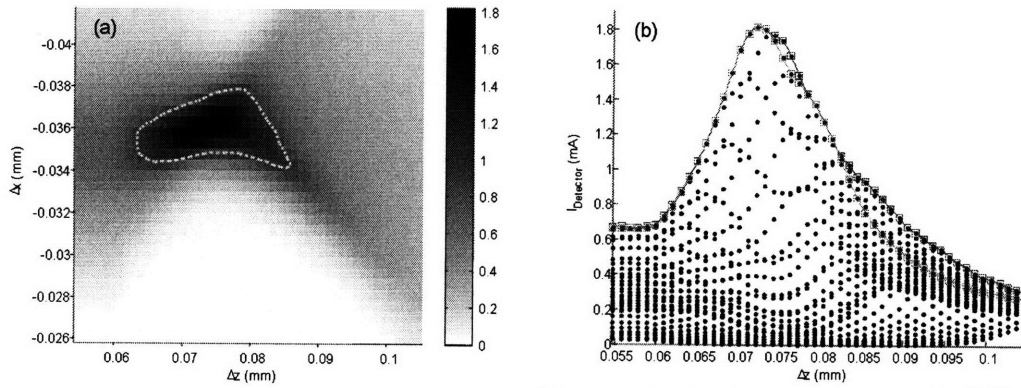


Figure 2-20: Response of VHI system using hologram F3A, grating #2 (spherical) to a point source in the $x - z$ plane at $\lambda_p = 633\text{nm}$.

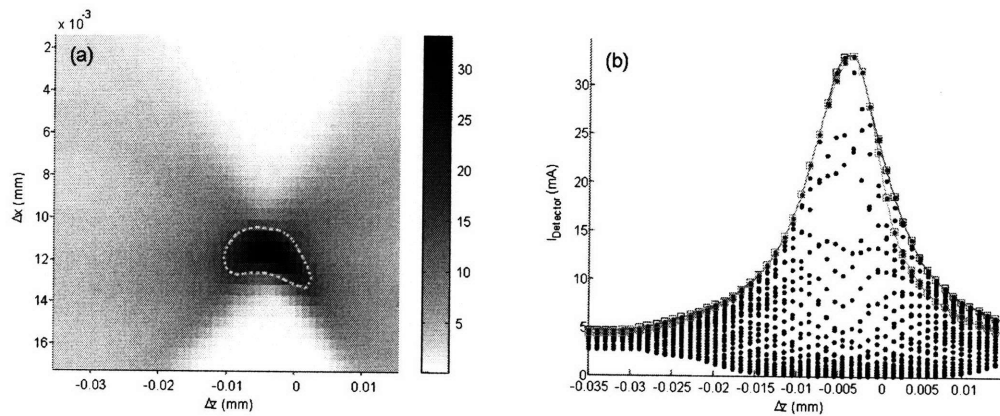


Figure 2-21: Response of VHI system using hologram F3B, grating #1 (planar) to a point source in the $x - z$ plane at $\lambda_p = 488\text{nm}$.

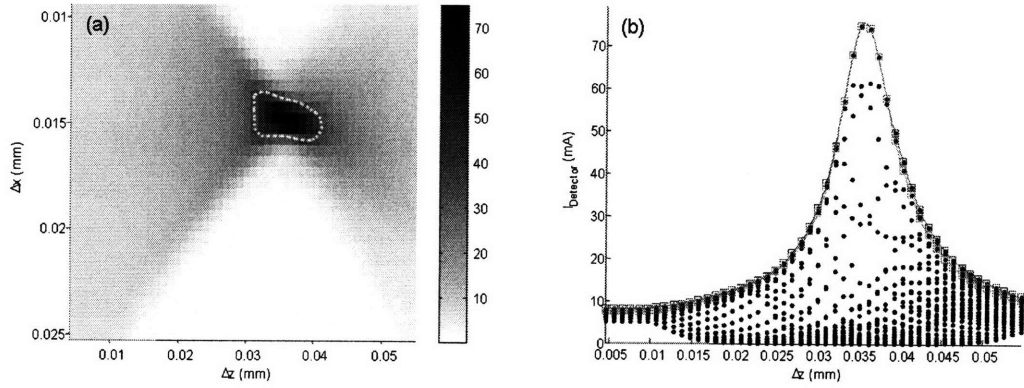


Figure 2-22: Response of VHI system using hologram F3B, grating #2 (spherical) to a point source in the $x - z$ plane at $\lambda_p = 488\text{nm}$.

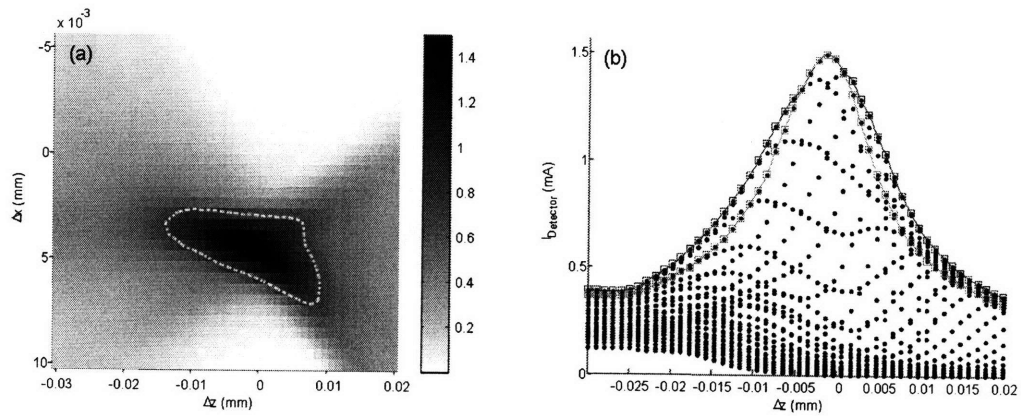


Figure 2-23: Response of VHI system using hologram F3B, grating #1 (planar) to a point source in the $x - z$ plane at $\lambda_p = 633\text{nm}$.

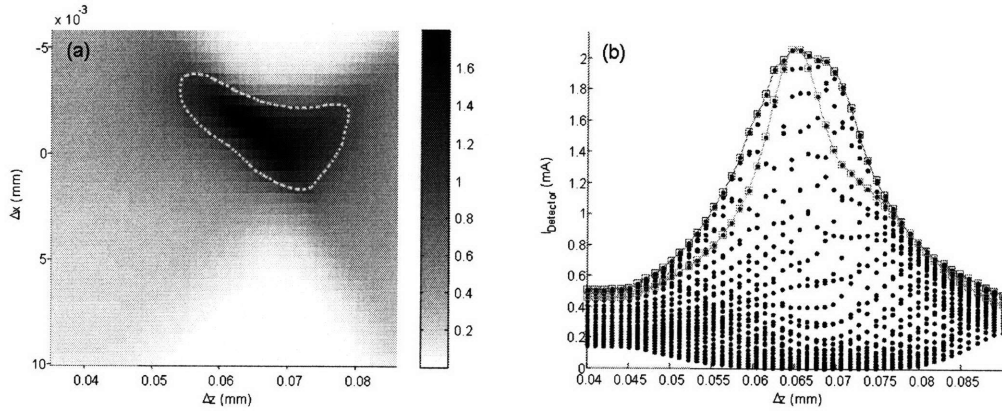


Figure 2-24: Response of VHI system using hologram F3B, grating #2 (spherical) to a point source in the $x - z$ plane at $\lambda_p = 633\text{nm}$.

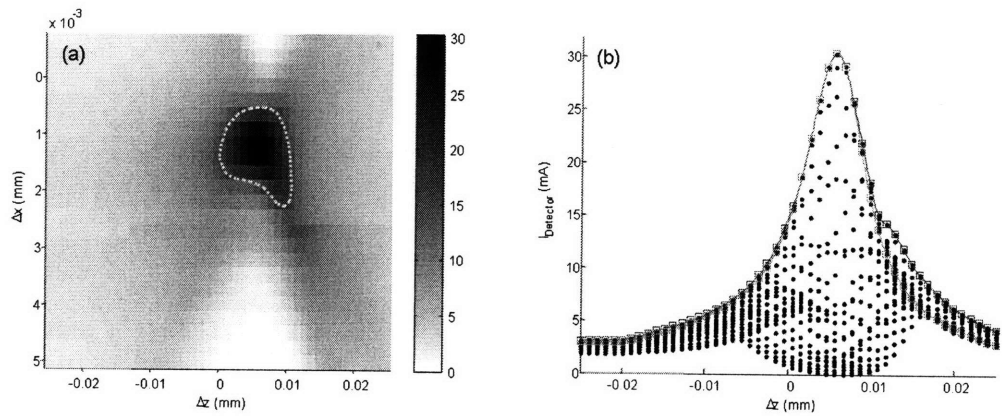


Figure 2-25: Response of VHI system using hologram F17, grating #3 (planar) to a point source in the $x - z$ plane at $\lambda_p = 488\text{nm}$.

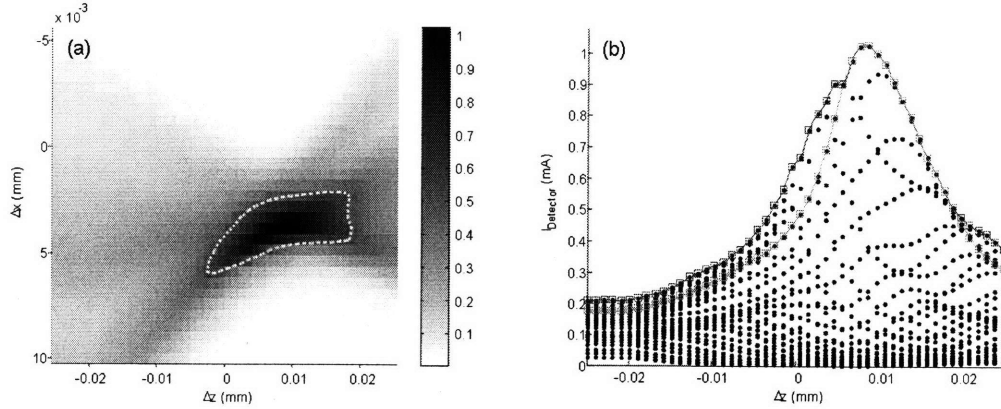


Figure 2-26: Response of VHI system using hologram F17, grating #3 (planar) to a point source in the $x - z$ plane at $\lambda_p = 633\text{nm}$.

The bell shape of the depth selectivity envelope was anticipated based on work in [33], [35], and others, as well as the modeling presented in chapter 4. One of the most prominent features in each of the figures is the "bow-tie"-shaped response to point source position. All of the gratings show this behavior, although in certain cases the bow-tie is tilted slightly with respect to the \hat{z} axis, which is likely due to a residual angular misalignment of the VH in the test fixture. The interpretation of this shape is simply that the image plane response of the hologram is similar to that of a standard imaging system screened by a fixed slit with a sinc cross-section [33]. While an off-axis point source might lie in the sidelobes of the sinc while in-focus and therefore be heavily attenuated, the conventional defocus response is essentially a larger diffuse spot and if the magnitude of the defocus is large enough, some of the spot is coincident with the center of the slit and some of this energy is diffracted. A geometrical optics approximation for this phenomenon was investigated in [33] and for planar reference gratings:

$$\Delta z_{FWHM} \approx \frac{5.34\lambda f_1^2}{\theta_s a L} \quad (2.15)$$

Let $\lambda = \frac{.488\mu\text{m}}{1.5}$ or $\lambda = \frac{.633\mu\text{m}}{1.5}$; $L = 1540\mu\text{m}$ (F3) or $L = 2170\mu\text{m}$ (F17); $\theta_s = 2 \arcsin\left(\frac{\sin(34^\circ)}{1.5}\right) = 43.78^\circ$, $f_1 = 3600\mu\text{m}$, and $a = 1800\mu\text{m}$. Table 2-10 shows the expected values for the Δz_{FWHM} .

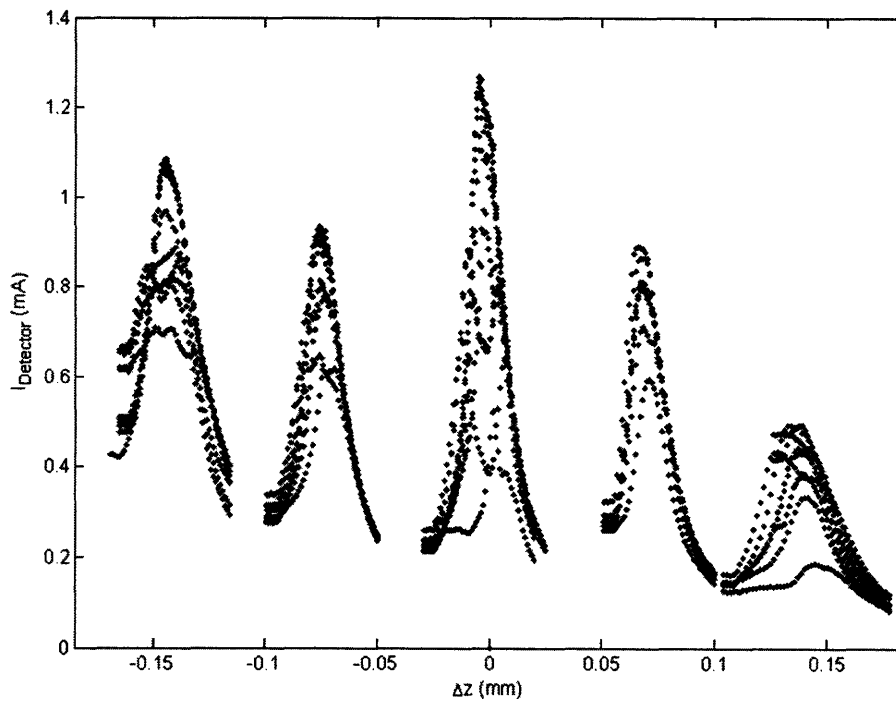


Figure 2-27: Cross section along x for all five gratings in hologram F17 versus defocus at $\lambda_p = 633\text{nm}$. Depth selectivity is roughly equal between gratings, while relative diffraction efficiency generally trends downward as the gratings reconstruct point sources closer to the objective lens. This was accomplished by varying the exposure time between gratings. Construction was at 488nm , with the signal arm focussed at $-100, -50, 0, +50,$ and $+100 \mu\text{m}$ along the optical axis.

Grating	$\lambda(\text{nm})$	FWHM($z, \mu\text{m}$)
F3(planar)	488	10.6
F17(planar)	488	7.54
F3(planar)	633	13.8
F17(planar)	633	9.79

Table 2-10: Theoretical depth selectivity.

While the theoretical result for the hologram depth selectivity does match fairly well for wavelength-matched reconstructions, it is clearly not as accurate in determining the reconstruction from the hologram with a wavelength mismatch condition. The effect of wavelength de-tuning on depth selectivity is much more severe than the geometrical optics approximation would indicate. The exact reason for the large difference in depth selectivity is unclear. It is possible that the method of scanning along \hat{x} as well as \hat{z} caused the depth selectivity to decrease. It is also likely that a physical effect in the VH, such as scattering, may be responsible. While the objective is corrected for infinite conjugates, it was not possible to obtain data on the proprietary configuration of the lens, so some unknown amount of aberration likely existed when the point source was moved away from the on-axis focal position. This is not seen as detrimental, since the VHI microscope is expected to be used with just such an objective, so this test is a valid measure of system performance. The data taken in this experiment is quite valuable as it gives insight into the ability of the hologram to function as a spatial filter. The theoretical response of VHS is discussed in greater detail in chapter 3.

2.5 Aberrated beams and depth selectivity

A VH might be utilized in any 4-f imaging system to provide spatial-spectral heterodyning. These systems, being composed of real lenses, will be subject to geometrical imperfections that give rise to aberrations. Especially in the case of a microscope with a high numerical aperture, the effect of the aberrations can be significant. Due to its spatially shift-invariant nature and effect on on-axis imaging, the effect of spherical aberration on the reconstruction beam of a planar-reference VHI system is examined here. Spherical aberration can arise from

the imperfect focusing of light by refraction through a spherical interface, especially with a small radius of curvature relative to the aperture of the interface. It can also occur when spherical converging or diverging phase fronts that encounter a flat dielectric interface, such as a microscope cover slip or the front surface of a VH recorded in photosensitive polymer. Spherical aberration is also present when imaging point sources located within optically thick dielectric media. The phase-conjugating property of the VH has been shown to ameliorate this effect when the recording process includes a section of thick media in the case of multiplexed holographic memories [32]. Aberrations can be represented as a deviation of the constant phase surface of a planar or spherical wavefront from the ideal form. This deviation, given in units of waves, is described by the aberration function Φ , which is a function of position in the pupil plane and contributes to the effective pupil function of the system. Primary spherical aberration is one realization of this function among the four others in the taxonomy of primary (Seidel) aberrations. Primary spherical aberration can be represented by the Zernike circle polynomials as in [31]

$$\Phi(\rho) = \frac{1}{\sqrt{2}} A_{040} (6\rho^4 - 6\rho^2 + 1), \quad (2.16)$$

where ρ is defined as the normalized pupil coordinate $\frac{r}{a}$ and A_{040} is the amplitude of the aberration. This aberration formula reveals the presence of quartic, quadratic, and constant phase factors. As the defocus aberration is defined as a spatially shift-invariant quadratic phase surface, this component of primary spherical aberration includes an effective defocus. Defining the effective defocusing of the system by the position that produces the maximum Strehl ratio, the defocus content of spherical aberration is [40]:

$$z_f = 6\sqrt{2} \left(\frac{r}{a}\right)^2 A_{040}. \quad (2.17)$$

Controlled amounts of spherical aberration can be added to a previously aberration-free wavefront in the following manner. Consider a truncated spherical wavefront diverging from a point source on the optical axis. In geometrical optics, this is represented by a fan of rays diverging from a single on-axis point. Placing a plane-parallel plate into the path of the ray fan and normal to the optical axis causes refraction in the spherical wavefront, and this can be traced by calculating the outgoing slope of each ray that is incident on the surface. Since the rays at

the outside of the diverging beam have a greater slope than those near the axis, the refraction is not a uniform effect, rather the change in slope of the outermost rays is more severe. This results in longitudinal spherical aberration; the focal position will be smeared along the optical axis [41]:

$$SphL(waves) = \frac{t}{n\lambda} \left(1 - \frac{\cos U}{\cos U'} \right), \quad (2.18)$$

where t is the thickness of the plate, n is the index of refraction, U is the external angle of the marginal ray, and U' is the internal angle of the marginal ray. The Seidel geometric aberration coefficient is then given by [41]:

$$A = \frac{-SphL}{a^4} \quad (2.19)$$

Corresponding to a Zernike coefficient A_{040} where m is the magnification between pupils [31]:

$$A'_{040} = -\frac{1}{4} \left(\frac{a}{m} \right)^4 A = \frac{SphL}{4m^4} = \frac{t}{4n\lambda m^4} \left(1 - \frac{\cos U}{\cos U'} \right) = \frac{6}{\sqrt{2}} A_{040}. \quad (2.20)$$

And:

$$\Phi(\rho) = A'_{040} \rho^4 = \frac{\rho^4 t}{4n\lambda m^4} \left(1 - \frac{\cos U}{\cos U'} \right) \quad (2.21)$$

$$\begin{aligned} A_{040} &= \frac{t\sqrt{2}}{24n\lambda m^4} \left(1 - \frac{\cos U}{\cos U'} \right) \\ &= \frac{t\sqrt{2}}{24n\lambda m^4} \left(1 - \frac{\cos(\arcsin(NA))}{\cos(\arcsin(\frac{NA}{n}))} \right). \end{aligned} \quad (2.22)$$

So it is clear then that the addition of a plane-parallel glass plate can add a controlled amount of spherical aberration to the system. Since these elements are quite commonly present in a microscope (e.g. cover slips), an experiment was performed to determine the impact of these elements upon the $x - z$ -selectivity of the VHI system.

2.5.1 Experimental procedure

This experiment is similar to the one described in section 2.4; the only difference being the placement of glass plates ~ 1 mm from the aperture of the objective lens. The plates used in this experiment are described in table 2-11. In the case of plates of intermediate thickness, several cover slips were stacked on each other and an index-matching microscope oil was placed between

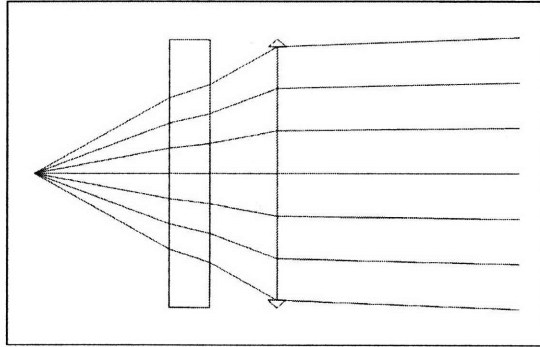


Figure 2-28: Configuration of the glass plate in front of the microscope objective.

them. The plates were borosilicate glass with a nominal index $n = 1.51$. The placement of the slide in the diverging beam in front of the objective lens was carried out before each data set was taken. Alignment and positioning of the slide is not critical, however the plate orientation was checked via retroreflection. The configuration of the glass plate in the aberration experiment is shown in Fig. 2-28.

Only hologram F3B was evaluated with this procedure.

2.5.2 Results and discussion

The figures below show each aberrated case along with the unaberrated response from the previous section. Each plot shows the diffracted power from a grating probed by a point source displaced parallel to the optical axis. ORG is the unaberrated case shown previously, 1CS has a single cover slip placed in the diverging beam, 4CS is a stack of four cover slips, 8CS is a stack of eight, and MS is a microscope slide. These curves represent the same type of measurement as the green curves in the previous section. The gratings with planar signal beams were used as a reference location for each curve. The spherical signal case was normalized in position to the location of the peak intensity in the planar signal. The peaks in the spherical signal case therefore show a small amount of displacement with respect to each other; this is an effect of the aberrated beam. Figs. 2-29 and 2-30 show the expected bell shape for the unaberrated objective optics with the response involving various amounts of added spherical aberration. Note that in Fig. 2-30(a), the peak response from the spherical signal case is located $40\mu\text{m}$

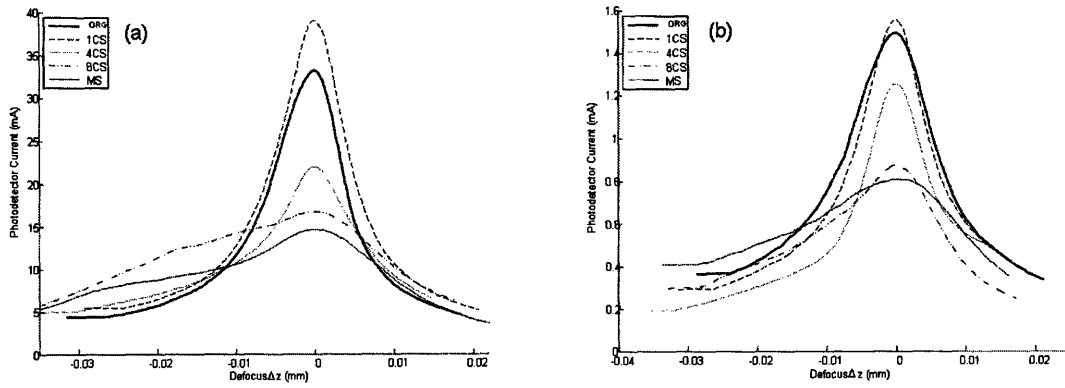


Figure 2-29: Diffracted power from grating F3B#1 (planar). (a) $\lambda_{probe} = 488\text{nm}$; (b) $\lambda_{probe} = 633\text{nm}$.

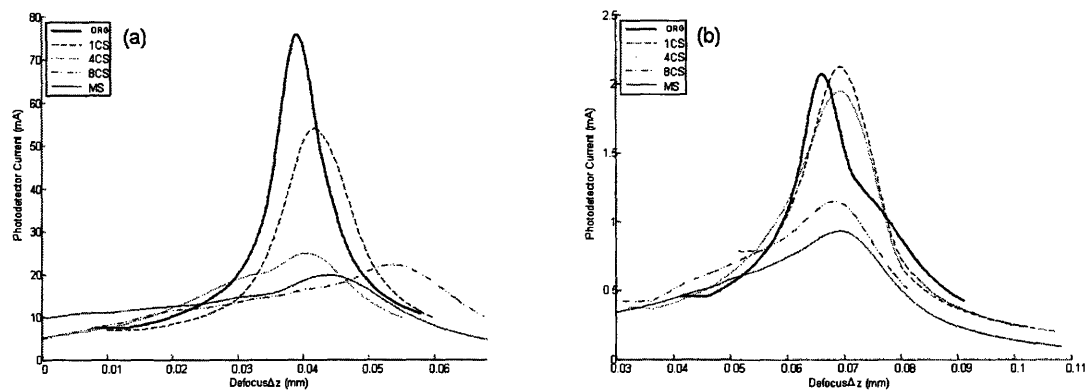


Figure 2-30: Diffracted power from grating F3B#2 (spherical). (a) $\lambda_{probe} = 488\text{nm}$; (b) $\lambda_{probe} = 633\text{nm}$.

closer to the objective than the planar signal case. By comparison, when recorded the point source was displaced $50\mu\text{m}$ for the spherical reference. The precise reason for this difference is not entirely clear, but is likely to involve mechanical strains in the pq-PMMA material present after developing. Small amounts of aberration, such as with a single cover slip, will increase the maximum diffracted intensity from the hologram in most cases. This has the related effect of decreasing the FWHM of the response curve. The response curve also begins to show a slight asymmetry; the side of the curve toward the effective defocus due to the spherical aberration, or positions further away from the objective in this experiment, show greater slope. Increasing the amount of aberration actually reverses this feature, such that each curve begins to show a long tail extending away from the objective lens. This is discussed further in chapter 3. Additionally, large amounts of aberration progressively diminish the peak diffracted intensity and increase the width of the response, reducing the depth selectivity of the VHI system. Note that the width of all curves representing longer probe wavelength is larger than the case of wavelength-matched reconstruction, and that the effect of spherical aberration is very similar for both probe wavelengths. Equation 2.21 was used to predict the coefficient of primary spherical aberration due to the presence of the plate, given $NA = 0.55$.

Type	$t(\text{mm})$	$A_{040}(\lambda = 488\text{nm})$	$A_{040}(\lambda = 633\text{nm})$
#0 Cover Slip	0.11 ± 0.01	0.91 ± 0.08	0.70 ± 0.06
#0 Cover Slip (x4)	0.43 ± 0.01	3.55 ± 0.08	2.74 ± 0.06
#0 Cover Slip (x8)	0.87 ± 0.01	7.18 ± 0.08	5.54 ± 0.06
Microscope Slide	1.24 ± 0.01	10.24 ± 0.08	7.89 ± 0.06

Table 2-11: Glass plates used in the aberration experiment.

Fig. 2-31 relates the aberration coefficient and peak diffracted intensity for each grating and probe wavelength in the experiment. Interestingly, this relationship is similar, within the measurement precision, for the spherical and planar signal gratings at 633nm. One of the interesting results from Fig. 2-32 is that the FWHM of the response curve actually decreases with a small amount of spherical aberration. The relationship is generally linear, although the spherical signal grating at 633nm is affected severely by the large amount of spherical aberration induced by the microscope slide in the objective optics; the FWHM of the response

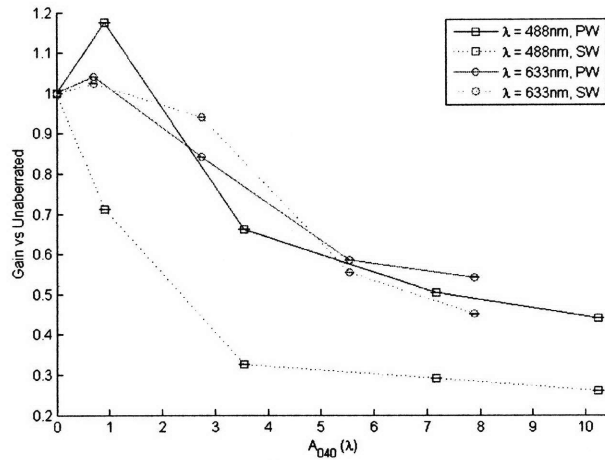


Figure 2-31: Relationship between peak diffracted intensity and aberration coefficient normalized to the peak value for the unaberrated case. PW is a planar signal beam grating, SW is a spherical signal.

became almost ten times larger than the cases with less aberration. This relationship is explored more fully in chapter 3. The conclusion from these experiments is that spherical aberration decreases the depth selectivity of the VHI system and reduces the power it transmits to a detector, although there are a few interesting cases where the opposite is true. This is the first experimental examination of the effect of aberration on a VHI system that has been carried out. There may be more possibilities for in-depth study, however. Although the light transmitted through the glass plate has a certain amount of spherical aberration that has been accounted for mathematically, the light that was reflected internally in the slide has been neglected. Although only a small fraction of the incident power, the wavefront of the twice-reflected light would appear to be flatter than the transmitted light, and the heterodyne behavior of the VH will cause this light to be diffracted as though it came from a point source that was placed behind the nominal focal position in object space. This reflected wavefront is also aberrated by the material interface. Placing a glass cover slip over a specimen will therefore decrease the dynamic range of the VHI system proportional to the thickness of the cover slip and the reflectivity of the material interface for the spectrum of incidence angles, but the magnitude of this effect has not been studied at present.

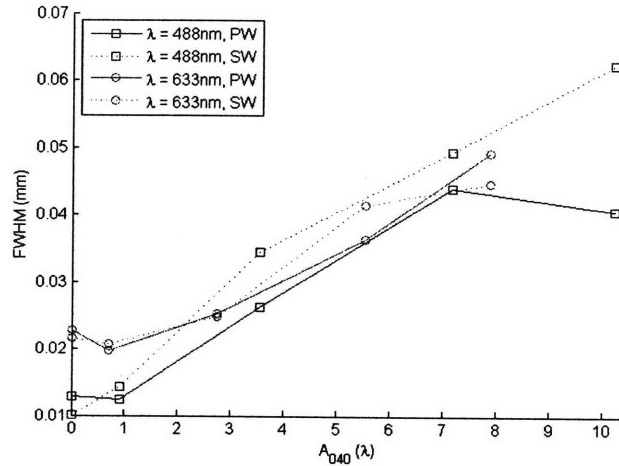


Figure 2-32: Relationship between aberration coefficient and FWHM of the response curve. Error in the FWHM for each value is $\pm 1\mu m$.

2.6 VHI micrographs

Acknowledgement 1 *The author would like to acknowledge the assistance of Prof. Ray Kostuk and colleagues Yuan Luo and Paul Gelsinger at the University of Arizona for their assistance in obtaining the VH images in this section.*

2.6.1 Resolution target images

A fluorescent resolution target composed of two non-symmetric vertically-stacked planar layers was described in section 2.1. This target, with $\lambda_{center} = 0.599\mu m$, was imaged using the VHI system with two gratings (F3B) and five gratings (F17) in the pupil plane. Fig. 2-34 shows two images from the two grating VHI system; the resolution target was positioned as shown in Fig. 2-33. The images in Fig. 2-34 were created by the VHI system and show the fluorescent resolution target as it appears on the image plane. Fig. 2-34(a) and Fig. 2-34(b) are images of the resolution target from a two-grating (F3B) VHI system showing the separation of the two target depth planes into two vertical "slices" in the image plane. The right-hand slice represents a depth plane closer to the objective lens. In each case, the target was illuminated by a UV laser at 300nm and imaged with an Andor iXon^{EM} 897 camera with a 512x512

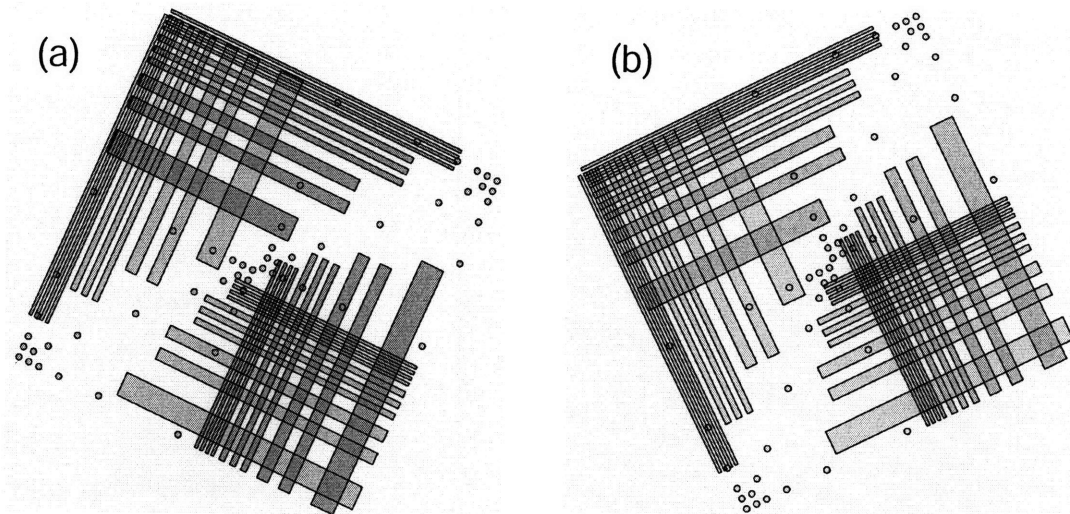


Figure 2-33: Arrangement of the resolution target layers as imaged in (a) figure 2-34(a) and (b) figure 2-34(b). The upper layer is colored green.

format detector array and $16\mu\text{m}$ pixel pitch. Layer separation in the target is approximately $60\mu\text{m}$. The hologram was recorded at 488nm with defocus positions of 0 and $-50\mu\text{m}$. The numerical aperture of the imaging objective is 0.55 . More sectioning capability can be achieved through the use of more multiplexed gratings in the VHI. The following images show the same resolution target as in Fig. 2-4 imaged with a 5-grating (F17) VHI system recorded at 488nm at defocus positions of -100 , -50 , 0 , 50 , and $100\mu\text{m}$. Several images are shown in Fig. 2-35 as the depth of focus of the objective lens is moved from above the target surface to a position underneath. These images reveal several important attributes of the imaging system. First, the lateral resolution is $\sim 7.5\mu\text{m}$ in most of the imaged section, as the series of four closely-spaced lines are just resolved everywhere in the image except for the extreme upper edge. Fig. 2-34 shows enough of the pattern that the field of view of a single Bragg slit can be determined. For the illumination condition described at the beginning of the section it is $340 \times 1280\mu\text{m}$. Second, the system displays a significant amount of inter-layer crosstalk. In the ideal case, light that is defocused with respect to a particular grating will be transmitted, although heavily attenuated by clipping across the Bragg-selective axis. While Fig. 2-35(a) for example shows the Bragg-selective behavior of the hologram (vertical slits are still visible), the intensity diffracted from the

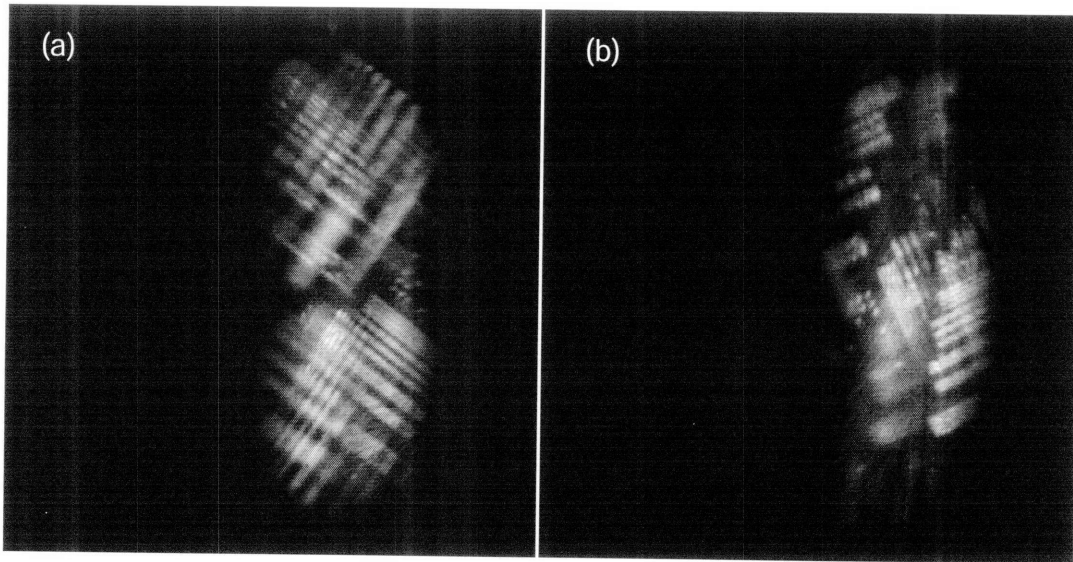


Figure 2-34: Image from VHI system incorporating two gratings. Image taken at 20°C detector temperature and 480msec exposure. (a) The orthogonal line sets between the left and right slices show in-focus images of the two target layers simultaneously. (b) This is an image of the same target as (a), but rotated counter-clockwise by $\sim 45^\circ$. Note the orthogonal sets of four narrow resolved lines and the alignment axes of the round dots. Also note the set of four lines at the upper extreme of the image is not resolved, indicating curvature of field. The vertical streaking in the image is due to residual QDs on the glass surface.

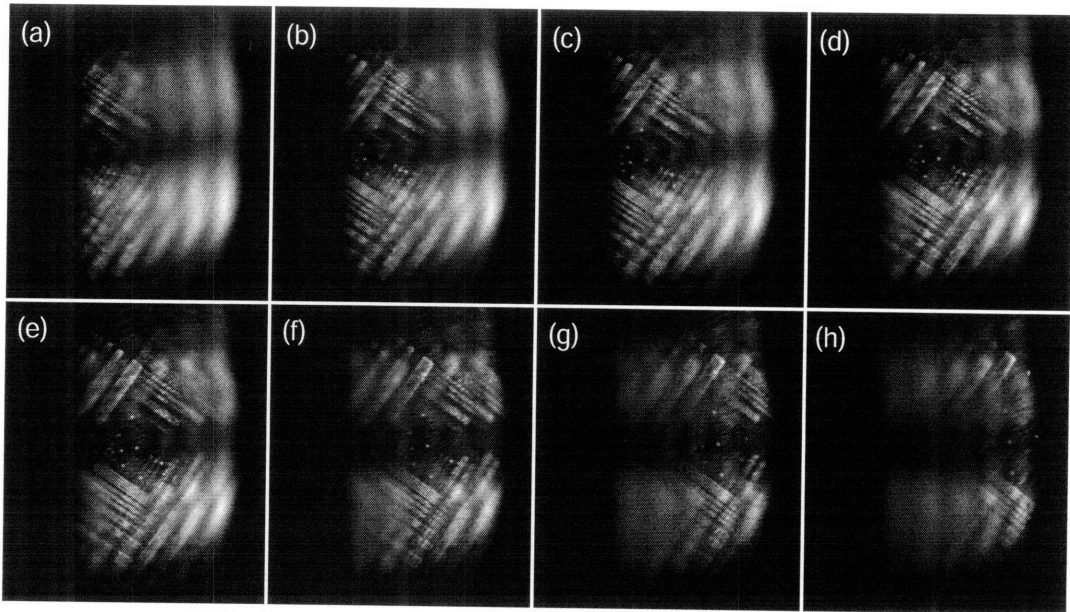


Figure 2-35: Image from VHI system incorporating five gratings. Image taken at 20°C detector temperature and 400msec exposure. **(a-h)** Show the effect of moving the depth of focus downward through the sample. The slice at the far right represents the upper-most depth plane.

out-of-focus gratings still appears to be significant. The inter-layer cross talk is also evident in the ghost images seen inside layers in-focus. The hologram can be made more selective through an increase in thickness, a higher Δn in the grating, or an increase in numerical aperture.

2.6.2 Onion peel images

Because the purpose of the VHI system is to image highly scattering biological tissues with generally less structure than that of the resolution target, an estimate of the imaging performance in more realistic conditions requires a different object. A convenient representative material is thinly-sliced onion peel, which contains large and easily discernible cellular structures. A series of images of different sections of onion peel are shown in Fig. 2-36. These are raw images that have not been enhanced. The method for imaging this purely scattering, i.e. non-fluorescent sample was the same as in section 2.6.1 except that the sample was illuminated from above by a high-output LED source with a center wavelength of $\lambda = 630\text{nm}$, and the backscattered light was collected from the sample. In Fig. 2-36, the cellular boundaries are easily discernible throughout the image. These images were obtained using the 5-grating (F17) VHI system. At 630nm, the center spacing in depth between the reconstructed slices occurs approximately at positions $\Delta z = -150, -75, 0, 75, \text{ and } 150\mu\text{m}$. These Δz values represent larger inter-layer spacing than the spacing recorded in the hologram due to the longer wavelength used to illuminate the specimen. Also, the longer wavelength increases the visible thickness of each layer to $\sim 25\mu\text{m}$. Note that the layers are very clearly defined with minimal ghosting as seen in the resolution target images. This may be due to the larger optical flux received from the onion sample resulting in a shorter exposure time. It is also possible that in the case of the resolution target the VH exhibits more internal scattering at the 599nm emission wavelength of the resolution target, or that reflected 300nm illumination from the excitation source causes the VH itself to fluoresce. Also, the Bragg slits exhibit some shallow curvature. Given a pixel pitch of $16\mu\text{m}$, the radius of curvature of the center slit was estimated to be 14.7mm.

2.6.3 Image processing

The processing of VH imagery is fairly straightforward in situations where no degeneracy exists; the physically separated image components are simply isolated and recombined at their correct

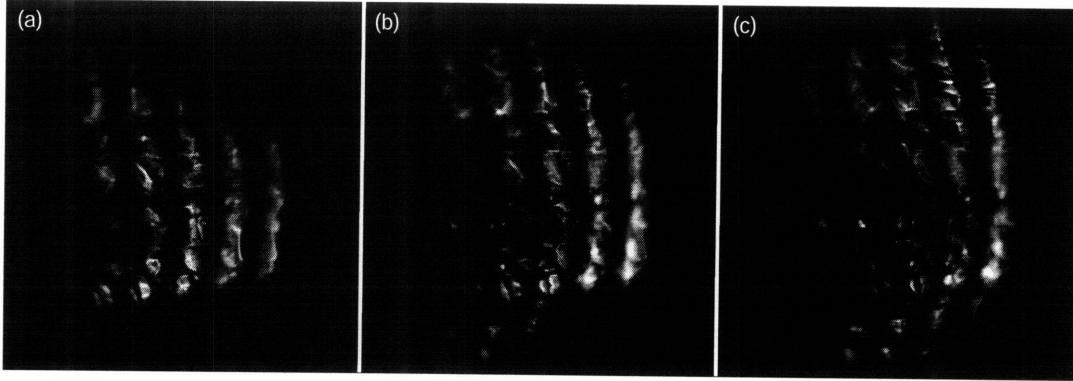


Figure 2-36: VHI image of onion skin. Each image is from the same general region of the sample. Each image shows a sample shifted to the right by $50\mu\text{m}$ relative to the previous image: (a) $\Delta x = 0$; (b) $\Delta x = 50\mu\text{m}$; (c) $\Delta x = 100\mu\text{m}$. Exposure time 350ms.

positions in object space. More general image processing techniques may be used before recombination such as background subtraction or edge detection; both of these techniques are used in this work. It was found to be necessary to image a region of the target that is completely out of focus in order to locate the edges of the Bragg reconstructions in the image plane. This process is shown in Fig. 2-37. The reconstructions are separated by thresholding the defocus image and decomposing the image into vertical line elements. This decomposed image is thresholded and the largest interconnected objects are coded and placed into a binary mask. This mask is then used to process all subsequent images; this procedure is only necessary once given an object with a static spectral bandwidth. Once the mask is generated, the raw images can be used directly, however it is sometimes necessary to use the defocus image as a background layer and then subtract this "background" from the raw image. Also, it is sometimes desirable to apply an edge enhancement to the raw image. This process was applied to the processed images of the resolution target since they generally consist of rows of straight lines. The edge enhancement used here is convolution with the Sobel operator, which approximates the gradient of the image

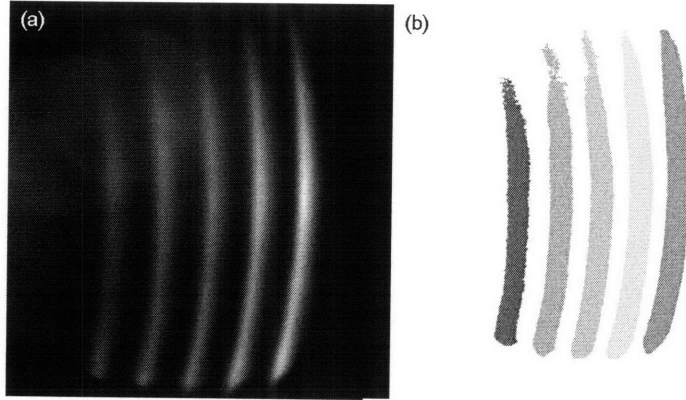


Figure 2-37: Determining the location of the Bragg reconstructions for various object locations. (a) Defocused object image. (b) MATLAB[®] processed image showing the reconstructions automatically distinguished from each other.

and has the form:

$$\begin{aligned}
 S_x &= \begin{bmatrix} 1 & 0 & -1 \\ 2 & 0 & -2 \\ 1 & 0 & -1 \end{bmatrix}, S_y = S_x^T \\
 I_{new} &= \|S_x \otimes I_{orig} + S_y \otimes I_{orig}\|_{L_z} \approx \nabla I_{orig}
 \end{aligned} \tag{2.23}$$

The reconstructions in Fig. 2-38 show the result of processing the images in Fig. 2-35(e-g). These reconstructions make use of convolution by the Sobel operator; the various reconstructions actually show an approximate gradient of the raw image of the resolution target. The reconstructions in Fig. 2-39 show a more conventional processed image of the onion peel. Performing reconstructions on the various images is an important first step toward developing similar tools that will enable users of VHI systems to operate with a 3-D display in real time. In many cases, the raw imagery will be of little help to a human in real-time imaging tasks. VHI systems are capable of measuring large amounts of spatial and spectral data in parallel so it will be very important to develop display methods that do not encumber the system with unnecessary overhead yet are fast, easy to use, and accurate.

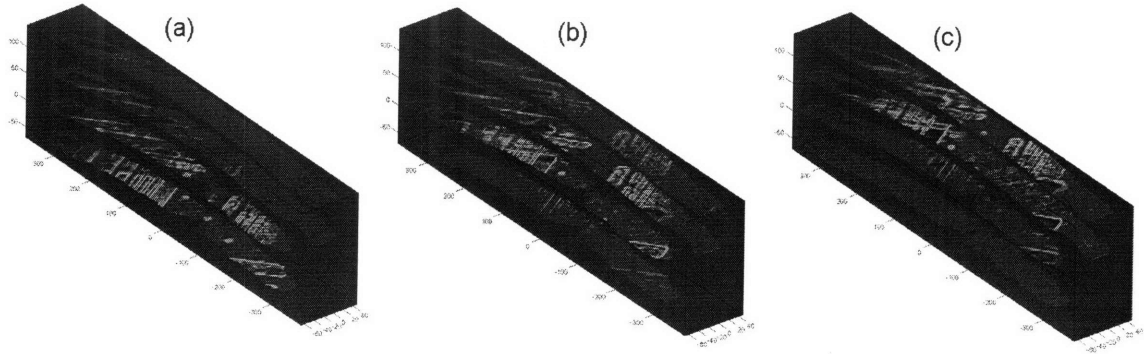


Figure 2-38: Three reconstructions of the 2-D image plane intensity in Fig. 2-35(e-g) as the focal depth of the objective progressed through the resolution target. These images were processed using the Sobel edge enhancing filter and background subtraction. Crossed lines in adjacent depth planes show the depth discrimination capability of the VHI system. Units are in μm .

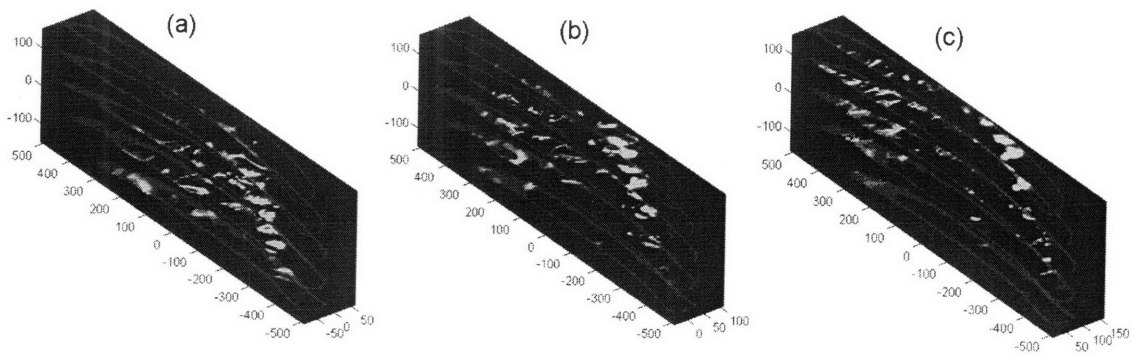


Figure 2-39: Processed images of onion peel from Fig. 2-36. Note that certain structural details are represented in multiple depth slices. Units are μm .

Chapter 3

Simulating VHI Systems

If the full potential of a VHI system is to be realized, the system must be engineered to provide the best possible image quality and spatial-spectral selectivity. While a vast number of different holographic filters could be constructed to find the solution space of the design, it is more practical to create a simulation architecture that allows most operating conditions and configurations to be tested. The first part of this chapter discusses the mathematical basis for constructing simulations and contains closed form solutions to a few idealized cases. Similar derivations have appeared elsewhere [33][34], however this chapter focuses on the case of an unslanted grating in imaging, which has not been examined in any great detail before. After the introduction of the relevant mathematical tools, attention shifts to a novel VHI simulation that was created using Matlab[®] which is capable of modeling arbitrary optical components through interaction with Zemax[®] models. Zemax[®] is a commercial lens design package. While a rigorous coupled wave (RCW) simulation will provide very accurate calculations of diffracted intensity, it must operate under certain idealizations of the optical system and hologram [45]. By contrast, the weak diffraction model provides greater flexibility in the simulation of the objective optics and VH at the expense of accuracy in diffraction efficiency.

3.1 Weak diffraction and transmission volume holograms

Volume holograms and other gratings that are optically thick will undergo Bragg diffraction. The criterion for determining the thickness of a grating is given in [35]:

$$Q = \frac{\lambda d}{\Lambda^2}, \quad (3.1)$$

where λ is the wavelength inside the bulk hologram material, d is the hologram thickness, and Λ is the period between fringes. Thick gratings will be those with $Q > 1$. Also from [35], the parameter $\Lambda = \frac{2\pi}{|\vec{K}|}$ where $\vec{K} = \vec{k}_r - \vec{k}_s$; \vec{k}_r is the wave vector for the reference beam, and \vec{k}_s is the wave vector for the signal beam. In the case of two plane waves, the grating period is given by $\Lambda = \frac{\lambda}{\sin \theta_r - \sin \theta_s}$.

3.1.1 The K-sphere

We can use the definition of grating vector and eq. 2.8 to construct a purely geometrical model of the diffraction process. This model is called the K-sphere or Ewald sphere [31]. From [42]: In the K-sphere formulation, each plane-wave component vector \vec{K}_g of a VH is defined as the vectorial sum of a reference wave-vector \vec{k}_r and a corresponding signal wave-vector \vec{k}_s , each of magnitude $\frac{2\pi}{\lambda}$, where λ is the wavelength of the reference and signal beams. When \vec{K}_g is probed by a plane-wave component \vec{k}_p in the probe field, the qualitative nature of the diffracted field is established by forming the vector $\vec{k}_d = \vec{k}_p + \vec{K}_g$. If \vec{k}_d is placed with its origin on the center of the K-sphere and its tip falls on the K-sphere, it indicates that the probe is Bragg-matched to the hologram. Since the radius of the K-sphere is $\frac{2\pi}{\lambda_p}$, the Bragg matching condition guarantees a propagating free-space mode; the corresponding plane-wave component of the diffracted field is in the direction of \vec{k}_d and the maximum diffraction efficiency allowed by the index modulation, thickness, and absorption of the holographic material is obtained. Otherwise, the diffraction efficiency is further attenuated by an amount

$$\eta \propto \text{sinc}^2 \left(\frac{L \left(\vec{k}_p + \vec{K}_g - \vec{k}_d \right) \cdot \hat{z}}{2\pi} \right) = \text{sinc}^2 \left(\frac{L \delta \vec{k}_d \cdot \hat{z}}{2\pi} \right); \quad (3.2)$$

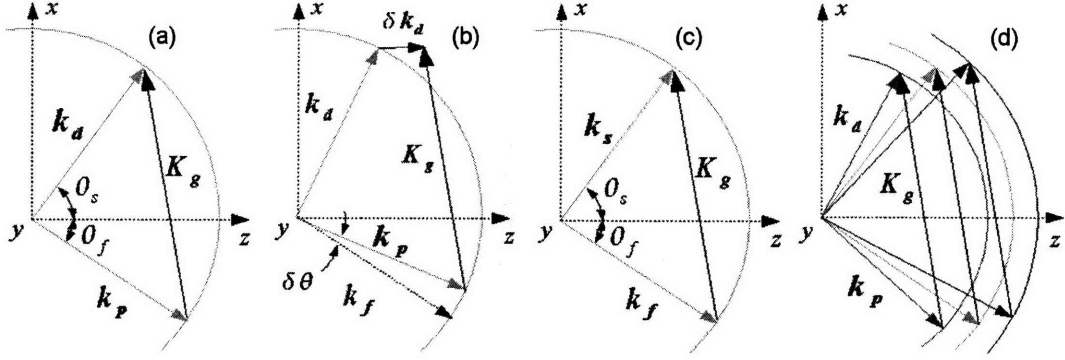


Figure 3-1: Geometric construction of volumetric diffraction using the K-sphere model. (a) construction of the grating vector from the recording wave vectors. (b) Bragg-matched reconstruction at $\lambda = \lambda_p$. (c) Bragg mis-match at $\lambda = \lambda_p$. (d) wavelength degeneracy; Bragg-matching holograms at different probe wavelengths (after [42]).

the corresponding diffracted plane wave component is in the direction of $\vec{k}_d - \delta\vec{k}_d$ [43]. In eq. 3.2, L is the thickness of the VH. Bragg-matched reconstruction occurs any time the tip of the vector $\vec{k}_p + \vec{K}_g$ lies on the sphere with radius $\frac{2\pi}{\lambda_p}$. It should be clear that the wave vectors used to construct or probe the hologram in the K-sphere approach need not be single vectors but may represent angular spectra, frequency spectra, or both. Given this fact and eq. 3.2, it would be possible to estimate a diffraction efficiency for non-paraxial conditions including geometric aberrations; this particular approach was not used in this work, however. Fig. 3-1 from [44] shows this process for wavelength degeneracy. The K-sphere is a very valuable tool for solving analytically for the required wave vector \vec{k}_p for reconstructing the reference beam under generally idealized, but not paraxial, conditions, and for visualizing the outcome of the diffraction process. This construct is used later in the non-paraxial Matlab[®] simulation to solve for the proper probe beam angle for a Bragg-matched reconstruction.

3.1.2 Weak diffraction

Let (x, y, z) be coordinates in the vicinity of the pupil of a 4- f optical system, where z is the optical axis; x and y with z define the sagittal and meridional planes, respectively. Furthermore, let (X, Y) be coordinates in the image plane behind the final collector lens, perpendicular to the optical axis. Given an object phase delay and amplitude function $\varepsilon(x, y, z)$, and a probe field

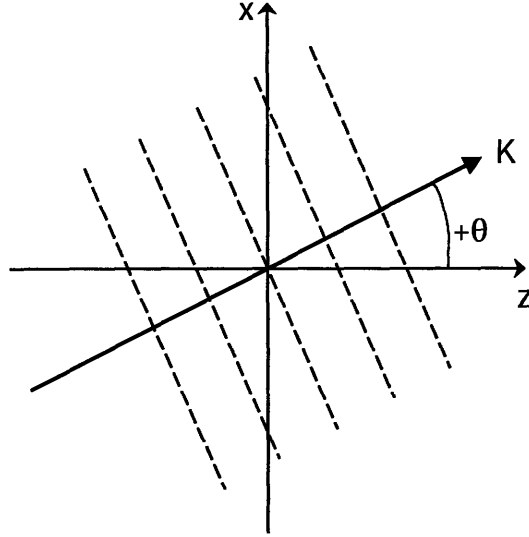


Figure 3-2: Convention used for defining angles in a phase profile. Dashed lines represent constant phase, and K is the wave vector. Regions in $+x$ encounter regions of the wavefront emitted later in time, a phase advance, while those in $-x$ find an earlier wavefront, a phase delay, for $+\theta$.

$P(x, y, z)$, the weak diffraction (1st-order Born) approximation simply states that the diffraction process at any position \bar{r} inside the physical domain of the hologram produces a superposition of point sources with amplitude and phase described in [34]

$$g(x, y, z) = \varepsilon(x, y, z) \times P(x, y, z) \times a(x, y) \quad (3.3)$$

where $P \equiv A_{probe}$ and $a(x, y)$ is the function describing the hologram aperture at \bar{r} , independent of z . There is no secondary interaction between point sources, or between any part of the probe field and the object function other than at the position \bar{r} . The probe field is therefore assumed to pass through any previous portions of the object unaffected, although in practice a simple depth-dependent absorption term is applied to the probe field. The total response is then due to the superposition of all point sources; essentially the weak diffraction (WD) assumption is the assumption of a linear diffraction process. This assumption functions nicely given a weak grating, however the mutual interaction between diffracted fields in strong gratings becomes significant, and the approximate solution becomes inaccurate. The non-paraxial equation for

the superposition of diffracted point sources is from [35]

$$b(x_0, y_0, z_0) = \iiint g(x, y, z) \exp \left[i \frac{2\pi}{\lambda_p} \|\bar{\mathbf{r}}_0 - \bar{\mathbf{r}}\| \right] dx dy dz. \quad (3.4)$$

Or more generally

$$b(x_0, y_0, z_0) = g(x, y, z) \otimes h(x_0 - x, y_0 - y, z_0 - z), \quad (3.5)$$

where the convolution kernel for the non-paraxial case is [35]

$$h(x_0 - x, y_0 - y, z_0 - z) = \exp \left[i \frac{2\pi}{\lambda_p} \|\bar{\mathbf{r}}_0 - \bar{\mathbf{r}}\| \right], \quad (3.6)$$

and for the paraxial [35]

$$h(x_0 - x, y_0 - y, z_0 - z) = \exp \left[i \frac{2\pi}{\lambda_p} (z_0 - z) \right] \times \exp \left[i\pi \frac{(x_0 - x)^2 + (y_0 - y)^2}{\lambda_p (z_0 - z)} \right]. \quad (3.7)$$

From [34], the value $z_0 = f_2$ is chosen such that singularities are avoided; z_0 no longer lies inside the hologram, but rather adjacent to the pupil side of the collector lens. Then

$$b(x_0, y_0, f_2) = g(x, y, z) \otimes h(x_0 - x, y_0 - y, f_2 - z) \quad (3.8)$$

from Fourier optics, and also in [34], the field precisely at the pupil of the collector lens has a Fourier transform relationship with the field at the image plane. To get the field to the pupil, however, the same transfer function h is convolved with the field adjacent to the lens to propagate the field to the pupil plane, then the Fourier transform is used. From Fourier optics, the field adjacent to the back side of the lens is related to the field on the image plane by

$$q(\xi, \eta) = \exp \left[i\pi \lambda_p f_2 (\xi^2 + \eta^2) \right] \times \mathcal{F}^{(2D)} (b(x_0, y_0, f_2 - z)) \quad (3.9)$$

from [35] where the first term is from the paraxial approximation of the quadratic phase of the lens, which also happens to be the form of the Fourier transform of the Fresnel diffraction

kernel, neglecting a constant phase term. In the exact case, where the Fourier transforming lens is symmetric bi-convex, the phase transformation of the lens is also from [35]

$$\exp [ik_p nd] \exp \left[-ik_p(n-1)2R \left(1 - \sqrt{1 - \left(\frac{\xi \lambda_p f}{R} \right)^2 - \left(\frac{\eta \lambda_p f}{R} \right)^2} \right) \right]. \quad (3.10)$$

If d is small, then $f \propto R$ and the phase transformation has the form of the exact diffraction kernel. Therefore, the field at the image plane is

$$\begin{aligned} q(\xi, \eta) &= H(\xi, \eta, -f_2) \times \int \mathcal{F}^{(2D)}(b(x_0, y_0, f_2 - z)) dz \\ &= H(\xi, \eta, -f_2) \times \int G(\xi, \eta, z) \times H(\xi, \eta, f_2 - z) dz \\ &= \int G(\xi, \eta, z) \times H(\xi, \eta, -z) dz \end{aligned} \quad (3.11)$$

by the convolution property of the Fourier transform, where ξ and η are spatial frequencies near the pupil. The structure of eq. 3.11 is similar to a method discussed in , although here the response is defined for a general transfer function and not specifically the Fresnel transform. The Fourier transform of the transfer function $h \equiv H$ is from [35]

$$H(\xi, \eta, z) = e^{ikz} \exp[-i\pi\lambda z(\xi^2 + \eta^2)] \quad (3.12)$$

for the paraxial case and

$$\begin{aligned} H(\xi, \eta, z) &= \exp \left[ikz \sqrt{1 - (\lambda\xi)^2 - (\lambda\eta)^2} \right] \sqrt{\xi^2 + \eta^2} < \frac{1}{\lambda} \\ &= 0 \text{ otherwise} \end{aligned} \quad (3.13)$$

for non-paraxial; the spatial frequency cut-off excludes evanescent waves from propagating. By Fourier optics, the spatial frequencies at the pupil are related to spatial displacements in the image plane by $\xi = \frac{X}{\lambda f_2}$, $\eta = \frac{Y}{\lambda f_2}$. These equations will prove important in the Matlab[®] simulation of section 3.2, as the integration along \hat{z} can be performed numerically using the FFT algorithm to calculate G . Before proceeding further, let us now examine the response of the VHI system under slightly idealized circumstances. Assume a VHI system with a perfectly recorded

hologram consisting of a single unslanted phase grating, and perfect objective and collector optics. Now, a point source on the object plane is imaged by the VHI system, producing a response on the image plane. This response is defined as follows. Using eq. 2.1 to construct the hologram from two interfering beams

$$I = |A_{ref} + A_{sig}|^2 = |A_{ref}|^2 + |A_{sig}|^2 + 2|A_{ref} \cdot A_{sig}|, \quad (3.14)$$

of which the Bragg-matched term is

$$A_{ref} \times A_{sig}^*. \quad (3.15)$$

Let the two beams be plane waves with $\theta_s = -\theta_r$ and $k_s = k_r = k$ for an unslanted grating. In the paraxial case, the index modulation of the hologram in pupil coordinates will be

$$\begin{aligned} \varepsilon(x, y, z) &= \exp \left[ikz \left(1 - \frac{\theta_r^2}{2} \right) + ikx\theta_r \right] \times \exp \left[ikz \left(\frac{\theta_s^2}{2} - 1 \right) - ikx\theta_s \right] \\ &= \exp \left[ikz \left(1 - \frac{\theta_r^2}{2} \right) + ikx\theta_r \right] \times \exp \left[ikz \left(\frac{\theta_r^2}{2} - 1 \right) + ikx\theta_r \right] \\ &= \exp [i2kx\theta_r]. \end{aligned} \quad (3.16)$$

This is the object function, which is a grating with a vector perpendicular to the optical axis along \hat{x} . Using eq. 3.3, 3.11, and 3.12; and by defining the probe field in the space of the pupil as $P(x, y, z) \times a(x, y)$, the paraxial field at the image plane is given by

$$\begin{aligned} q(X, Y) &= \iiint g(x, y, z) \exp \left[-ik_p \frac{Xx + Yy}{f_2} \right] \exp \left[-ik_p z \left(1 - \frac{X^2 + Y^2}{2f_2^2} \right) \right] dx dy dz \\ &= \int dz \exp \left[-ik_p z \left(1 - \frac{X^2 + Y^2}{2f_2^2} \right) \right] \iint g(x, y, z) \exp \left[-ik_p \frac{Xx + Yy}{f_2} \right] dx dy \\ &= \int \exp \left[-ik_p z \left(1 - \frac{X^2 + Y^2}{2f_2^2} \right) \right] \mathcal{F}^{(2D)} (g(x, y, z)) dz \\ &= \int \exp \left[-ik_p z \left(1 - \frac{X^2 + Y^2}{2f_2^2} \right) \right] G \left(\frac{X}{\lambda_p f_2}, \frac{Y}{\lambda_p f_2}, z \right) dz. \end{aligned} \quad (3.17)$$

If $P(x, y, z)$ is another plane wave in the pupil such that $P(x, y, z) = \exp \left[ik_p z \left(1 - \frac{\theta_p^2}{2} \right) + ixk_p \theta_p \right]$ and $a(x, y) = \text{circ}(x, y)$, then

$$g(x, y, z) = \exp [i2kx\theta_r] \times \exp \left[ik_p z \left(1 - \frac{\theta_p^2}{2} \right) + ixk_p \theta_p \right] \times \text{circ}(x, y) \quad (3.18)$$

$$\begin{aligned} G(\xi, \eta, z) &= \mathcal{F}^{(2D)}(g(x, y, z)) \\ &= \exp \left[ik_p z \left(1 - \frac{\theta_p^2}{2} \right) \right] \times \mathcal{F}^{(2D)}(\exp [ix(2k\theta_r + k_p \theta_p)] \times \text{circ}(x, y)) \end{aligned} \quad (3.19)$$

$$\begin{aligned} &= \exp \left[ik_p z \left(1 - \frac{\theta_p^2}{2} \right) \right] \times \mathcal{F}(\exp [ix(2k\theta_r + k_p \theta_p)]) \\ &\quad \otimes \mathcal{F}^{(2D)}(\text{circ}(x, y)) \end{aligned} \quad (3.20)$$

$$\begin{aligned} \mathcal{F}(\exp [ix(2k\theta_r + k_p \theta_p)]) &= \delta(2k\theta_r + k_p \theta_p + 2\pi\xi) \\ &= \delta \left(2k\theta_r + k_p \theta_p + \frac{k_p X}{f_2} \right) \end{aligned} \quad (3.21)$$

$$\mathcal{F}^{(2D)} \left(\text{circ} \left(\frac{r}{a} \right) \right) = \frac{a^2}{\pi a \rho} J_1(2\pi a \rho) = a^2 \text{jinc}(a \rho) \quad (3.22)$$

where J_1 is the first order Bessel function of the first kind, a is the radius of the circ function by the Fourier transform scaling property, and ρ is the spectral radius. When $\rho = \sqrt{\xi^2 + \eta^2} = \frac{\sqrt{X^2 + Y^2}}{(\lambda_p f_2)}$, then

$$\frac{a^2}{\pi a \rho} J_1(2\pi a \rho) = \frac{a \lambda_p f_2}{\pi \sqrt{X^2 + Y^2}} J_1 \left(\frac{k_p a}{f_2} \sqrt{X^2 + Y^2} \right). \quad (3.23)$$

This Fourier relationship is described in [35], and is also known as a "jinc" function, as it has the appearance of a sinc function with circular symmetry and slightly different null locations. Now, the convolution property of delta functions is used such that the convolution presents itself as applying a spatial shift to the "jinc" which is now centered at the position:

$$R_{\text{Gaussian}} = \left(\lambda_p f_2 \left(-\frac{2\theta_r}{\lambda} - \frac{\theta_p}{\lambda_p} \right), 0 \right) \quad (3.24)$$

with a radius to the first null equal to

$$r_{\text{jinc}} = \frac{0.61 \lambda_p f_2}{a} \quad (3.25)$$

on the image plane. Note that $k = k_p$ and $-\theta_r = \theta_p = \theta_s$ results in Bragg-matched reconstruction, as the reference beam is reconstructed on the image plane including a convolution with the hologram aperture function.

$$G(\xi, \eta, z) = \exp \left[ik_p z \left(1 - \frac{\theta_p^2}{2} \right) \right] \times a \frac{J_1 \left(2\pi a \sqrt{\left(\frac{2\theta_r}{\lambda} + \frac{\theta_p}{\lambda_p} + \xi \right)^2 + \eta^2} \right)}{\pi \sqrt{\left(\frac{2\theta_r}{\lambda} + \frac{\theta_p}{\lambda_p} + \xi \right)^2 + \eta^2}} \quad (3.26)$$

$$= \exp \left[ik_p z \left(1 - \frac{\theta_p^2}{2} \right) \right] \times a^2 \text{jinc} \left(a \sqrt{\left(\frac{2\theta_r}{\lambda} + \frac{\theta_p}{\lambda_p} + \xi \right)^2 + \eta^2} \right) \quad (3.27)$$

$$G \left(\frac{X}{\lambda_p f_2}, \frac{Y}{\lambda_p f_2}, z \right) = \exp \left[ik_p z \left(1 - \frac{\theta_p^2}{2} \right) \right] \times a^2 \text{jinc} \left(a \sqrt{\left(\frac{2\theta_r}{\lambda} + \frac{\theta_p}{\lambda_p} + \frac{X}{\lambda_p f_2} \right)^2 + \left(\frac{Y}{\lambda_p f_2} \right)^2} \right). \quad (3.28)$$

Now the integration along z is performed. The integral is physically bounded by the ends of the hologram as a rect function, which is

$$\text{rect}(x) = \begin{cases} 1 & \text{if } |x| < \frac{1}{2} \\ 0 & \text{otherwise.} \end{cases} \quad (3.29)$$

Integrating

$$\begin{aligned}
& \int_{-\infty}^{\infty} \exp \left[-ik_p z \left(1 - \frac{X^2 + Y^2}{2f_2^2} \right) \right] \exp \left[ik_p z \left(1 - \frac{\theta_p^2}{2} \right) \right] \text{rect} \left(\frac{z}{L} \right) dz \\
&= \int_{-L/2}^{L/2} \exp \left[i \frac{k_p z}{2} \left(\frac{X^2 + Y^2}{f_2^2} - \theta_p^2 \right) \right] dz \\
&= -i \frac{2f_2^2}{k_p (X^2 + Y^2 - \theta_p^2 f_2^2)} \exp \left[iz \frac{k_p}{2f_2^2} (X^2 + Y^2 - \theta_p^2 f_2^2) \right]_{-L/2}^{L/2} \\
&\quad \text{let } B = \frac{k_p}{4f_2^2} (X^2 + Y^2 - \theta_p^2 f_2^2). \text{ Then:} \\
&= -i \frac{1}{2B} (\exp [iBL] - \exp [-iBL]) \\
&= -\frac{1}{B} \sin(BL) = -L \text{sinc} \left(\frac{BL}{\pi} \right) \\
&= -L \text{sinc} \left(\frac{L}{2\lambda_p f_2^2} ((X^2 + Y^2) - \theta_p^2 f_2^2) \right), \tag{3.30}
\end{aligned}$$

where $\text{sinc}(x) \equiv \frac{\sin(\pi x)}{\pi x}$. Eq. 3.30 is an interesting result, as it shows that even with a planar probe beam, an unslanted planar grating will produce a Bragg slit that is actually the shape of a circular arc in the image plane, with radius:

$$|R_{Bragg}| = \theta_p f_2 \tag{3.31}$$

The field and intensity on the image plane is then

$$\begin{aligned}
q(X, Y) &= -L \text{sinc} \left(\frac{L}{2\lambda_p f_2^2} ((X^2 + Y^2) - \theta_p^2 f_2^2) \right) \times \\
&\quad a^2 \text{jinc} \left(a \sqrt{\left(\frac{2\theta_r}{\lambda} + \frac{\theta_p}{\lambda_p} + \frac{X}{\lambda_p f_2} \right)^2 + \left(\frac{Y}{\lambda_p f_2} \right)^2} \right) \tag{3.32}
\end{aligned}$$

$$\begin{aligned}
|q(X, Y)|^2 &= L^2 \text{sinc}^2 \left(\frac{L}{2\lambda_p f_2^2} ((X^2 + Y^2) - \theta_p^2 f_2^2) \right) \times \\
&\quad a^4 \text{jinc}^2 \left(a \sqrt{\left(\frac{2\theta_r}{\lambda} + \frac{\theta_p}{\lambda_p} + \frac{X}{\lambda_p f_2} \right)^2 + \left(\frac{Y}{\lambda_p f_2} \right)^2} \right). \tag{3.33}
\end{aligned}$$

If the hologram is read at a wavelength that is not equal to that of the recording wavelength, it is under a condition known as wavelength de-tuning or wavelength degeneracy. To achieve a

Bragg-matched reconstruction, a change in the probe-reconstruction geometry must occur. In the paraxial case derived previously, both the sinc and jinc functions must be maximized at the same location in the image plane. For $\lambda \neq \lambda_p$ and $Y = 0$, eq. 3.24 gives

$$X = -f_2 \left(\frac{2\theta_r \lambda_p}{\lambda} + \theta_p \right), \quad (3.34)$$

while eq. 3.31 gives the radial location for the center of the Bragg slit. Combining with eq. 3.34 gives

$$\begin{aligned} |R_{Bragg}| = \theta_p f_2 &= -f_2 \left(\frac{2\theta_r \lambda_p}{\lambda} + \theta_p \right), \\ \theta_p &= \frac{-\theta_r \lambda_p}{\lambda}. \end{aligned} \quad (3.35)$$

This result is quite accurate for an unslanted grating and small recording angles. Now, the case of Bragg mis-match is investigated. Let $\varepsilon(x, y, z)$ represent a recording of a plane wave grating in the $x - z$ plane; the more general case of a slanted grating will be considered, where

$$\varepsilon(x, y, z) = \exp [ikz \cos \theta_r + ikx \sin \theta_r] \times \exp [-ikz \cos \theta_s + ikx \sin \theta_s]. \quad (3.36)$$

Let $P(x, y, z)$ be a plane wave in the pupil as before, but here $\bar{\mathbf{k}}_p$ is out of plane with components

$$\bar{\mathbf{k}}_p = \frac{2\pi}{\lambda_p} (\hat{x} \cos \alpha_x, \hat{y} \cos \alpha_y, \hat{z} \cos \alpha_z) \quad (3.37)$$

where

$$\cos \alpha_x \equiv \sin \theta_{px}, \quad \cos \alpha_y \equiv \sin \theta_{py} \quad (3.38)$$

and

$$\cos \alpha_z = \sqrt{1 - \cos^2 \alpha_x - \cos^2 \alpha_y}. \quad (3.39)$$

Instead of $\theta_{px} = \theta_s$, let $\theta_{px} = \theta_s + \theta'_x$ and $\theta_{py} = \theta'_y$, where θ'_x and θ'_y are deviation angles. For small values of θ'_x and θ'_y , the following relationships are used:

$$\sin \theta_{px} = \sin (\theta_s + \theta'_x) \simeq \left(1 - \frac{\theta'^2_x}{2}\right) \sin \theta_s + \theta'_x \cos \theta_s \quad (3.40)$$

$$\cos \theta_{px} = \cos (\theta_s + \theta'_x) \simeq \left(1 - \frac{\theta'^2_x}{2}\right) \cos \theta_s - \theta'_x \sin \theta_s \quad (3.41)$$

$$\sin \theta_{py} \simeq \theta'_y, \quad \cos \theta_{py} \simeq \left(1 - \frac{\theta'^2_y}{2}\right). \quad (3.42)$$

This implies the following from eq. 3.39:

$$\begin{aligned} \cos \alpha_z &\simeq \sqrt{1 - \left(\left(1 - \frac{\theta'^2_x}{2}\right) \sin \theta_s + \theta'_x \cos \theta_s \right)^2 - \theta'^2_y} \\ &\simeq \sqrt{1 - \theta'^2_y - (\sin^2 \theta_s - \theta'^2_x \sin^2 \theta_s + 2\theta'_x \sin \theta_s \cos \theta_s + \theta'^2_x \cos^2 \theta_s)} \\ &= \cos \theta_s \sqrt{1 - \frac{2 \sin \theta_s \cos \theta_s}{\cos^2 \theta_s} \theta'_x + \left(\frac{\sin^2 \theta_s}{\cos^2 \theta_s} - 1 \right) \theta'^2_x - \frac{\theta'^2_y}{\cos^2 \theta_s}} \end{aligned} \quad (3.43)$$

where powers of θ'_x larger than 2 are neglected. This expression has the general form given by

$$f(\epsilon_1, \epsilon_2) = \sqrt{1 + \alpha_1 \epsilon_1 + \beta_1 \epsilon_1^2 + \beta_2 \epsilon_2^2} \quad (3.44)$$

with the second-order Taylor series expansion

$$\simeq f + \frac{\partial f}{\partial \epsilon_1} \epsilon_1 + \frac{\partial f}{\partial \epsilon_2} \epsilon_2 + \frac{\partial^2 f}{\partial \epsilon_1^2} \epsilon_1^2 + \frac{\partial^2 f}{\partial \epsilon_2^2} \epsilon_2^2 + \frac{\partial^2 f}{\partial \epsilon_1 \partial \epsilon_2} \epsilon_1 \epsilon_2. \quad (3.45)$$

At $\epsilon_1 = \epsilon_2 = 0$, the expansion has the form

$$f(\epsilon_1, \epsilon_2) \simeq 1 + \frac{\alpha_1}{2} \epsilon_1 + \frac{4\beta_1 - \alpha_1^2}{8} \epsilon_1^2 + \frac{\beta_2}{2} \epsilon_2 \quad (3.46)$$

giving

$$\alpha_1 = -\frac{2 \sin \theta_s \cos \theta_s}{\cos^2 \theta_s}, \quad \beta_1 = \left(\frac{\sin^2 \theta_s}{\cos^2 \theta_s} - 1 \right), \quad \beta_2 = \frac{-1}{\cos^2 \theta_s} \quad (3.47)$$

$$\cos \alpha_z \simeq \cos \theta_s \left[1 - \frac{\sin \theta_s \cos \theta_s}{\cos^2 \theta_s} \theta'_x - \frac{\theta_x^2}{2} - \frac{\theta_y^2}{2 \cos^2 \theta_s} \right] \quad (3.48)$$

and

$$P(x, y, z) = \exp [i (k_{px} + k_{py} + k_{pz})] \quad (3.49)$$

$$k_{px} = \frac{2\pi}{\lambda_p} \left[\left(1 - \frac{\theta_x^2}{2} \right) \sin \theta_s + \theta'_x \cos \theta_s \right] \quad (3.50)$$

$$k_{py} = \frac{2\pi}{\lambda_p} \theta'_y \quad (3.51)$$

$$k_{pz} \simeq \frac{2\pi}{\lambda_p} \cos \theta_s \left[1 - \frac{\sin \theta_s \cos \theta_s}{\cos^2 \theta_s} \theta'_x - \frac{\theta_x^2}{2} - \frac{\theta_y^2}{2 \cos^2 \theta_s} \right] \quad (3.52)$$

The diffraction response from any plane parallel to the $x - y$ plane in the hologram is given by eq. 3.3. The Gaussian image of a probe point in the image plane is located at

$$R_{Gaussian} = -f_2 \left(\lambda_p \frac{\sin \theta_r - \sin \theta_s}{\lambda} + \left(1 - \frac{\theta_x^2}{2} \right) \sin \theta_s + \theta'_x \cos \theta_s, \theta_y^2 \right) \quad (3.53)$$

from the Fourier transform relationship of eq. 3.21. At the Bragg-matched angular position, the center of the diffracted spot from each plane is represented by a spatial frequency corresponding to $\frac{X}{f_2} = -\sin \theta_r$. The exact diffraction kernel from eq. 3.13 is then approximated by a second-order Taylor series expansion around the point $(X = -f_2 \sin \theta_r, Y = 0)$ as

$$\begin{aligned} \bar{H} &= \sqrt{1 - \left(\frac{X}{f_2} \right)^2 - \left(\frac{Y}{f_2} \right)^2} \simeq \\ &\cos \theta_r + \frac{\tan \theta_r}{f_2} (X + f_2 \sin \theta_r) - \frac{(X + f_2 \sin \theta_r)^2}{2f_2^2 \cos^3 \theta_r} - \frac{Y^2}{2f_2^2 \cos \theta_r} \end{aligned} \quad (3.54)$$

The result of integrating $G \times H$ along \hat{z} as in eq. 3.30 is now represented by

$$B = \frac{|k_p|}{2f_2^2} \left(\bar{H} - \left(\frac{k_{pz}}{|k_p|} + \frac{\varepsilon(z)}{|k|} \right) \right) \quad (3.55)$$

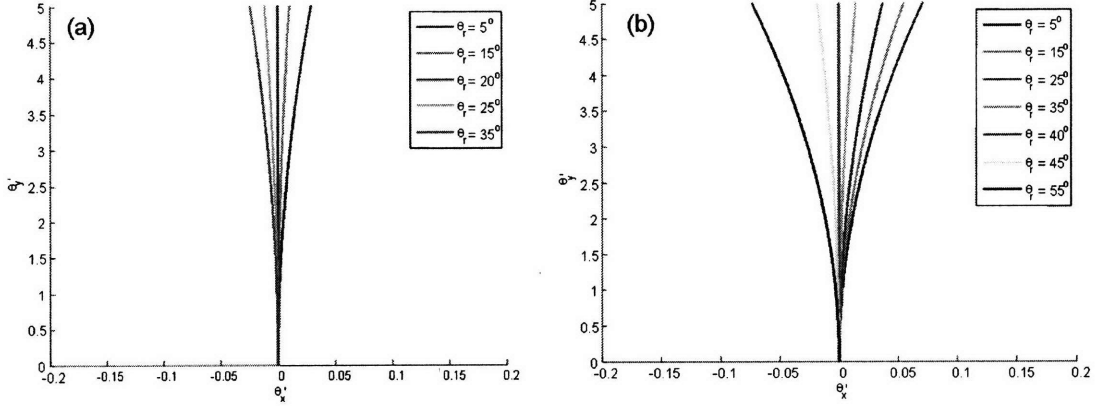


Figure 3-3: Bragg slit curvature for various construction geometries and wavelength-matched reconstruction. (a) $\theta_s = -20^\circ$, (b) $\theta_s = -40^\circ$.

forming the sinc screening function $-L \text{sinc}\left(\frac{BL}{\pi}\right)$

$$= -L \text{sinc} \left(\frac{L}{\lambda_p f_2^2} \left[\begin{aligned} & \cos \theta_r + \frac{\tan \theta_r}{f_2} (X + f_2 \sin \theta_r) - \frac{(X + f_2 \sin \theta_r)^2}{2f_2^2 \cos^3 \theta_r} - \frac{Y^2}{2f_2^2 \cos \theta_r} \\ & - \cos \theta_s \left[1 - \frac{\sin \theta_s \cos \theta_s}{\cos^2 \theta_s} \theta'_x - \frac{\theta'^2_x}{2} - \frac{\theta'^2_y}{2 \cos^2 \theta_s} \right] - \\ & \frac{\lambda_p}{\lambda} (\cos \theta_r - \cos \theta_s) \end{aligned} \right] \right). \quad (3.56)$$

Setting X and Y equal to the gaussian image coordinates, and setting the function inside the sinc in eq. 3.56 to be zero allows the Bragg-matched position of the Gaussian image to be solved as a function of θ'_x and θ'_y . Some of these solutions are presented in Fig. 3-3. This figure shows the Bragg slit curvature changing as the grating slant changes, and that the unslanted case should still be represented by a straight line. Note that the curvature of the slit is increasing as the total inter-beam construction angle increases. This also shows that even when recorded in plane, the VH can have a selective behavior for point sources out of plane that should be Bragg-matched given a certain coordinate in the recording plane. Construction of these recording geometries in the K-sphere model yields a very similar result, although assuming that the image plane has a rotated coordinate system from the hologram indicates that even the unslanted grating will have an apparent selectivity out of plane, matching the experimental Bragg slit curvature in the VH imagery in section 2.6, especially Fig. 2-37(b). Assuming this more complicated yet

more realistic geometry in the weak diffraction model requires the use of a modified Green's function $b(x_0 - x, y_0 - y, z_0 - z)$ in rotated coordinates and is outside the scope of this thesis. Another method for calculating the field at the image plane would be to use integral equation methods to solve for the diffracted field at the collector lens directly. Equation 3.4 provides the non-paraxial solution for the superposition of diffracted point sources where $g(x, y, z)$ is the local diffracted field at each point inside the hologram according to the WD approximation and $\|\bar{\mathbf{r}}_0 - \bar{\mathbf{r}}\|$ is the linear distance in \mathbb{R}^3 from a point source describing an envelope of constant phase on a spherical wavefront according to Huygens principle [35]. This is a non-smooth integral equation of the first kind and can be solved with the appropriate numerical technique. If $z_0 = f_2$, the focal length of the second lens, then $b(x_0, y_0, f_2)$ is the field directly before the collector lens. If the collector is assumed to be paraxial, the field at the image plane can be found from the Fourier relationship from [34]:

$$q(X, Y) = \exp\left[i\pi\frac{X^2 + Y^2}{\lambda_p f_2}\right] \iint b(x_0, y_0, f_2) \exp\left[-i2\pi\frac{Xx_0 + Yy_0}{\lambda_p f_2}\right] dx_0 dy_0 \quad (3.57)$$

This may be a more efficient method for calculating the image field and warrants further study.

3.2 Weak diffraction simulation with Matlab[®], pMatlab, and Zemax[®]

Presented in this section is a computational method for modeling non-paraxial imaging systems with VH pupil elements, i.e. including geometrical aberrations. Recording and reconstruction beams are modeled as depth-dependent phase profiles. The field propagation through the hologram is modeled using a 3-D spatial Fourier transform approach that is accurate within the physical (or scalar wave) optics approximations. This method is subject to the weak diffraction (WD) approximation, also referred to as the 1st order Born approximation. The WD approximation drives a computationally simple model; the thick hologram is represented as a volume of non-interacting phase and amplitude regions whose response is the superposition determined by a 3-D Fourier transformation. This method is applicable in a direct sense to VHs that have very low (<0.05) diffraction efficiency. For stronger holograms, the total efficiency calculation will not be accurate, as higher order diffraction is neglected by this approximation.

The relative efficiency of the first diffracted order remains fairly accurate however, even with strong holograms. For a complete simulation of stronger holograms, more rigorous methods such as coupled-wave theory, beam propagation, or finite-difference time-domain methods must be used. These are beyond the scope of this work. This particular modeling approach allows for a high level of flexibility in simulation.

Simulation of arbitrary geometries

Using WD and the Fourier transform approach, any thick hologram cross-section, including rhomboids, inclined cylinders, conoids, and others may be assumed. The topology and wavelengths of the phase fronts comprising the recording and reconstruction beams may be arbitrarily defined.

Matlab[®] for optical calculations

In order to fully utilize the power of this method, a version of this simulation architecture has been created as a suite of Matlab[®] functions. This suite interfaces with the commercial optical design code Zemax[®] using the Multi-Domain Optimization (MDO) environment, which was developed specifically for optimizing imaging systems [46]. Zemax[®] contains a prolific lens catalog and features a very high-accuracy ray tracing engine. This ensures that almost any conceivable optic can be implemented as the objective in a simulated VH imaging system. The WD model implemented in Matlab[®] is still necessary, however, as Zemax[®] cannot simulate Bragg diffraction, and Matlab[®] is better equipped to handle Fourier transformation in computationally efficient fashion using special properties of VH diffraction that will be highlighted subsequently.

3.2.1 Simulation architecture and design

The hologram model involves a WD technique that discretizes a thick hologram into thin hologram sections and sums the complex amplitudes of their responses upon propagation to the pupil plane. The hologram sections are modeled as a phase function constructed from the sum of amplitudes of the wavefronts comprising the reference and signal beams at a particular depth in relation to the pupil plane. This interference of complex amplitudes is converted

to phase via linear model. This phase object is combined with the probe wavefront incident upon the hologram at the same depth for reconstruction. The weak-diffraction model, while assuming very low diffraction efficiency, is capable of fully simulating aberrated wavefronts, as the simulation is non-paraxial. Consider a VH centered in the pupil plane of a 4- f (two-lens) imaging system. The response function will then provide the diffracted field $q(X, Y)$ at the image plane resulting from the entirety of the field at the pupil plane. The z -coordinate is defined with respect to the pupil plane at $z = 0$. The direction \hat{y} corresponds to the Bragg-degenerate direction in the image reconstruction, and is tangent to the Bragg slit reconstruction at $Y = 0$. The Bragg-selective direction is along \hat{x} . In other words, all beams in the simulation have wave vectors \vec{k} where $\vec{k}_y = 0$. This is certainly not a requirement for this simulation, but merely a convention used in this work to simplify the interpretation of the results. The simulation is capable of fully supporting 2-D multiplexing, etc. On a lower level, the simulation is constructed around three key operations:

- Construction of the hologram phase-amplitude object and probe field near the pupil.
- Propagation of the resulting weak diffraction.
- Numerical integration.

By eq. 3.11, integration for the hologram response only occurs in one dimension, along the optical axis. So, all of the WD calculations are executed explicitly in planes normal to the optical axis and the integration along z is approximated very simply by:

$$\int G(\xi, \eta, z) \times H(\xi, \eta, -z) dz \approx \sum_{n=1}^N G(\xi, \eta, \varrho_n) \times H(\xi, \eta, -\varrho_n) \quad (3.58)$$

$$\varrho_n = \Delta z \left((n-1) - \frac{(N-1)}{2} \right). \quad (3.59)$$

A more sophisticated numerical integration technique might also be used, although Simpson's quadrature has been applied to this problem and produced very similar results. Because the hologram consists of a generally unslanted grating or gratings, it is unlikely that even a large fraction $\frac{\Delta z}{L}$ would cause aliasing in the hologram. Instead Δz must be large enough to avoid aliasing in the product of the diffraction transfer function H and the z -component of the

transformed diffracted field G . As each simulated case is different and this value may not be obtainable analytically, the appropriate value of Δz is found in a heuristic manner. Given a particular phase profile $\phi(x, y, \varrho_n)$, a beam near the pupil is constructed in the non-paraxial case such that

$$A(x, y, \varrho_n) = a'(x, y, \varrho_n) \times \exp \left[i \frac{2\pi n}{\lambda} ((\phi(x, y, \varrho_n) + \varrho_n) \cos(\theta) + x \sin(\theta)) \right], \quad (3.60)$$

where $a'(x, y, \varrho_n) = a(x, y, \varrho_n) \times \exp[-\alpha(\varrho_n + L/2)]$ and n is the bulk refractive index at the wavelength λ . $a'(x, y, \varrho_n)$ is the result of multiplying the binary aperture function $a(x, y, \varrho_n)$ by the loss due to absorption by the hologram material at a certain depth $\varrho_n + L/2$ from Beer's law. This formula is used for all beams near the pupil, whether for construction or re-construction. Note that if $\phi(x, y, \varrho_n) = \text{const}$ then the formula describes a non-paraxial plane wave, as expected. In the simulation, this condition can be enforced to create a perfectly collimated aberration-free beam. The sine and cosine components in the exponential represent the phase delay of the beam on-axis rotated to the global reference frame where \hat{z} is the optical axis. In the construction of the hologram object, the two-field interference formula from eq. 2.1 is used to find the intensity pattern produced by the reference and signal beams at a particular depth plane. This intensity pattern is then used in the formula

$$\varepsilon(x, y, \varrho_n) = \exp \left[-i \frac{2\pi n}{\lambda} I(x, y, \varrho_n) \Delta z \Delta n \right], \quad (3.61)$$

where Δn is the peak-to-peak value of change in refractive index in the photosensitive material. The intensity pattern produced by the interfering beams is the component $I(x, y, \varrho_n)$. It should be clear that eq. 3.61 produces a phase-only object, which is the type of hologram used in the experiments of chapter 2; however an amplitude grating could be simulated by using the direct relationship $\varepsilon(x, y, \varrho_n) = 1 - I(x, y, \varrho_n)$. This is somewhat of an idealization, as the response of the photosensitive polymer is assumed to be linear with intensity, which may or may not be valid. The flexibility of the WD method makes it possible to model over or underexposure in a specific material given the relevant recording parameters and knowledge of the material response. In that case, $I(x, y, \varrho_n) \Delta n$ would be replaced with a function $\Delta n = f(x, y, \varrho_n, \rho)$ where ρ is a vector of recording parameters. The shape of the hologram, under even fairly

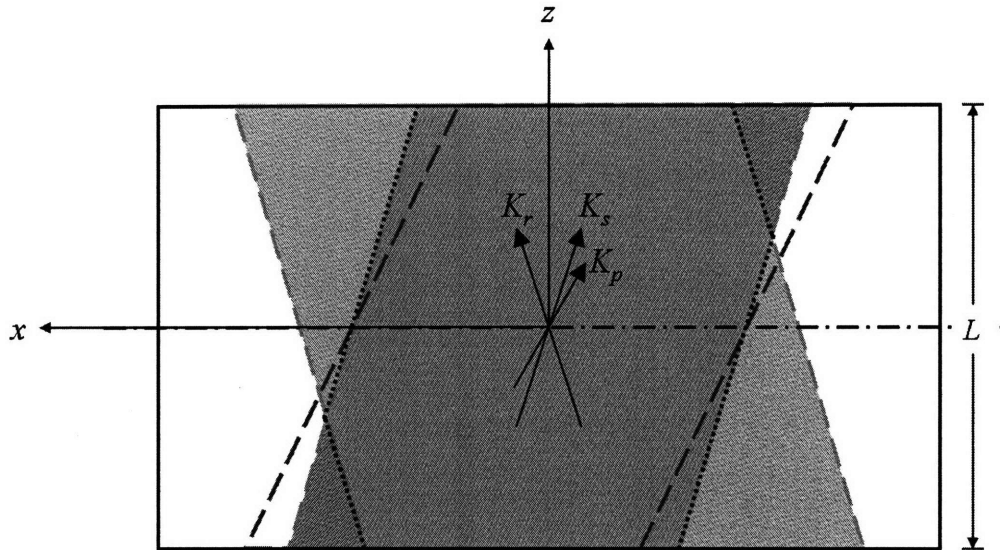


Figure 3-4: Geometry produced by two overlapping space-limited beams. The grating area produced is outlined with a black dashed line. A wavelength-degenerate probe beam, outlined in dashed red, probes the hologram at the Bragg-matched angle. Only the area inside both the black and dashed red lines contributes to reconstructing the original reference beam.

idealized conditions, can be quite complicated. If the reference beam near the pupil is a plane wave with a very large diameter in comparison with the signal beam, the hologram takes the shape of a cylinder aligned with the signal beam. However as shown in figure 3-4, limiting the size of both recording beams produces more complicated geometry. Furthermore, a wavelength-degenerate probe beam Bragg-matched to the hologram with a substantial angular shift will intercept less of the grating area than a wavelength-matched beam. Any defocus or other aberrations present in the probe beam will cause different depths in the hologram to be probed with changing phase curvatures as the probe sweeps across the hologram. The effect of this phenomenon, especially on a non-planar grating can be non-trivial and is explored further in section 3.3. It should also be noted that this simulation assumes that the wavefront curvature is small and the hologram is thin enough such that the outer edge of the beam envelope follows the wave vector K and does not expand or contract as it travels through the hologram. Although the simulation architecture is perfectly capable of modeling this behavior, such a level of complexity

was omitted from the analysis of section 3.3.

3.2.2 MDO, MZDDE, and Zemax[®]

Multi-Domain Optimization (MDO) is a software package based on the Dynamic Data Exchange Toolbox for Matlab[®] (MZDDE)*. This powerful set of functions allows Matlab[®] to modify lens and configuration data in the various editors in Zemax[®]. MZDDE provides a rapid and efficient means to build optical systems with Zemax[®] and to test multiple configurations via Matlab[®] scripting. It also allows Matlab[®] to call analysis functions within Zemax[®], and to read configuration data and simulation or optimization results. MDO is a suite of analysis and optimization tools for Matlab[®] that utilize MZDDE functions extensively. This greatly facilitates the use of MZDDE by enabling a programmer to easily perform analyses or optimizations outside of Zemax[®]. MDO was developed under the DARPA/MONTAGE program as a tool for designing a novel ultra-thin camera system [46]. More relevant to the work presented here, MZDDE allows Matlab[®] to include Zemax[®] models of wavefronts within optical systems. This is the method by which the wavefront function $\phi(x, y, \rho_n)$ is obtained in the simulation. Each arm of the hologram recording setup is simulated as a separate Zemax[®] lens file. Parameters which are to be varied in multiplexed gratings; incidence angle for the reference arm or defocus for the signal arm, are programmed into the configuration editor as different configurations of the lens file. In principle, any parameter that Zemax[®] is able to modify can be altered in a new configuration producing a new solution that will be interpreted by the VHI simulation, but the two aforementioned parameters are the relevant ones for VHI. The design of the probe optics may be likewise specified in a third lens file, although frequently the optics will be the same as those used in the signal arm of the construction to take advantage of the wavefront conjugating property of VHs. Whichever lens file is used for the probe beam, there are specific parameters that must be set, most importantly, the wavelength used in the reconstruction should be specified as the second wavelength in the lens file. Also, any lateral displacement of the point source in the object plane can be specified as displacements of the field point (along \hat{y}); any number of these may be specified, the desired probe field point is selected when the wavefront function is called through MZDDE. Each lens file must have a slab

*MZDDE is copyright 2002-2004, Defencetek, CSIR.

of pq-PMMA at the conjugate plane to the system aperture in the case of a relay, or the system aperture itself. This ensures that the chief ray passes through the center of the slab of Pq-PMMA, and that the marginal ray will pass through the same point on the Pq-PMMA surface regardless of field position in object space, and represents the correct location of the VH in the real system. The slab should also contain a paraxial lens surface that is correctly focussed, since the beam incident on the Pq-PMMA slab is essentially afocal and must be made to come to a focus for Zemax[®] to calculate the wavefront map. Before performing a calculation of image plane intensity, Zemax[®] is accessed through the data server, the important system parameters are read from the lens file, and a data file (or files) are generated containing the wavefront map calculated by Zemax[®]. This wavefront is calculated directly from the ray-tracing model by the method of superposition of Gaussians [47]. The VHI simulation accounts for different sizes of construction or probe beams, so the lens files should all be set to use object space NA as the aperture type to properly simulate the overlap of beams inside the hologram. While Zemax[®] is capable of providing a wavefront at various depths in the Pq-PMMA material, in practice the slab is so thin that Zemax[®] finds essentially no difference between wavefront maps retrieved from either end of the slab. As a consequence, only one wavefront map is calculated by Zemax[®] for each beam; a phase shift places the wavefront at the appropriate depth in the material.

3.2.3 Distributed block 2-D FFT and spatial-spectral sampling

Acknowledgement 2 *The author would like to thank Jose Dominguez-Caballero in the Mechanical Engineering department at MIT for his assistance in this section.*

One of the serious challenges in simulating a structure such as a VH is the required scale; the VH itself is macroscopic yet contains detail with periods potentially as small as $\frac{1}{2}$ of the recording wavelength. The amount of memory needed to store the phase object of the hologram to double precision (64 bit) quickly becomes unacceptably large. For example, assume a computational domain of 4mm \times 4mm sampled at 0.15 μ m. This is very close to the parameters described in section 3.3. In this case, to solve for the locally diffracted field is to dot-multiply two matrices, each containing $\sim 7.11 \times 10^8$ entries. At 128 bits per entry, this results in a memory requirement of ~ 11.4 gigabytes to store each matrix. The ideal radix-2 FFT algorithm operates

in $2N \log_2 N$ time. To solve the propagation of the diffracted field to the pupil plane, there would need to be 4.25×10^{10} operations, not a challenging figure at present. It is therefore the memory requirement of the calculation that is prohibitive. This problem is solved by using a modified form of the overlap-add method for large FT filtering calculations by breaking the space domain into smaller elements that can be easily processed [49]. The overlap-add method involves defining elements, zero-padding if required, then finding the FT for each element, applying a filter, and finally calculating the superposition of the inverse-FT for each element. The filter in this system is the non-paraxial diffraction kernel H , which has a finite length. The method employed here is modified; only a *forward* FT is required; the solution to the image plane field is in the frequency domain of the pupil plane, so superposition must also take place in the frequency domain. As a result, a phase shift is applied to the solution to each element that is representative of the position of the element in pupil coordinates. Fig. 3-5 illustrates the steps in the the discretization and zero-padding process. First, the required size of the space domain is found, which is the size of the largest extent of any grating in the hologram at all depths. Therefore, the size of the space domain in terms of the number of data points is $M_x = 2^{\frac{\max(r(x,y),x)}{\Delta x}}$ and $M_y = 2^{\frac{\max(r(x,y),y)}{\Delta x}}$ for a symmetric grating. This domain is then separated into $b_x \times b_y$ adjacent elements for further processing. The location of the center of the element in the space domain is (ψ_x, ψ_y) , and will be applied as a phase shift to the spectrum from a particular element in the superposition of spectra in the frequency domain. In this simulation, the user may specify the size of the zero-padded domain M'_x and M'_y , the minimum ratios $\frac{M'_x}{N_x}$ and $\frac{M'_y}{N_y}$, and finally the size of the spatial discretization in the pupil, Δx . The simulation then solves for the required number of elements and the number of original data points N_x and N_y included within each element. The relationship between the space and frequency domain drives the requirements for the particular values chosen. The discretization of the spatial frequencies ξ and η is dependent on the maximum domain dimensions $x_{\max} = M'_x \Delta x$ and $y_{\max} = M'_y \Delta x$:

$$\Delta\xi = \frac{1}{M'_x \Delta x} \quad \Delta\eta = \frac{1}{M'_y \Delta x} \quad (3.62)$$

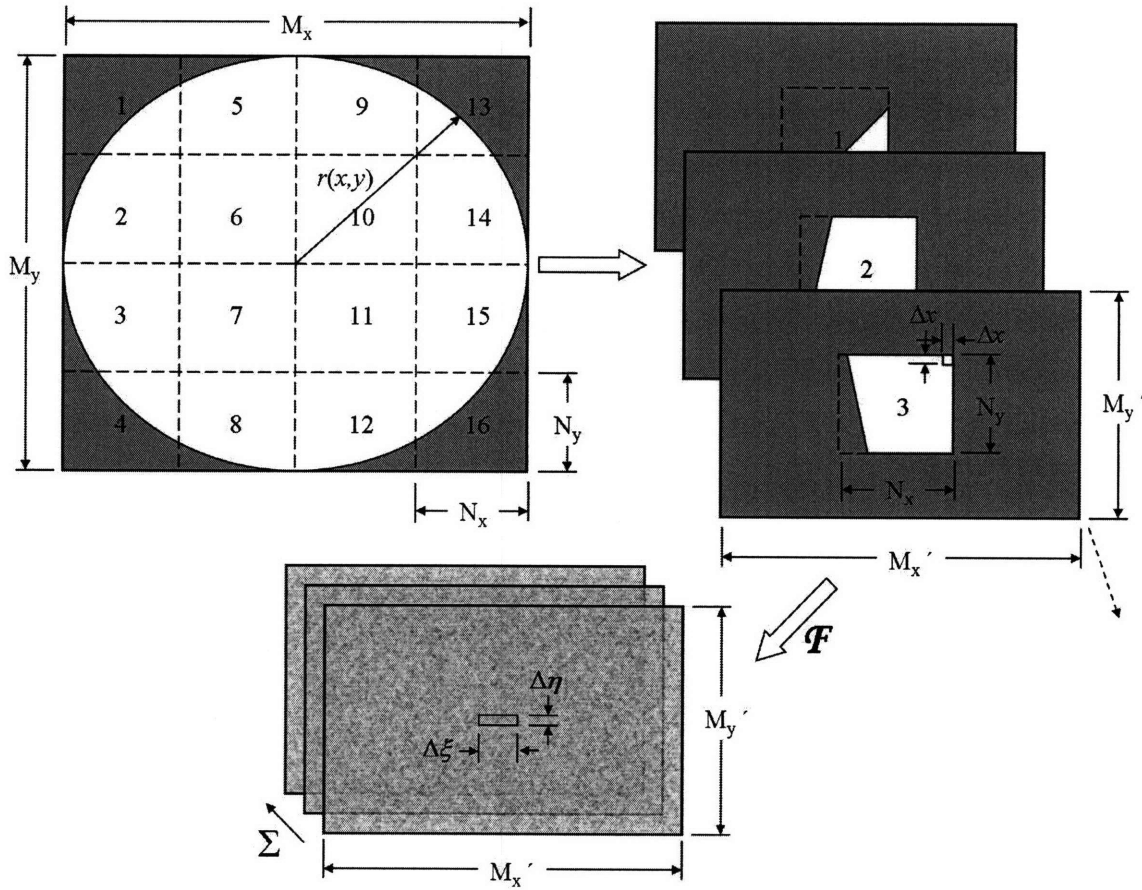


Figure 3-5: Schematic of the block-FFT algorithm used in the simulation. (1) The largest extent of the hologram grating region defines the lateral size of the space domain, which is separated into equal-sized elements. (2) The hologram sections in each element are equally zero-padded. (3) The Fourier transform of each element is then summed coherently with the appropriate phase shifts applied. The dimensions of the 2-D frequency domain are equal to the zero-padded element.

Because the frequency domain contains both positive and negative frequencies, the maximum absolute frequency that can be represented is therefore $\frac{1}{2}M'_x\Delta\xi$ and $\frac{1}{2}M'_y\Delta\eta$. From eq. 3.62:

$$\frac{1}{2}M'_x\Delta\xi = |\xi_{\max}| = \frac{1}{2\Delta x} \quad \frac{1}{2}M'_y\Delta\eta = |\eta_{\max}| = \frac{1}{2\Delta x} \quad (3.63)$$

These are the spectral limits of the elements, and ultimately represent the spatial limits of the solution $q(X, Y)$ as well. Let $X = \xi\lambda_p f_2$ and $Y = \eta\lambda_p f_2$:

$$|X_{\max}| = \frac{\lambda_p f_2}{2\Delta x} \quad |Y_{\max}| = \frac{\lambda_p f_2}{2\Delta x} \quad (3.64)$$

$$\Delta X = \frac{\lambda_p f_2}{M'_x \Delta x} \quad \Delta Y = \frac{\lambda_p f_2}{M'_y \Delta x} \quad (3.65)$$

It should be made clear at this point that the spectral extent and discretization of the solution $q(X, Y)$ is the same as that of each element after zero-padding. We now begin by defining the minimum feature size in pupil coordinates using some assumptions about the hologram recording conditions. The grating period Λ can be calculated from the incidence angles and the recording wavelength using the formula $\Lambda = \frac{\lambda}{\sin\theta_r - \sin\theta_s}$ [35]. In this section, all quantities assume values inside the hologram bulk material. Let $\lambda = 327.5\text{nm}$, $\theta_r = -\theta_s = 22.04^\circ$, so $\Lambda = 0.436\mu\text{m}$. To satisfy the Nyquist sampling theorem, the sampling period must be $\Lambda_{\text{sample}} = \Delta x < \frac{\Lambda}{2} = 218\mu\text{m}$. Spectra for a grating constructed with these parameters and various sampling periods is shown in Fig. 3-6. In the simulation study of section 3.3, the sampling period was chosen to be $\Delta x = 0.1487\mu\text{m}$; this value satisfies the Nyquist sampling requirement and was somewhat arbitrarily chosen such that larger recording angles could be simulated without aliasing. Higher spatial frequencies could potentially exist in multiplexed holograms and also as local changes in grating period due to non-planar recording wavefronts from defocus or other aberrations. In the non-paraxial case (equation 3.13), frequencies $\sqrt{\xi^2 + \eta^2} \geq \frac{1}{\lambda_p}$ are not propagated by the transfer function $H(\xi, \eta, \varrho_n)$ and are considered evanescent. This might suggest that Δx should be limited to $|\xi_{\max}| = \frac{1}{\lambda_p} = \frac{1}{2\Delta x}$, but this is not the case. While the transfer function will not propagate evanescent frequencies, the transfer function acts on $G(\xi, \eta, \varrho_n)$, not the object function $\varepsilon(x, y, \varrho_n)$ by itself. In order for $G(\xi, \eta, \varrho_n)$ to be accurate, both $\varepsilon(x, y, \varrho_n)$ and the probe beam $P(x, y, \varrho_n)$ must not be aliased, hence the requirement of minimum spatial sampling based on the grating period. The spectrum of the

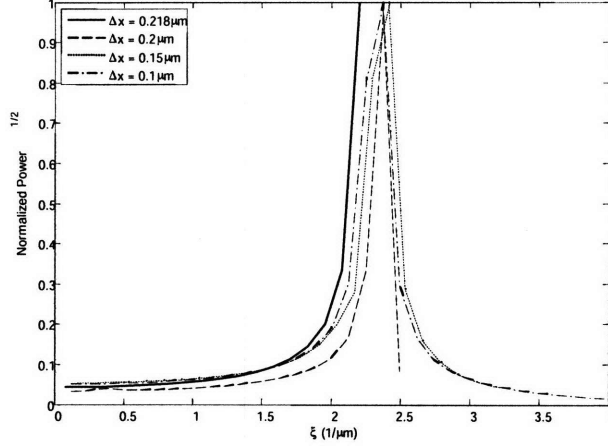


Figure 3-6: Spectra of the phase object constructed given the recording parameters defined in the text. The various curves shown here represent different sampling in the space domain, with the largest sampling representing the Nyquist limit. The vertical axis is normalized power, and the DC term has been removed for clarity.

resulting weak diffraction $G(\xi, \eta, \varrho_n)$ is then subject to the evanescent cutoff. The largest spatial frequency of the perfectly Bragg-matched reconstruction is approximately $\frac{\sin(\theta_d)}{\lambda_p}$, so the evanescent cutoff only becomes important to the result if the diffraction angle θ_d is larger than $\frac{\pi}{2}$ radians. There is one other important consideration however. Note the behavior of the non-paraxial transfer function in figure 3-7b; the phase oscillates so rapidly close to the evanescent cutoff that the transfer function itself becomes aliased. The local frequency in the non-paraxial transfer function can be described by:

$$\omega_{local}(\xi) = \frac{1}{2\pi} \frac{d\phi}{d\xi} \quad (3.66)$$

$$= \frac{1}{2\pi} \frac{d}{d\xi} \left(kz \sqrt{1 - (\lambda_p \xi)^2 - (\lambda_p \eta)^2} \right)$$

$$\omega_{local}(\xi, z; \eta = 0) = -z \lambda_p \frac{\xi}{\sqrt{1 - \lambda_p^2 \xi^2}} \quad (3.67)$$

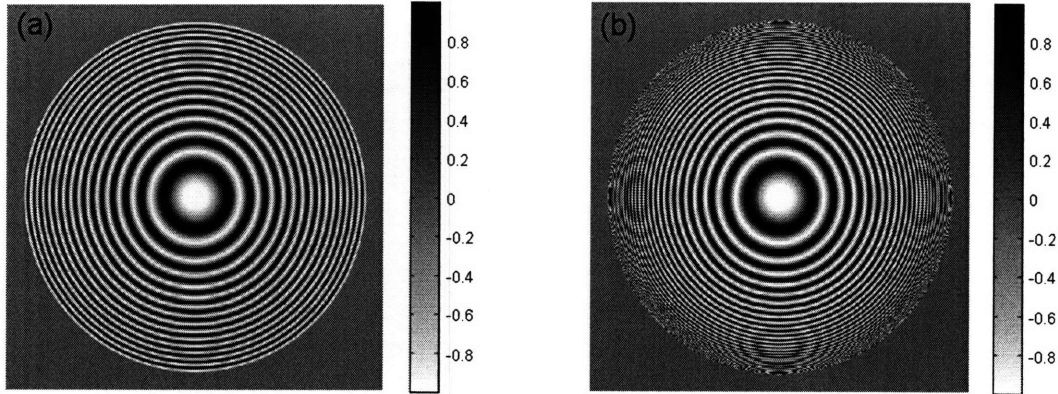


Figure 3-7: Real part $\Re(H)$ of the (a) paraxial and (b) non-paraxial transfer function for a small region of the pupil $80\mu\text{m}\times 80\mu\text{m}$ across using parameters from the text and $z = -10\mu\text{m}$.

The criterion for the maximum allowable spatial frequency step size based on this formula would then be:

$$\frac{1}{2\Delta\xi} > \omega_{local} \left(\frac{\sin(\theta_d)}{\lambda_p}, \frac{L}{2}; \eta = 0 \right) \quad (3.68)$$

$$D_\xi \Delta x > 2 \times \omega_{local} \left(\frac{\sin(\theta_d)}{\lambda_p}, \frac{L}{2}; \eta = 0 \right) \quad (3.69)$$

For $L = 2\text{mm}$, $\lambda = 327.5\text{nm}$, $\theta_d = 22.04^\circ$, and defining D_ξ as the number of discrete points in the filter H , eq. 3.69 indicates the necessary spatial extent $D_\xi \Delta x > 809.7\mu\text{m}$; with $\Delta x = 0.1487\mu\text{m}$, $D_\xi > 5445$ to avoid aliasing in the transfer function. This basically defines the requirements for the total size of the element in the overlap-add method [49]; the filter, H , will contain at least D_ξ elements along $\hat{\xi}$. The length of the filter defines the number of zero entries added to the data in each element in the overlap-add method, so $M'_x \geq N_x + D_\xi$. Because the spatial frequencies of g along $\hat{\eta}$ are very small in comparison, the required zero-padding D_η is likewise small compared to D_ξ . There is an additional requirement for the total size of the zero-padded element. If well-resolved details of the lateral PSF of the hologram are required for an accurate analysis, the closed-form equations defined previously can provide a scale for the spatial extent of certain key features in the image plane. Suppose for example that the Bragg slit should be resolved well enough that the sidelobes are well-resolved, defined here as four pixels between

nulls. From eq. 3.33, the width of the sidelobes on the image plane is:

$$\frac{\pi L}{2\lambda_p f_2^2} (f_2^2 \theta_p^2 - X_1^2) - \pi = \frac{\pi L}{2\lambda_p f_2^2} (f_2^2 \theta_p^2 - X_2^2) - 2\pi \quad (3.70)$$

$$\Delta X_{\text{sidelobe}} = X_2 - X_1 \quad (3.71)$$

With parameters $L = 1.61\text{mm}$, $\lambda_p = 327.5\text{nm}$, $f_2 = 3.6\text{mm}$, and $\theta_s = 22.04^\circ$, the width of the sidelobe of the Bragg slit is $\Delta X_{\text{sidelobe}} = 1.90\mu\text{m}$. Since $\Delta X = \frac{\lambda_p f_2}{M'_x \Delta x}$, the required product $M'_x \Delta x$ is:

$$M'_x \Delta x = \frac{4\lambda_p f_2}{\Delta X_{\text{sidelobe}}} \quad (3.72)$$

Yielding a spatial extent of $M'_x \Delta x > 2482\mu\text{m}$ and assuming $\Delta x = 0.1487\mu\text{m}$, $M'_x > 16694$ points for a well-resolved Bragg slit sidelobe on the image plane. In the study of section 3.3, this is the requirement that drives the choice of the final element dimensions. Because most of the detail in the image plane is dependent upon the X -coordinate, the required size of the element along \hat{y} is not well defined and is subject to the specific requirements of the simulation. This begs the important question, why zero pad the data in each element at all? First, the size of the physical extent of the hologram in the pupil may not be large enough to realize some of the sampling requirements defined previously, so additional data points are required to increase the resolution in the frequency (image) domain, as in eq. 3.72. Second, the memory and processor time required to compute the 2-D FFT with Matlab[®] is actually lower for matrices containing a smaller fraction of non-zero entries [48], so memory requirements are eased if the zero-padding is increased, although the number of elements will naturally increase as a result. Third, zero-padding is necessary because of the action of the diffraction kernel H on the field g , the limit was defined in eq. 3.69. Diffraction will cause energy from the original field to be distributed everywhere in space, but for short propagation distances, most of the energy in the original field remains close to the limits imposed by the aperture function. If the field at the pupil plane were reconstructed by inverse-FT, this would appear as a "halo"; without zero-padding, the convolution of g with h becomes circular, the halo becomes aliased, and wraps around the edges of the element, and the reconstruction of the original domain by superposition of elements will be inaccurate. In this simulation however the field at the pupil plane is not reconstructed, only the field at the image plane is simulated and because of the Fourier relationship between the

two planes, the simulation implicitly requires a perfect collector lens. The simulation cannot operate in an afocal mode for very large holograms. If resources exist to reconstruct the field at the pupil plane, then afocal solutions are possible. In the case of very large holograms however, the field at the image plane is the superposition of the spectra of individual elements, each with a shifted phase representing the spatial location of the element in pupil coordinates. This phase shift is given by:

$$\Delta\varphi^m = \exp[-i2\pi(\xi\psi_x^m + \eta\psi_y^m)] \quad (3.73)$$

Where (ψ_x^m, ψ_y^m) is the coordinate near the pupil of the center of element m . The complete formula for the processing of the elements used in the simulation of section 3.3 is given by:

$$q(X, Y) \approx \sum_{m=1}^{b_x \times b_y} \Delta\varphi^m \sum_{n=1}^N G^m \left(\frac{X}{\lambda_p f_2}, \frac{Y}{\lambda_p f_2}, \varrho_n \right) \times H \left(\frac{X}{\lambda_p f_2}, \frac{Y}{\lambda_p f_2}, -\varrho_n \right) \quad (3.74)$$

3.2.4 Parallel processing with pMatlab and LLGrid

Equation 3.74 describes the superposition of phase-shifted element spectra. On inspection, this equation is easily parallelizable, either summation could take place independently. As such, the simulation has been implemented on the LLGrid computer at MIT Lincoln Laboratory in Lexington, Massachusetts. This grid computer contains approximately 230 Red Hat Linux nodes that are capable of running parallel computations via either the C/C++ MPI library or pMatlab, a programming shell for Matlab[®] incorporating elements of the Matlab[®] MPI toolbox for inter-node communication. The advantage of pMatlab is a reduction in coding time and complexity (lines of code) to implement parallel solutions in Matlab[®] versus the MPI toolbox, as the construction of parallel data structures is simplified to the level of constructing standard Matlab[®] structures, and in other cases native Matlab[®] functions are overloaded to provide a truly seamless boundary between serial and parallel programming [50]. Parallelizing the algorithm of eq. 3.74 with pMatlab is done by distributing to separate processor nodes the summation along \hat{z} of separate elements of the hologram. This is the most natural choice as several small data files, each representing the wavefront phase delays inside a single element, can be produced before the parallel processing step and distributed independently to each node, reducing the amount of data transfer in the implementation. Parallel programming introduces

the concept of processor rank, where the leader process has rank $r = 0$. Eq. 3.74 can then be re-written as:

$$q^r(X, Y) = \Delta\varphi^{r+1} \sum_{n=1}^N G^{r+1} \left(\frac{X}{\lambda_p f_2}, \frac{Y}{\lambda_p f_2}, \varrho_n \right) \times H \left(\frac{X}{\lambda_p f_2}, \frac{Y}{\lambda_p f_2}, -\varrho_n \right) \quad (3.75)$$

For all ranks. If $r = 0$, a final step is added:

$$q(X, Y) \approx \sum_{r=0}^{(b_x \times b_y) - 1} q^r(X, Y) \quad (3.76)$$

To calculate the value of the function $q(X, Y)$. By doing so, the computation time has been decreased by a factor of $\frac{1}{b_x \times b_y}$ from the amount required by eq. 3.74. The pMatlab simulation is detailed in the flowchart Fig. 3-8.

3.3 Simulation Study

Acknowledgement 3 *The author would like to thank Yuan Luo at the University of Arizona-Electrical and Computer Engineering department for providing the rigorous coupled-wave simulation results shown in this section.*

In order to validate the weak diffraction VHI simulation, the angular selectivity and depth selectivity experiments from sections 2.3 and 2.4 were reproduced to the best fidelity possible given the limits of the simulation. The power of the method lies in its independence from paraxial limits, so a study was also undertaken to understand the capabilities of the simulation in applications involving wave aberrations. This study takes the same form as the experiment from section 2.5. Two gratings were simulated, S9 and F3B from table 1-2, repeated here.

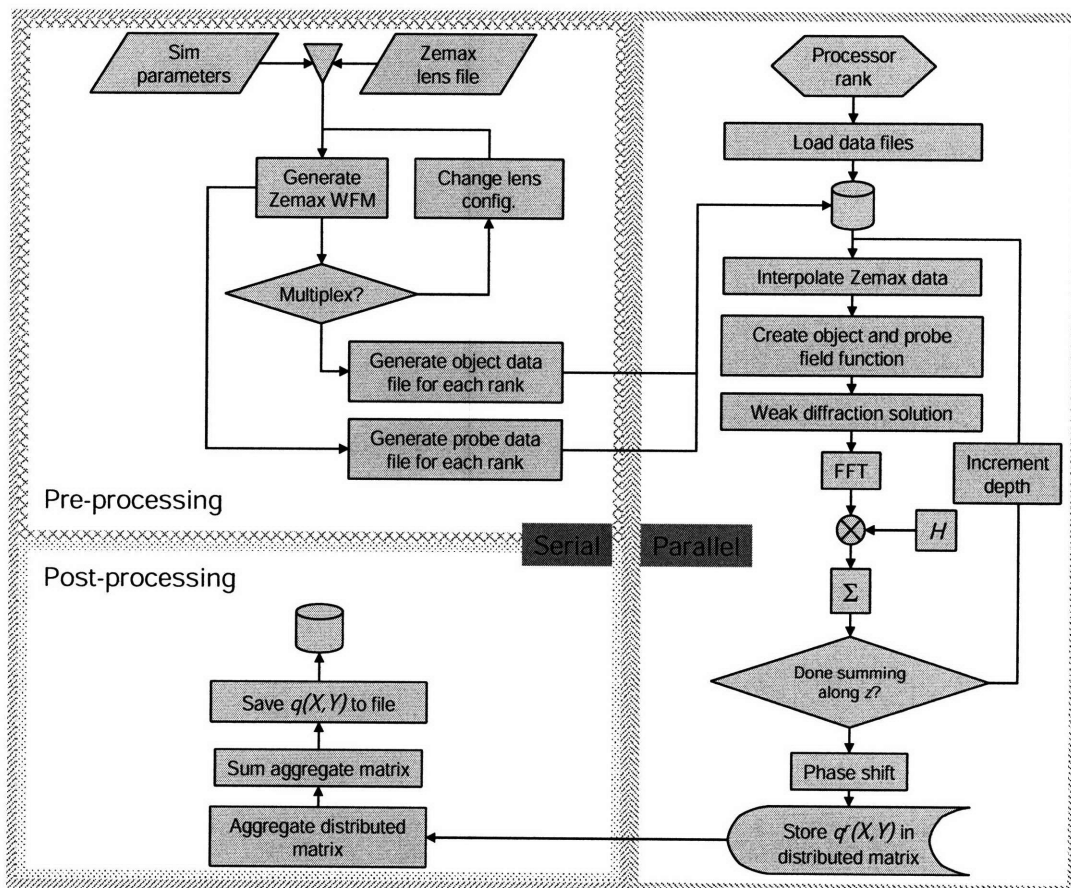


Figure 3-8: Flowchart of the parallel simulation using pMatlab. Processing begins with the specification of simulation parameters and a ZEMAX[®] lens file in the pre-processing stage. Once the wavefront data has been saved, the parallel processing can begin, which ends with another serial step – the leader process aggregates and sums the distributed matrix of individual element solutions and saves the result.

Name	S9	F3B
Gratings	1	2
Exposure Wavelength	488nm	488nm
Thickness	1.61mm	1.54mm
Nominal Recording Angle	$\pm 34^\circ$	$\pm 34^\circ$
Δz Per Grating	0	0, $+50\mu\text{m}$
$\Delta\theta$ Per Grating	0	0, 2.5°

Table 3-1: Holographic filters simulated in this section.

These particular holograms were chosen because they are representative of two cases: A single grating hologram useful for validating some of the properties of VHs, and a two-grating multiplexed hologram intended to be used in two-layer 3-D multispectral imaging. While the five-grating hologram F17 would have been even more interesting to simulate, there was not sufficient experimental data to validate the results. When possible, a Rigorous Coupled-Wave (RCW) solution[†] is plotted with the weak diffraction result and the experimental data. In this section, there are two simulation methods that are applied to most problems. The first is a slightly idealized situation involving a hologram with cylindrical cross-section and on-axis beam centers. The second is a more realistic scenario involving hologram geometry similar to that shown in Fig. 3-4, and off-axis beam centers; that is, the edges of the phase profiles in the recording beams generally form the grating near the surface of the hologram on both sides. The simulated recording geometry used by both VH filters is shown in Fig. 3-22. Zemax[®]-generated phase profiles for the incident beams are shown in Fig. 3-10. These profiles were split into smaller data sets based upon the distribution of block-FFT elements in the pupil. Because the beam spot size is known from Zemax[®], the wavefront data can be trimmed to remove, for example, rows of zeros in the phase profile representing the beam edge, and then properly interpolated as the physical extent of each block element in the pupil is calculated in pre-processing. The interpolation of the phase profile is performed with a simple linear method, as this preserves the shape of the profile near the edge of the beam, and has reduced memory

[†]RCW analysis performed by Yuan Luo of the Electrical and Computer Engineering department at the University of Arizona.

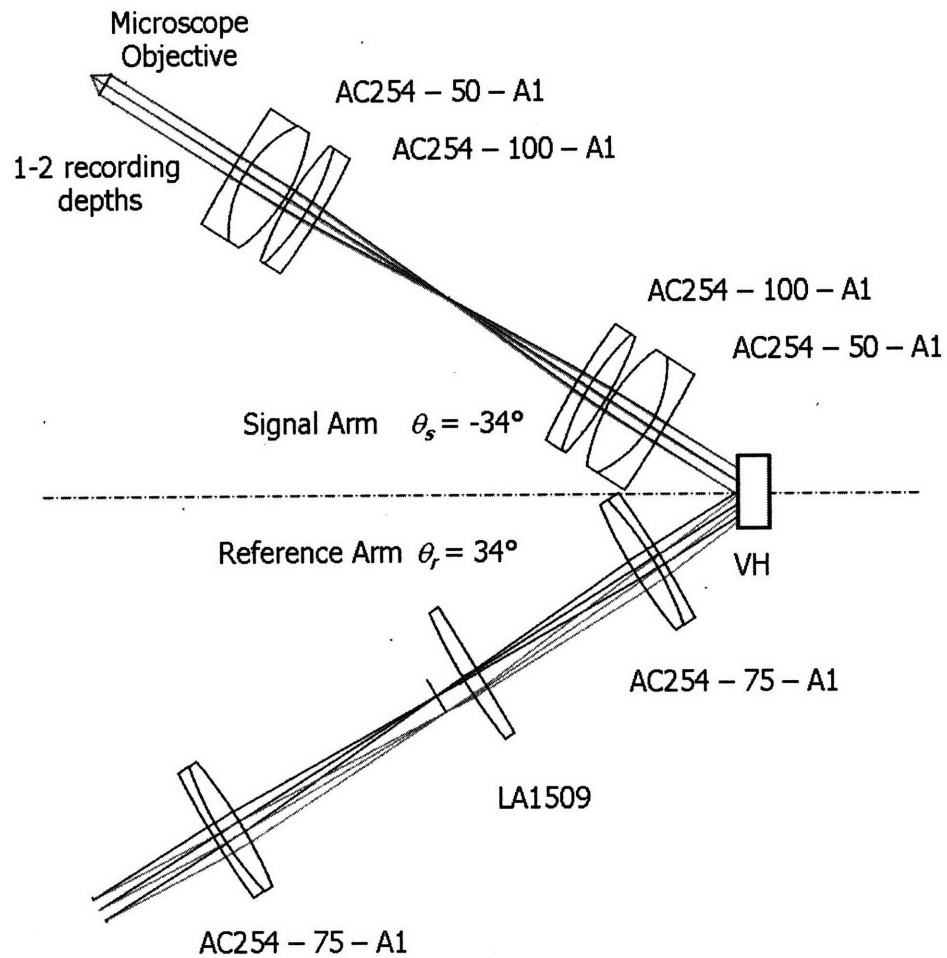


Figure 3-9: Geometry of the recording optics used in the simulation study. Both the reference and signal arms were simulated with Zemax[®]. The second grating in hologram F3 was recorded with the larger reference angle, shown in green, and a point source $50\mu\text{m}$ closer to the objective lens than the focal position. All gratings were recorded with $\lambda = 488\text{nm}$.

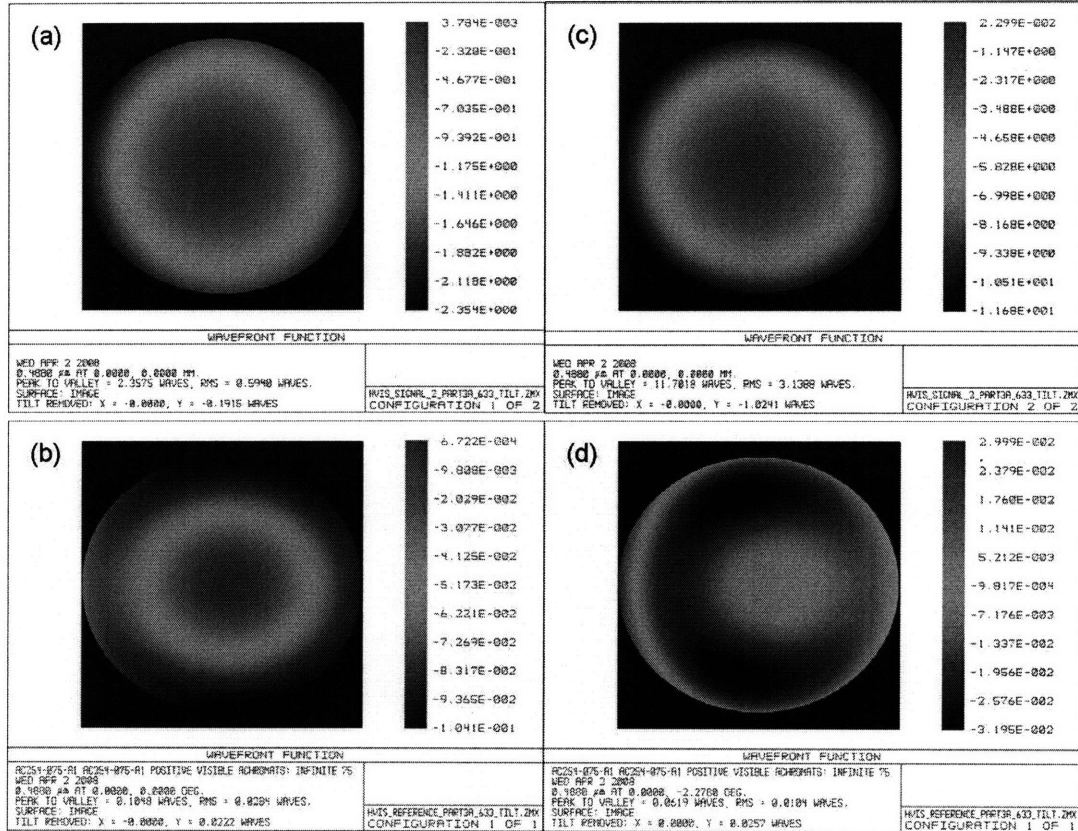


Figure 3-10: Wavefronts generated by Zemax[®] and used to record the VH. (a) and (b) in focus signal and reference wavefronts used for S9 and F3 grating 1, (c) and (d) signal and reference wavefronts used for F3 grating 2.

and computational requirement versus other methods, such as cubic spline interpolation. Once these wavefronts are used to construct the hologram, Zemax[®] provides another phase profile from the lens file simulating the objective optics. In this study, generally the same lens file is used for the objective optics as for the signal arm of the construction, however a 633nm wavelength is often used. The simulated phase profile used for the probe beam is shown in Fig. 3-11 with $\lambda_p = 633\text{nm}$.

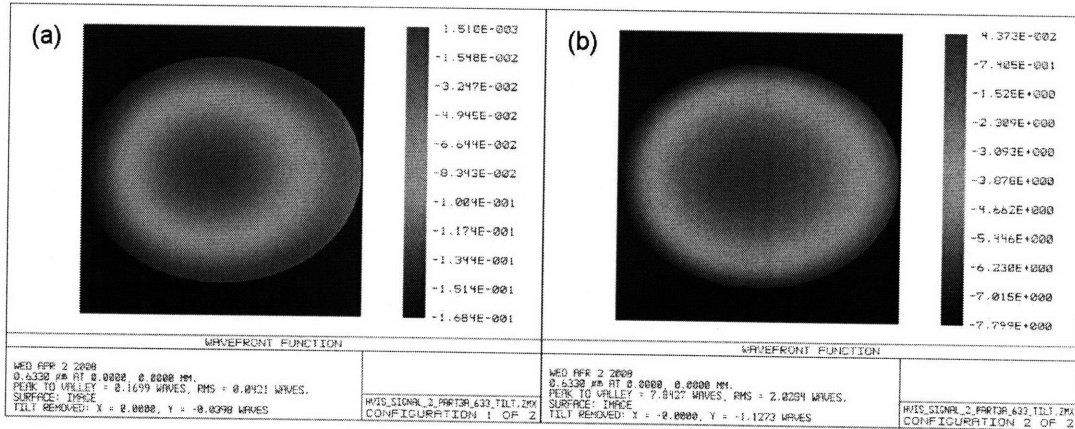


Figure 3-11: Probe beam wavefronts simulated by Zemax[®] for $\lambda_p = 633\text{nm}$ (a) in focus and (b) defocused by $+50\mu\text{m}$.

3.3.1 Angular selectivity and diffraction efficiency

This section introduces a simulation study that performs analysis similar to the experiments of section 2.3. One of the difficulties in performing this type of analysis with the weak diffraction simulation is that the diffraction efficiency can only be estimated, so a well-defined point of reference, such as an efficiency solution from the Kogelnik formula (eq. 2.14) or RCW analysis, may be necessary to scale the results. Estimating the diffraction efficiency in the weak approximation is, however, fairly simple because of the underlying assumptions of the method. Comparing the integrated *intensity* of the first order with the zeroth-order undiffracted beam reveals a gross over-estimation of the un-diffracted power. This is due to the weak diffraction assumption constructing the un-diffracted beam as the superposition of the un-diffracted amplitudes from many very weak gratings. A scaling in the form:

$$\bar{q}^0(X, Y) = \frac{q^0(X, Y)}{N} \quad (3.77)$$

can be applied to the function with finite support representing the un-diffracted field on the image plane $q^0(X, Y)$ where N is the number of discrete gratings in the summation along the

optical axis \hat{z} . The efficiency of the hologram can then be estimated as:

$$\eta \approx \frac{\sum_{b=0}^{M'_y-1} \sum_{a=0}^{M'_x-1} |\bar{q}_{a,b}^{+1}|^2}{\sum_{b=0}^{M'_y-1} \sum_{a=0}^{M'_x-1} |\bar{q}_{a,b}^0|^2} \quad (3.78)$$

Where $q^{+1}(X, Y)$ is the function with finite support representing the field of the first diffracted order on the image plane. The boundaries for these functions are made arbitrarily but due to the extraordinarily low background power level in the image plane, the resulting efficiency estimate is not sensitive to very large bounds. In this study, as in the experiment, the hologram is probed along the conjugate direction, that is, along the reference arm to reconstruct the signal beam. This separates the response from each grating in a multiplex hologram, and removes the necessity to add defocus to certain gratings to obtain an accurate result. As in the experiment, the hologram is illuminated by a collimated beam directly, without objective optics, so Zemax[®] is only involved in the construction step.

M'_x	22000	Δz	80.5 μm (S9), 77 μm (F3)
M'_y	2400	Δz_s	0, +50 μm (F3)
Block ratio	4 (x); 1.25 (y)	α	$4 \times 10^{-5} / \mu\text{m}$
Elements	6×10	n ($\lambda = 488\text{nm}$)	1.49761
Δx	0.1487 μm	n ($\lambda = 633\text{nm}$)	1.48997
$\Delta \theta$	2.54° (F3)	Δn	7×10^{-5}

Table 3-2: General parameters for the angular selectivity simulation.

The angular selectivity results are shown in Figs. 3-12 through 3-14. For each plot, Curve α is a grating constructed with perfect plane waves, β uses Zemax[®]-simulated wavefronts, and γ simulates the hologram with Zemax[®] wavefronts, beam tilting, and offsets for an accurate hologram cross-section. The black diamond in each plot represents the solution for diffraction efficiency from the Kogelnik equation. When available, the RCW result for the grating is shown as a thick dotted line. For hologram F3, the "idealized" case was not simulated, and the RCW solution is only given for the planar grating (#1). Although the weak diffraction approximation can only estimate the diffraction efficiency, Fig. 3-13 shows a fairly good agreement with the

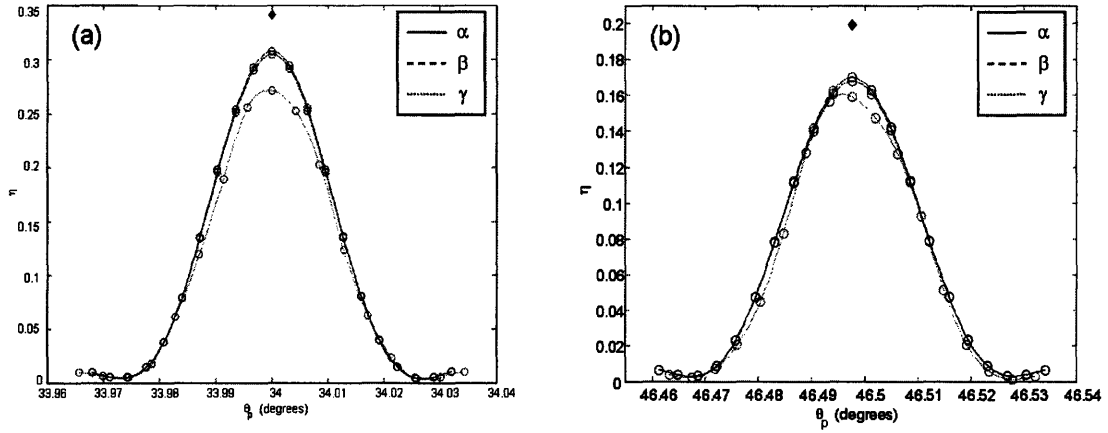


Figure 3-12: Simulated angular selectivity versus diffraction efficiency of hologram S9 at (a) $\lambda_p = 488\text{nm}$ and (b) $\lambda_p = 633\text{nm}$.

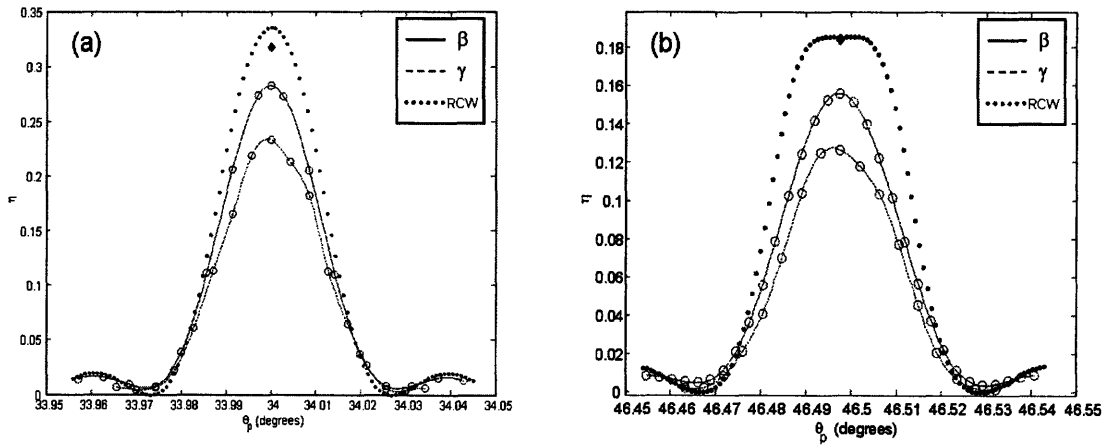


Figure 3-13: Simulated angular selectivity versus diffraction efficiency of hologram F3, grating #1 (planar) at (a) $\lambda_p = 488\text{nm}$ and (b) $\lambda_p = 633\text{nm}$.

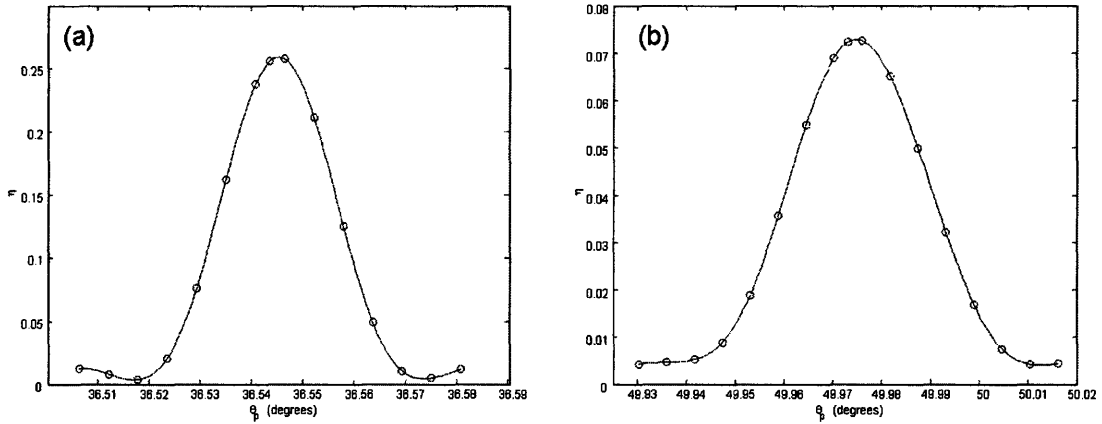


Figure 3-14: Simulated angular selectivity versus diffraction efficiency of hologram F3, grating #2 (spherical) at (a) $\lambda_p = 488\text{nm}$ and (b) $\lambda_p = 633\text{nm}$. Only the cylindrical hologram was simulated.

RCW solution, within about 20% for the peak value. According to the analysis in [37], the ratio between the bulk refractive index of PMMA and the estimated value of the index modulation used here should provide strong agreement between the WD, Kogelnik, and RCW solutions. Also, the idealized WD model was only used for hologram S9, recorded with plane waves. While a more idealized solution could have been applied to hologram F3 by simply using closed-form spherical wavefronts to represent defocus, this would not capture effects such as the spherical aberration induced by the hologram surface in such a case, while Zemax[®] does include such effects in the phase profile. For the spherical grating in hologram F3, the angular selectivity was only simulated with a cylindrical hologram. Because of the Fourier relationship between the pupil plane and the image plane, the WD simulation does not function in an afocal mode. The only method available to "move" the image plane is to add defocus to the probe beam; in the conjugate probe case, defocus is added to the probe beam with an opposite sign of that used to record the hologram. In the offset case, this produces astigmatism in the reconstruction, and the angular response of the hologram is substantially changed. This does not occur in the mode where the probe beam is roughly aligned with the signal recording arm, so this alternative geometry could have been used to analyze the angular selectivity of the hologram. Interestingly, in the experiment when the reconstruction beam from any spherical grating was

allowed to propagate a few meters, it began showing astigmatism, which has not been explained theoretically. Figure 3-16 shows an image of the intensity on the image plane in this case, the astigmatism is evident in the characteristic horizontal diffracted spot in Fig. 3-16a. More on this in section 3.3.2. It is possible that the interference between defocused beams that shift laterally with respect to each other produces this effect. Figures 3-15 and 3-16 also show the

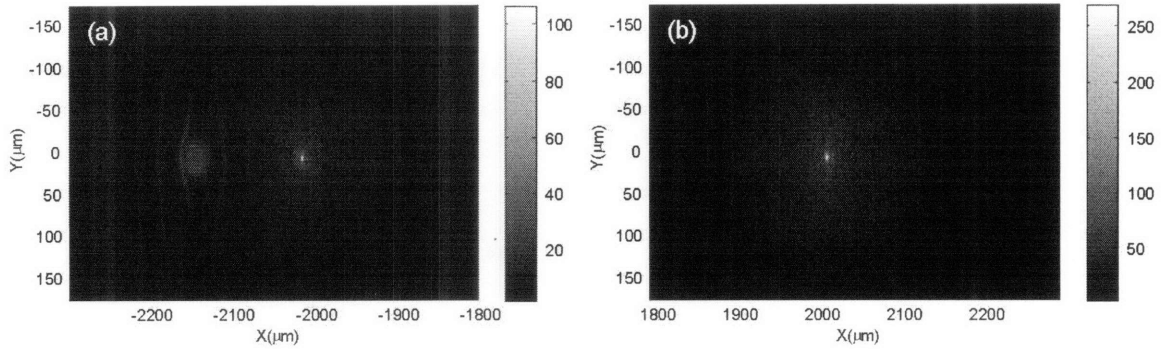


Figure 3-15: Image plane intensity for the conjugate angular selectivity simulation, grating F3#1 (planar) at $\lambda_p = 488\text{nm}$, scaled as $|q(X, Y)|^{1/4}$. (a) is the region surrounding the diffracted beam, (b) shows the undiffracted beam.

relative change in the angle of the reconstruction beams as the two different gratings are probed. Some crosstalk is evident as the dim circle near the bright reconstruction point; the grating that is not being probed also produces a reconstruction, although heavily attenuated. The repeated vertical stripes are evidence of under-sampling with the depth discretization Δz ; only the stripe over the strong reconstruction is the Bragg slit predicted in the closed-form solution. While the simulation involving beam offsets better simulates the geometry of the hologram, it does assume a hard boundary on both the hologram and the probe beam which does not occur in the real case because of diffraction present in the beams upon reaching the hologram. This sharp boundary causes an asymmetry in the simulated peak efficiency values, as the real hologram has a more gradual loss of efficiency. The comparison between the cylindrical simulation and the experimental measurements of section 2.3 is shown in Fig. 3-17 through 3-19. Generally, the shape of the response is quite similar to the experiment; with appropriate scaling aided by the Kogelnik result, the result should be even more accurate. Interestingly, the response of

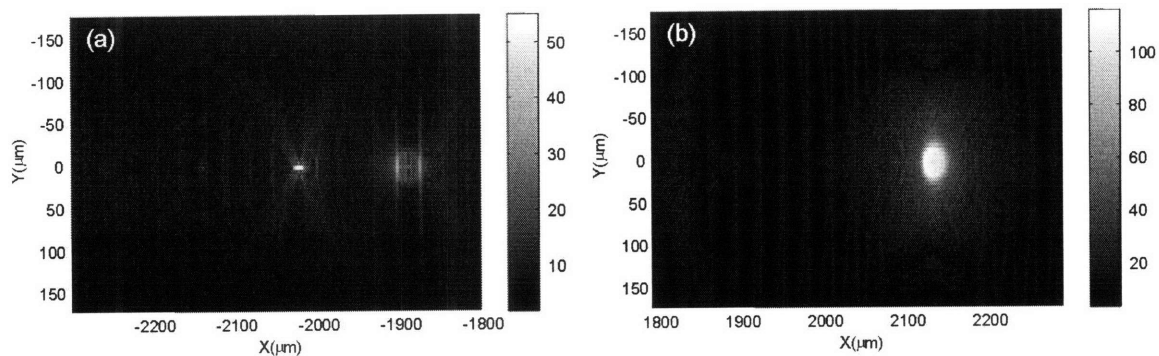


Figure 3-16: Image plane intensity for the conjugate angular selectivity simulation, grating F3#2 (spherical) at $\lambda_p = 488\text{nm}$, scaled as $|q(X, Y)|^{1/4}$. (a) is the region surrounding the diffracted beam, (b) shows the undiffracted beam.

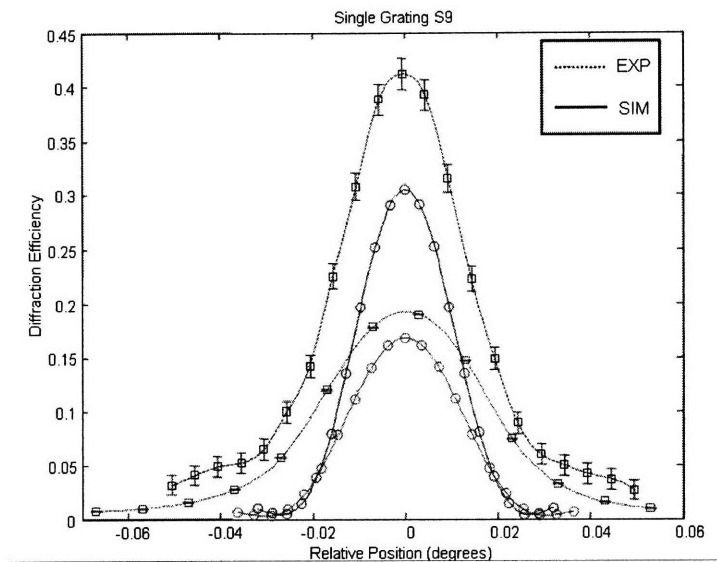


Figure 3-17: Comparison between experiment and simulation for diffraction efficiency versus angle for hologram S9. Reconstruction at $\lambda_p = 488\text{nm}$ is shown in blue; $\lambda_p = 633\text{nm}$ is shown in red.

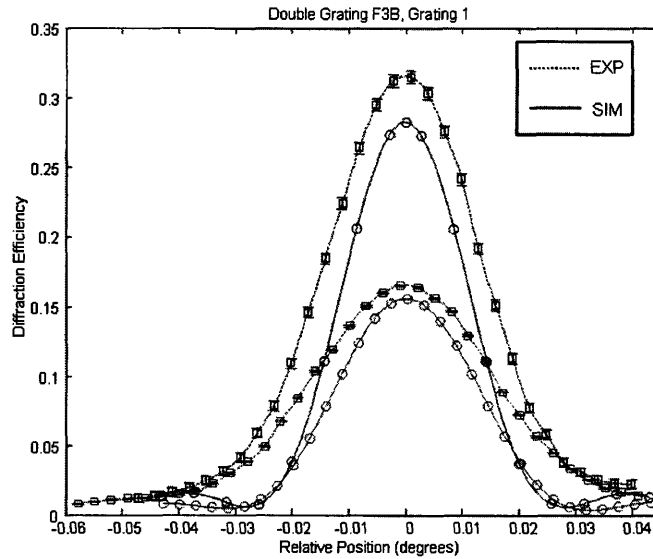


Figure 3-18: Comparison between experiment and simulation for diffraction efficiency versus angle for grating F3#1 (planar). Reconstruction at $\lambda_p = 488\text{nm}$ is shown in blue; $\lambda_p = 633\text{nm}$ is shown in red.

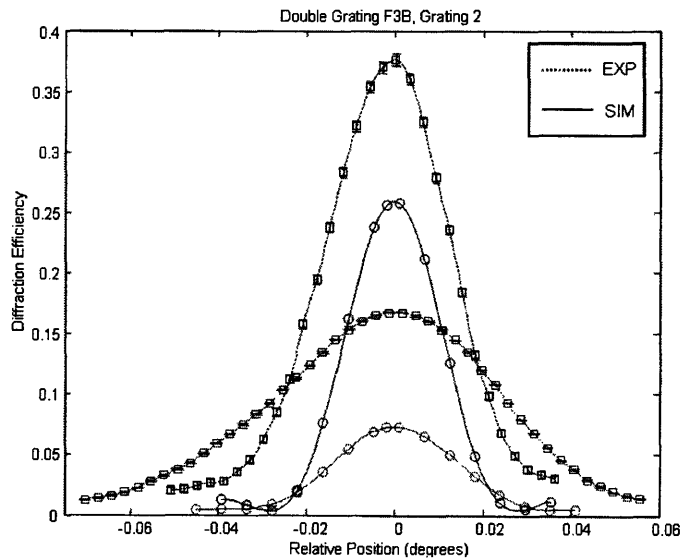


Figure 3-19: Comparison between experiment and simulation for diffraction efficiency versus angle for grating F3#2 (spherical). Reconstruction at $\lambda_p = 488\text{nm}$ is shown in blue; $\lambda_p = 633\text{nm}$ is shown in red.

the spherical grating is much stronger than the prediction, which estimates that the response should be approximately 50% of the response from the planar grating at 633nm. In fact, the experimental data shows the reconstruction at this wavelength is actually *stronger* than the planar reconstruction. This is possibly due to changes in the recording parameters.

3.3.2 Aberrated beams and depth selectivity

Initial studies with 1 and 2-D models

Before proceeding with modeling very large holograms as used in imaging, it was important to qualitatively evaluate the simulation to ensure that it was capable of performing the analysis required of the full simulation, namely simulating the effects of aberration on the probe wavefront and the resulting change in hologram depth selectivity. This was done initially without Zemax[®], as the primary ray (Seidel) aberrations have wavefront topologies that are represented by simple closed-form expressions. Due to the smaller physical extent of the holograms, the simulations were carried out on a single personal computer and did not require the large grid computer described in the following section. The response of a volume hologram to the five primary aberrations was simulated in an idealized hologram consisting of a single grating of perfect plane waves, and only containing the Bragg-matched diffraction term. The paraxial propagation kernel was used in this case. The hologram has a radius $a = 600\lambda$, a thickness of $L = 2000\lambda$, an on-axis signal arm and a reference beam angle of 14.04° . The hologram is probed by a point source through an aberrated objective lens with $NA = 0.15$. The simulated response of the VHI system is shown in Fig. 3-20. In the case of field-dependent aberrations, the point source was placed at the extreme edge of the field. Excluding the Bragg slit, these results are very similar to the diffraction patterns produced by conventional imaging systems with aberrations [31]. Given this encouraging result, a new simulation was constructed that was able to interface with Zemax[®] and simulate a more representative objective lens. Additionally, larger holograms were simulated, but this was through the restriction of the simulation to the xz plane only, producing 1-D results. This restriction, while reducing computation time and enabling larger hologram radii, requires that only radially symmetric phase profiles can be simulated. Fortunately, spherical aberration is radially symmetric. An example is shown in Fig. 3-21, where the diffraction efficiency versus defocus is shown for a paraxial lens and a Newport

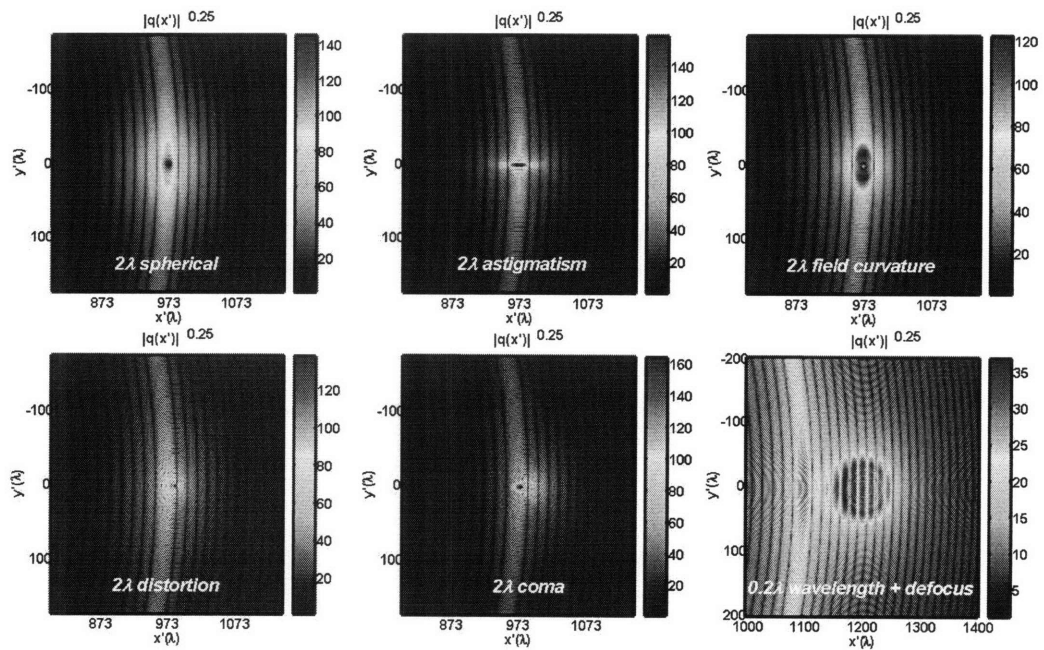


Figure 3-20: Six images representing the response of a volume hologram to 2λ of the five primary aberrations in a lens with $NA = 0.15$. Each case appears to show the expected diffraction pattern of a conventional imaging system screened by a sinc function. Of these aberrations, only spherical, defocus, and wavelength detuning are shift-invariant.

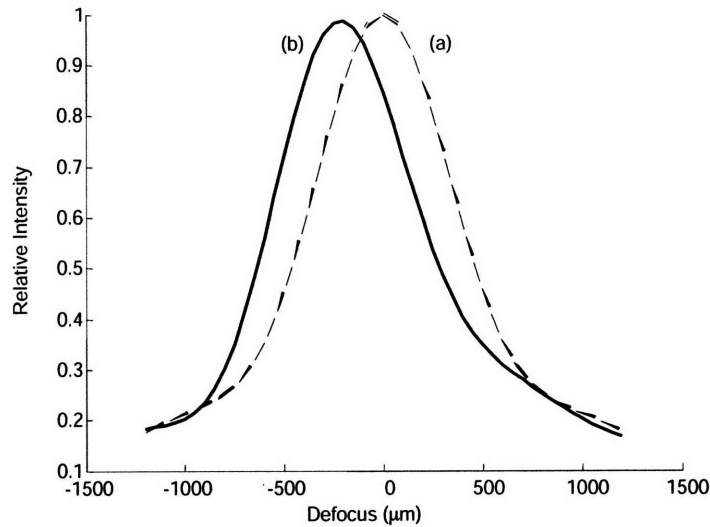


Figure 3-21: Integrated intensity versus depth given (a) paraxial and (b) non-ideal objective optics. The lens used to generate curve (b) is a Newport KBX052 bi-convex lens; $f = 49.948\text{mm}$.

plano-convex lens simulated by Zemax[®]. The hologram parameters are $L = 2\text{mm}$, $a = 2.1\text{mm}$, $\theta_r = 23^\circ$, $\theta_s = 0^\circ$, and $\lambda_p = \lambda = 532\text{nm}$, and perfect planar reference and signal beams. Note that the defocus response for the Newport objective is not symmetric with defocus as in the paraxial case. Additionally, the peak response has shifted to a position away from the nominal focal position. This tilted z-PSF profile is representative of the response seen in the aberrated z-PSF measurements of section 2.5. The 1-D simulation was also used to investigate the effect of the shape factor of the objective lens on the depth selectivity of the VHI system. The objective lens shape factor is defined by $q = \frac{R_1 + R_2}{R_1 - R_2}$, where R_1 and R_2 are the radii of curvature for the lens front and back surfaces, respectively. Given the same hologram and objective NA that produced Fig. 3-21, the performance of the hologram versus lens shape factor is shown in Fig. 3-22. Interestingly, with the correct shape factor the FWHM of the z-PSF can drop below the level of the paraxial case, although the diffraction efficiency of the grating is always lower with a real lens. Based on this result, a similar study was undertaken to further understand the effect of objective lens shape factor on the system response for a different hologram geometry and system NA. This time, using parameters $L = 1.5\text{mm}$, $a = 3\text{mm}$, $\theta_r = 20^\circ$, $\theta_s = -20^\circ$, and $\lambda_p = \lambda = 532\text{nm}$ for an unslanted grating, and using Zemax[®] to simulate the wavefront

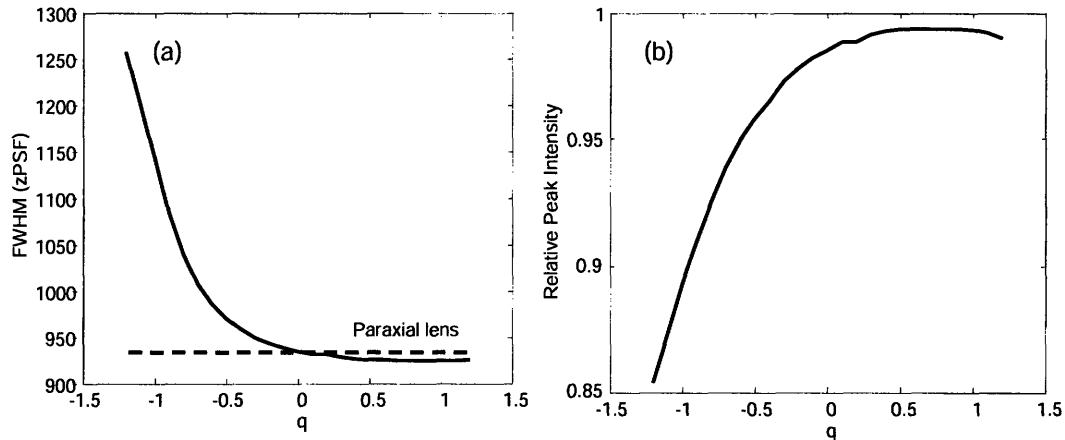


Figure 3-22: (a) Width of the FWHM of the zPSF versus shape factor of the objective lens. (b) Peak intensity of the integrated reconstruction versus lens shape factor, scaled relative to the reconstruction with a paraxial objective lens.

inside a volume of Pq-PMMA, the results were somewhat different, as shown in Fig. 3-23. The the FWHM of the z-PSF has decreased due to the larger total recording beam angle and hologram aperture, even though the thickness of the hologram was reduced by 25%. In each case, a q of ~ 0.75 produces the best imaging performance, although with these parameters, the paraxial case has better performance in all figures of merit. A pictorial result of the image plane intensity in the vicinity of the first diffracted order is shown in Fig. 3-24. The effect of moving the point source along the optical axis produces a variation of the classic "blinking spot" diffraction response of a circular aperture screened by a sinc function [52]. Note also that as the point source moves along \hat{x} , the center of the Bragg slit shifts as well, and in the opposite direction of the image of the point source as predicted in eq. 3.33. These results show that the weak diffraction simulation is capable of modeling the response of a VHI system with aberrated objective optics, however the simulation requires a different approach for simulation of a full 2-D image plane field produced by larger holograms.

Studies with 2-D block-FFT models

The block-FFT method was used to simulate hologram depth selectivity as it was used for angular selectivity. All of the block-FFT simulations were performed on LLGrid at MIT Lincoln

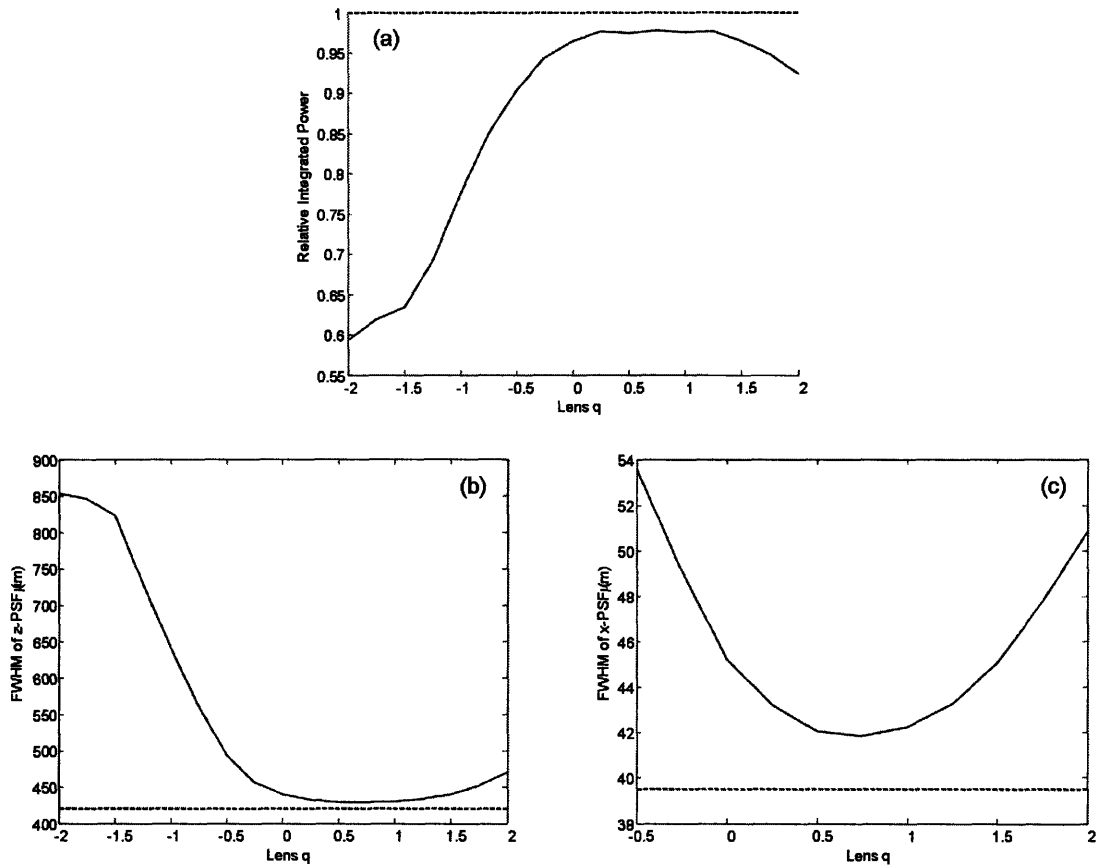


Figure 3-23: Simulated response of an unslanted planar grating to a probe point source and a non-paraxial lens with shape factor q . The response of the grating to a perfect paraxial lens is shown by the dotted line. (a) integrated intensity versus q . (b) depth selectivity as the FWHM of the z-PSF versus q . (c) angular selectivity as the FWHM of the x-PSF versus q .

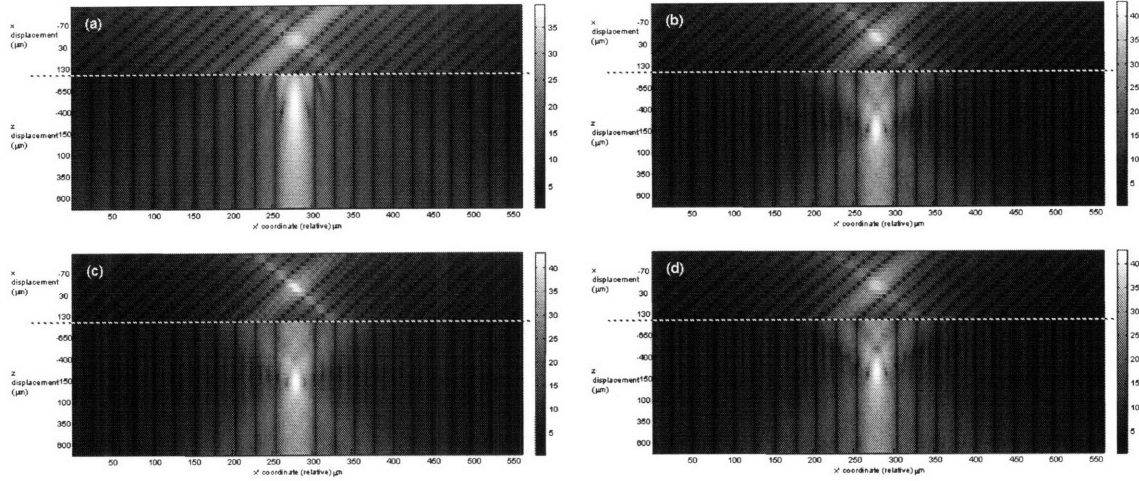


Figure 3-24: Each image presented here is a simulated 1-D section of the image plane field amplitude to the power of 1/4 along the X -axis for a given point source position in object space. The top of each image represents point source displacement along \hat{x} , while the bottom shows displacement along \hat{z} . (a) $q = -2.0$; (b) $q = 0$; (c) $q = +0.75$; (d) $q = +2.0$.

Laboratory. This method was necessary due to the large spatial extent of the hologram aperture and the sampling requirements to avoid aliasing. The study consists of two parts: Evaluating the performance of the WD simulation versus the RCW simulation and experimental data in depth selectivity, and recreating with the WD simulation the conditions of the experiments in section 2.5 involving controlled aberrations in the objective. In simulation, the peak diffraction response along \hat{z} with constant x is generally used, rather than an envelope of the maximum response across the $x - z$ plane. The simulation parameters used in this study were the similar to those used in the angular selectivity study, as shown in table 3-3. The number of samples along the optical axis of the hologram were reduced to decrease processing time. More steps and thus a smaller step size Δz were used in the case of the simulation involving offset construction beams, as the hologram contains more detail along \hat{z} . In each case, the NA of the objective was 0.55.

M'_x	22000	Δz	$103\mu\text{m}, 86\mu\text{m}$
M'_y	2400	Δz_s	$0, +50\mu\text{m}$
Block ratio	$4 (x); 1.25 (y)$	α	$4 \times 10^{-5}/\mu\text{m}$
Elements	6×10	$n (\lambda = 488\text{nm})$	1.49761
Δx	$0.1487\mu\text{m}$	$n (\lambda = 633\text{nm})$	1.48997
$\Delta\theta$	2.54°	Δn	7×10^{-5}

Table 3-3: General parameters for the depth selectivity simulation.

The results of the simulation method comparison for the unaberrated objective lens are shown in Figs. 3-24 and 3-25. In these figures, both gratings of hologram F3 are represented at each reconstruction wavelength used in experiment. As the diffraction efficiency was not explicitly measured in the experiment, rather integrated detector power was measured instead, the plots of all results are scaled with respect to the maximum value produced by each method. The abscissa of each plot is given as Δz_p , or displacement of the point source producing the probe beam at the pupil. Positive displacements are consistent with the direction of the $+z$ -axis in the simulation, that is, toward the objective lens. $\Delta z_p = 0$ is the longitudinal position of the nominal front focus. Table 3-4 describes the sum of the squared residuals between experimental and simulation results for each simulation method in the region $\pm 10\mu\text{m}$ from the peak. From Fig. 3-24 it is apparent that while none of the methods can exactly recreate the relative experimental curve, the RCW simulation clearly comes closest to reproducing the proper morphology, especially below 50% of the peak power. Also evident is that even though the hologram was recorded with two gratings, one with a signal point source placed at the nominal focus and another with the point source $50\mu\text{m}$ closer to the objective, or $\Delta z_s = 0, +50\mu\text{m}$, the peak reconstruction of the second, spherical grating at $\lambda_p = \lambda = 488\text{nm}$ occurs at $+38\mu\text{m}$. As the hologram has aged after being developed, or during the developing process, it has developed some internal changes to the grating structure that has caused this shift. Because of these unknown changes, it is difficult to draw a direct comparison between simulation results and experimental data. Another interesting point is evident in Fig. 3-26(b), in that the displacement of the peak response from the spherical grating at $\lambda_p = 633\text{nm}$ lies at $\Delta z_p = +65\mu\text{m}$, while the simulations all predict reconstruction positions closer to the objective.

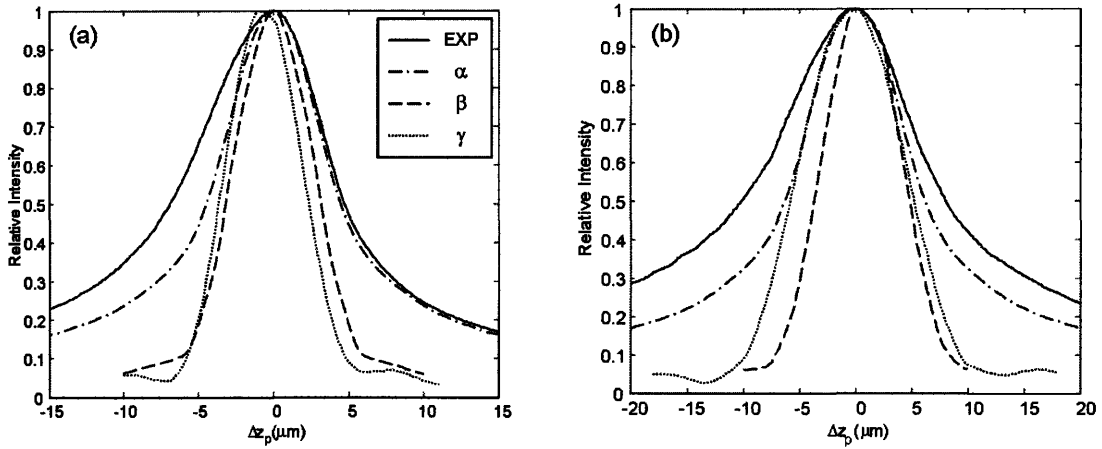


Figure 3-25: Methods for simulating the depth selectivity grating #1 (planar) of hologram F3 with experimental data. α is the RCW simulation, β is the WD simulation with idealized cylindrical geometry, and γ is the WD simulation with offset beams. (a) $\lambda_p = 488\text{nm}$, (b) $\lambda_p = 633\text{nm}$.

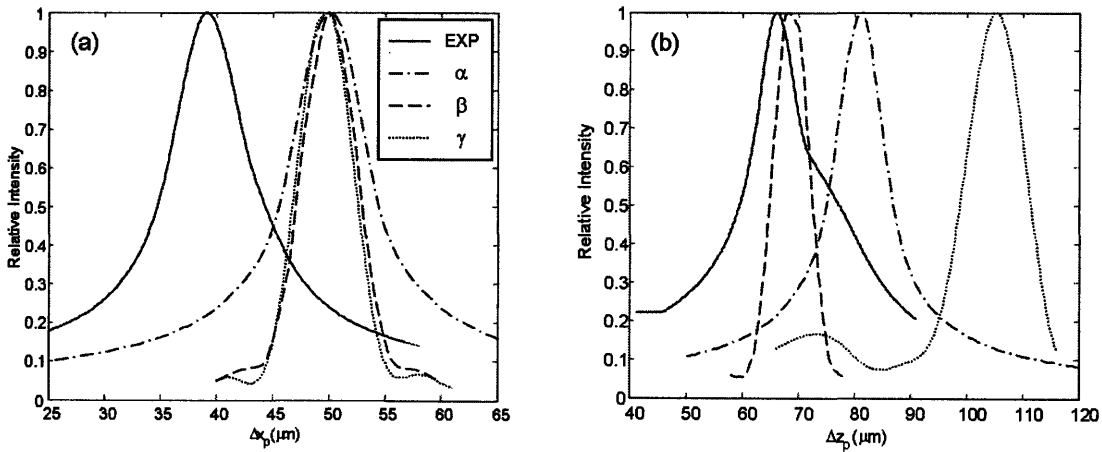


Figure 3-26: Methods for simulating the depth selectivity grating #2 (spherical) of hologram F3 with experimental data. α is the RCW simulation, β is the WD simulation with idealized cylindrical geometry, and γ is the WD simulation with offset beams. (a) $\lambda_p = 488\text{nm}$, (b) $\lambda_p = 633\text{nm}$.

Grating	RCW	WD-Cylinder	WD-Offset
F3 #1, $\lambda_p = 488\text{nm}$	0.22	1.65	2.00
F3 #1, $\lambda_p = 633\text{nm}$	0.30	2.54	1.16
F3 #2, $\lambda_p = 488\text{nm}$	0.02	1.15	1.40
F3 #2, $\lambda_p = 633\text{nm}$	0.22	2.19	0.44

Table 3-4: Sum of squared residuals for each simulation method.

This table shows that the offset-beam geometry is generally more accurate for reproducing the shape of the depth selectivity curve between the two WD methods, although RCW is still the superior method for determining the unaberrated depth selectivity. One additional point that should be discussed is the angular position of the reconstruction for each grating, as each signal beam in recording interfered with reference beams having different angles. While the idealized cylinder WD simulation agrees with the K-sphere approach, the offset case in the WD simulation provides a slightly more accurate accounting of the angle of the probe beam for Bragg-matched reconstruction than the idealized case. Table 3-5 shows the difference in angle between the probe beams required to reconstruct the reference beam in each of the two gratings in hologram F3B, for both probe wavelengths.

$\Delta\theta_p$	Exp. (F3B)	K-Sphere	WD Sim
$\lambda_p = 488\text{nm}$	$2.543 \pm 0.001^\circ$	2.543°	2.543°
$\lambda_p = 633\text{nm}$	$3.378 \pm 0.001^\circ$	3.475°	3.451°

Table 3-5: Angular separation of reconstructions: hologram F3B.

A few plots of the image plane intensity are shown in Figs. 3-27 and 3-28. It is interesting to see that the wavelength de-tuning of Fig. 3-27(b) causes the defocused point to be misaligned to the slit; an angular correction is required to Bragg-match the reconstruction in Fig. 3-28(b). Therefore, wavelength de-tuning can appear in the reconstruction as angular de-tuning, and vice-versa. This degeneracy may cause difficulty in estimating the spatial-spectral coordinates of broadband sources, especially with closely-spaced points in the object space. With the limitations of the WD simulation in mind and using the same parameters and the block-FFT

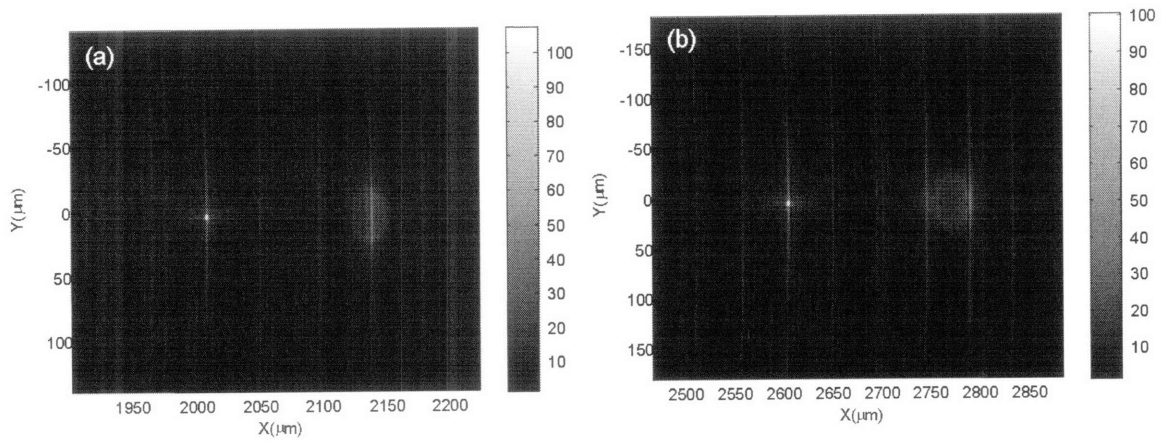


Figure 3-27: Image plane intensity to the power of 1/8 for hologram F3 in the vicinity of the first diffracted order for both gratings. Probe defocus $\Delta z_p = 0$. This model has longitudinal sampling of $\Delta z = 51.3\mu\text{m}$ and $M'_y = 3000$ at (a) $\lambda_p = 488\text{nm}$; (b) $\lambda_p = 633\text{nm}$.

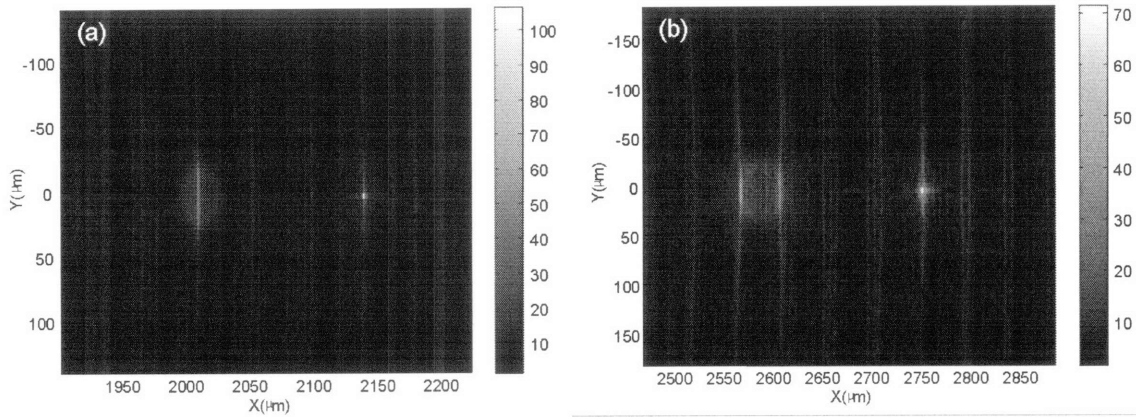


Figure 3-28: Image plane intensity to the power of 1/8 for hologram F3 in the vicinity of the first diffracted order for both gratings. This model has longitudinal sampling of $\Delta z = 85.6\mu\text{m}$ and $M'_y = 2400$ at (a) $\lambda_p = 488\text{nm}$, probe defocus $\Delta z_p = +50\mu\text{m}$; (b) $\lambda_p = 633\text{nm}$, probe defocus $\Delta z_p = +105\mu\text{m}$.

method, this study investigates the simulated response of the VHI system to a point source imaged with an aberrated objective lens. The aberration of the lens was performed in simulation by modifying the Zemax[®] lens file to include an appropriately-sized plate of BK7 glass in the diverging wavefront just prior to the microscope objective. Three of the aberrated systems from section 2.5 were simulated with Zemax[®] and the offset-beam WD simulation. The plates in the objective are detailed in table 3-6, along with the aberration coefficients at the probe wavelengths, although the microscope slide case was not simulated at $\lambda_p = 633\text{nm}$.

Type	$t(\text{mm})$	$A_{040}(\lambda_p = 488\text{nm})$	$A_{040}(\lambda_p = 633\text{nm})$
#0 Cover Slip	0.11 ± 0.01	0.91 ± 0.08	0.70 ± 0.06
#0 Cover Slip (x4)	0.43 ± 0.01	3.55 ± 0.08	2.74 ± 0.06
Microscope Slide	1.24 ± 0.01	10.24 ± 0.08	--

Table 3-6: Glass plates used in the aberration simulation.

The results of the simulation for the objective lens aberrated by a single #0 cover slip are shown in Figs. 3-29 and 3-30. Although the simulation does not significantly expand or shift the aberrated depth selectivity curve as shown in the experiment, it does appropriately induce a slight asymmetry to the curve. The response of each grating becomes larger for displacements toward the objective lens as opposed to displacements away from the objective with equal magnitude. Now applying a larger level of spherical aberration to the objective, Figs. 3-31 and 3-32 show the result of adding aberration to the objective lens with a stack of four #0 cover slips. As the effect of aberration is larger in terms of waves for the shorter wavelength, a stronger effect on the depth selectivity curve results for $\lambda_p = 488\text{nm}$. An interesting aspect of the effect of aberration on the depth selectivity is that at some level of aberration, the response curve becomes less affected at positions closer to the objective and more affected at positions away from the lens, as shown in the experimental curve from Fig. 3-32(a). Here, the long tail develops that is also present in the case of even stronger aberrations. Figure 3-33 shows the result of the simulation for the objective lens aberrated by a microscope slide, representing the most aberrated objective lens examined in this study. The predicted response closely matches the form of the experimental result, as the curve width has increased, with a continuing response away from the peak in the direction away from the objective lens. An interesting feature in

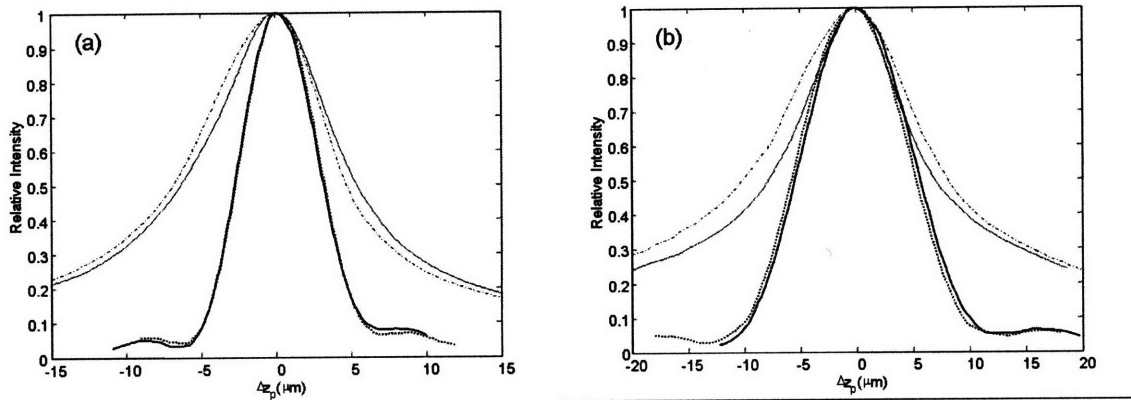


Figure 3-29: Results of simulation (bold lines) and experiment (thin lines) after aberrating the objective lens with a single #0 cover slip. The dashed lines indicate the unaberrated case. For grating F3#1 (planar): (a) $\lambda_p = 488\text{nm}$; (b) $\lambda_p = 633\text{nm}$.

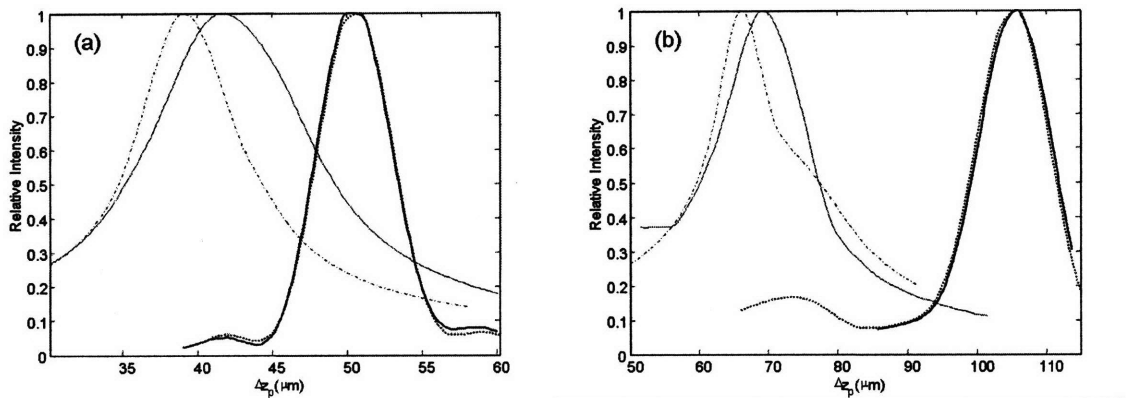


Figure 3-30: Results of simulation (bold lines) and experiment (thin lines) after aberrating the objective lens with a single #0 cover slip. The dashed lines indicate the unaberrated case. For grating F3#2 (spherical): (a) $\lambda_p = 488\text{nm}$; (b) $\lambda_p = 633\text{nm}$.

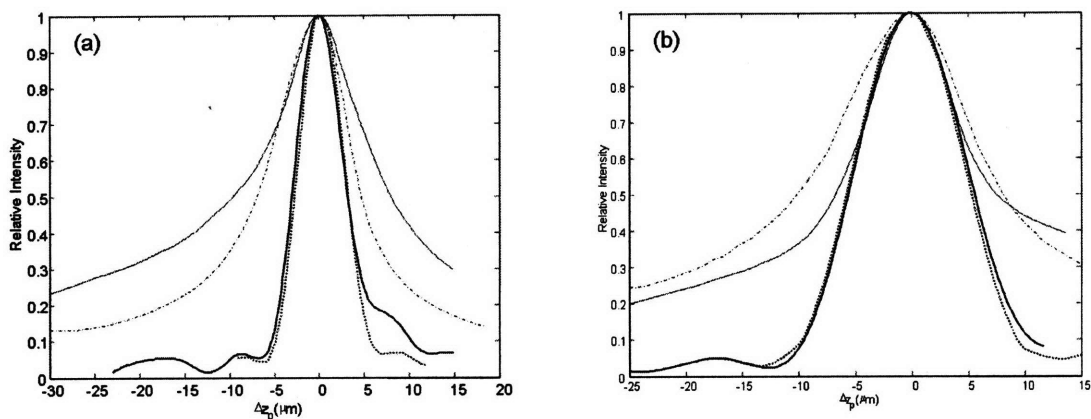


Figure 3-31: Results of simulation (bold lines) and experiment (thin lines) after aberrating the objective lens with four #0 cover slips. The dashed lines indicate the unaberrated case. For grating F3#1 (planar): (a) $\lambda_p = 488\text{nm}$; (b) $\lambda_p = 633\text{nm}$.

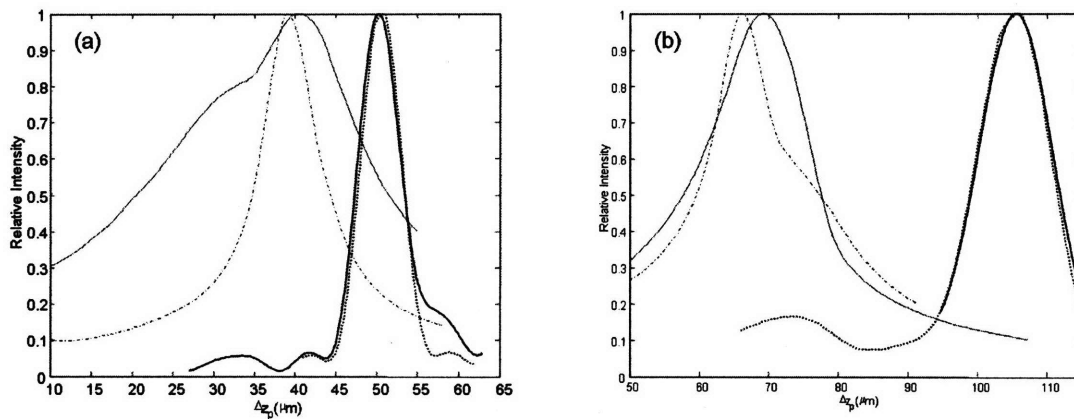


Figure 3-32: Results of simulation (bold lines) and experiment (thin lines) after aberrating the objective lens with four #0 cover slips. The dashed lines indicate the unaberrated case. For grating F3#2 (spherical): (a) $\lambda_p = 488\text{nm}$; (b) $\lambda_p = 633\text{nm}$.

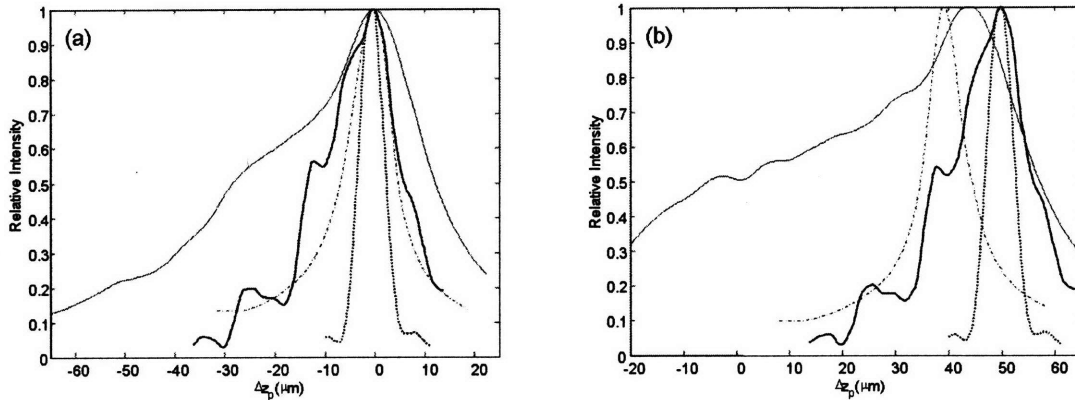


Figure 3-33: Results of simulation (bold lines) and experiment (thin lines) after aberrating the objective lens with a microscope slide. The dashed lines indicate the unaberrated case. For hologram F3 at $\lambda_p = 488\text{nm}$: (a) grating #1 (planar); (b) grating #2 (spherical).

the simulation is the oscillation in this "tail", which is also present in the experiment with a reduced magnitude. Again, the simulation does not predict the shift in the peak for the spherical grating. Interestingly, if the magnitude of the probe defocus in the simulation is doubled, the simulated response closely matches the experiment as shown in Fig. 3-34, down to the location of the peaks in the oscillating tail. Finally, the complete set of results from the simulation is summarized in Fig. 3-35. These results should be compared with Figs. 2-31 and 2-32 from the depth selectivity experiment in chapter 2. These results show that the simulation of the aberrated objective VHI system follows the general trends of the physical system in terms of peak diffraction intensity and FWHM of the depth selectivity curve. Not surprisingly, as the aberration coefficient increases, a reduction in efficiency and decrease in depth selectivity is realized. The simulation also shows that the aberration affects the two probe wavelengths differently, as the longer 633nm probe wavelength was less sensitive to aberration, at least with the relatively low levels of aberration simulated in this study. This trend is also consistent with the experimental result, although the effect of low levels of aberration increasing these performance metrics was much less pronounced in the simulation.

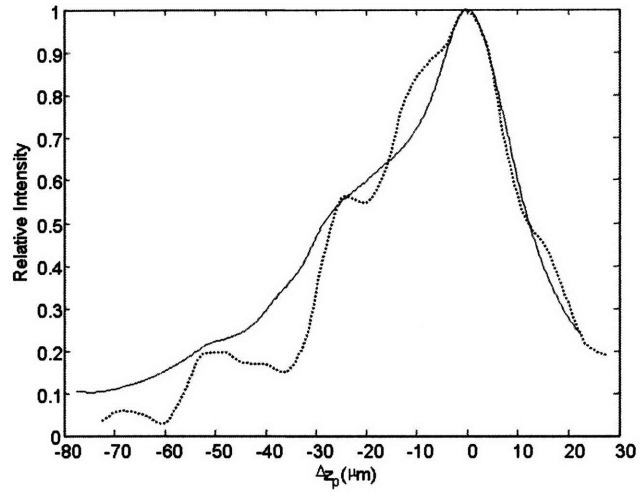


Figure 3-34: Simulated (dashed) and experimental response of grating F3#1 (planar) with a microscope slide aberrating the objective lens. Here, the plotted defocus magnitude has been doubled versus the value provided to Zemax[®].

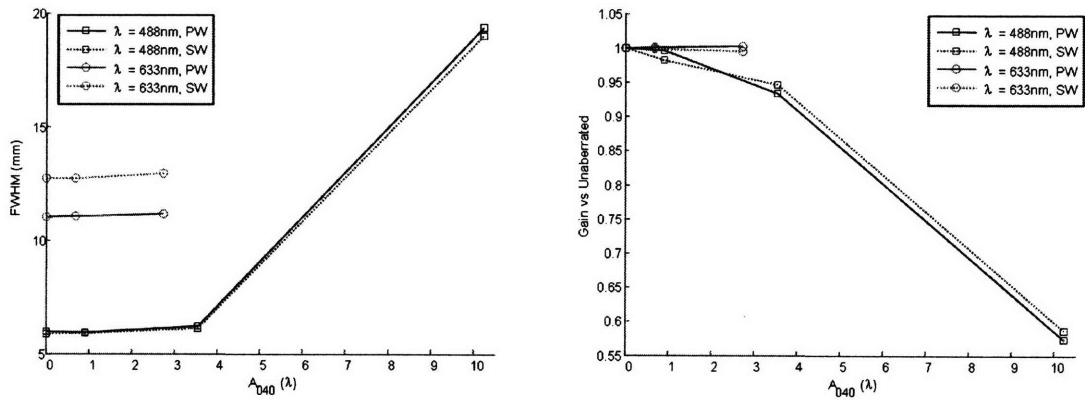


Figure 3-35: Simulated depth selectivity curve FWHM and maximum gain with respect to the unaberrated case.

Aperture apodization

The function of the hologram is to act as a heterodyne for spatial and spectral frequencies. In the vicinity of the pupil, the physical location of a point source produces a beam that has a phase profile spanning the pupil characteristic of that location. If the point source is in focus, the phase profile is constant over the pupil with a phase angle consistent with the spatial frequency of the source. If the point source lies outside of the focal plane of the objective, then the phase profile will be spherical over the pupil. For a hologram constructed with plane waves, this phase profile will not represent the correct spatial frequencies to reconstruct the reference beam to a degree. In this case, a small region of the spherical wavefront near the center of the pupil is very close to a plane wave, while the edges of the probe beam will be less so. Therefore, the response of the hologram to a mismatched probe wavefront due to defocus will still produce a small amount of response originating at the center of the pupil. If an apodization is applied to the pupil after recording such that the center of the pupil is blocked, then the depth selectivity of the hologram may be improved. To determine the shape of the apodization, the separate calculation of separate regions of the hologram by the block-FFT method was used to map the activity of each region. Using the idealized cylindrical cross-section and using the parameters of hologram S9, a single plane-wave grating. The hologram was constructed at $\lambda = 488\text{nm}$ and probed at $\lambda_p = 488\text{nm}$. The hologram aperture was divided into a grid of 10×10 equally-spaced regions and each response was calculated independently, omitting the step of phase-shifting and recombination described in the block-FFT algorithm. The variance of the intensity map was calculated for each block, as a stronger contribution from a block will generally produce a larger variance of intensity. These maps are shown in Fig. 3-36. As expected, the hologram has uniform activity when a point source probes the VHI system at the Bragg-matched position. However, the out-of-focus point source presents a spherical phase front to the hologram, and the activity map shows a vertical stripe through the center of the aperture. The slit shape arises due to the hologram being recorded in the $x-z$ plane with plane waves and therefore not acting on the components of a phase profile aligned with the y -axis. This map was used to generate the proper apodization for the pupil to minimize the response of the hologram to defocused point sources which essentially takes the form of the inverse of Fig. 3-36(b). Two apodized pupils were used, and each features an elliptical mask with the

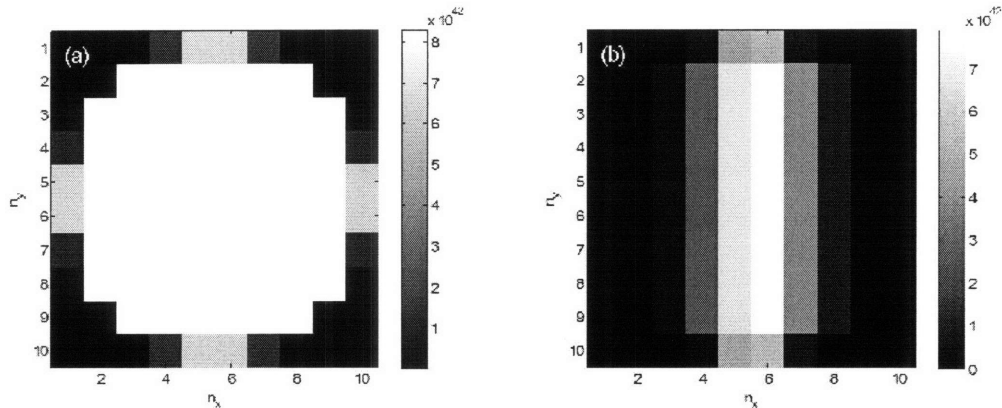


Figure 3-36: Variance of intensity for each block in the discretized aperture for a point source at (a) $\Delta z_p = 0$ (in-focus) and (b) $\Delta z_p = +18\mu\text{m}$ (out of focus).

semimajor axis aligned with \hat{y} and spanning the height of the pupil. The semiminor axis was $187.5\mu\text{m}$ for the first mask and $375\mu\text{m}$ for the second, while the semimajor axis of the outside of the pupil was approximately 2mm. The depth selectivity was analyzed for the unobscured and apodized hologram at $\lambda_p = 633\text{nm}$ with the offset-beam WD simulation. The results are shown in Fig. 3-37. The response is fairly similar for each hologram near the peak other than the loss of efficiency, however the important difference lies in the magnitude of the "tails" of the response, as the larger obscurations produce a weaker response where the probe point source is highly defocused. A drawback of this method other than a decrease in peak intensity is an increase in the FWHM of the response curve; the FWHM increases from $11.04\mu\text{m}$ to $11.33\mu\text{m}$ and $11.87\mu\text{m}$ for the largest obscuration. It is possible that if the drop in efficiency is tolerable, even larger obscurations could serve to narrow the z-PSF from the unobscured case.

3.3.3 Simulation performance

While the accuracy of the WD simulation in reproducing the experimental defocus response is not as great as the RCW simulation, the WD method does offer the ability to simulate the VHI system with arbitrary optics. The WD simulation is also quite capable of simulating the 2-D distribution of intensity on the image plane. Additionally, using the block-FFT algorithm, the WD simulation can be expanded to simulate very large holograms, or increase the accuracy of

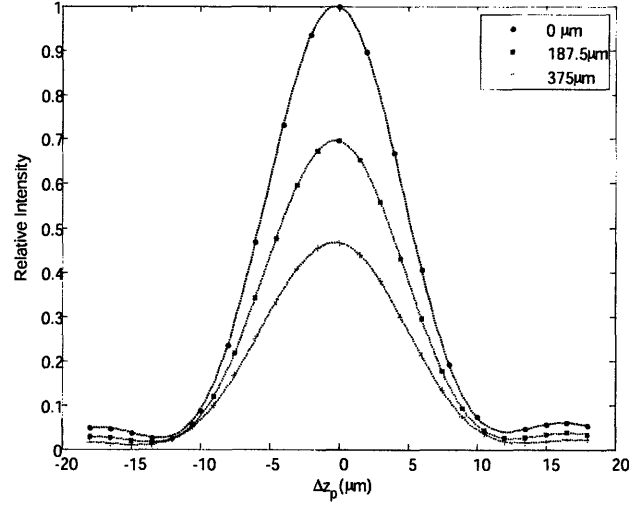


Figure 3-37: Defocus response of the VHI system with three apodizing masks of various semi-minor radii.

a smaller domain. The error in efficiency and execution time of the offset-beam WD simulation is shown in Fig. 3-38 for hologram F3 at $\lambda_p = 633\text{nm}$ and using the parameters of table 3-3. The relative error in the efficiency is with respect to a case with $N_z = 64$. From this plot it is evident that the amount of execution time required for the simulation is linear with the number of samples along \hat{z} in the hologram. This is expected as the number of operations also increases linearly with z -sampling. More interesting perhaps is the efficiency error versus sampling, as the relationship is not linear. Fitting the efficiency error to a power of the z -samples produces:

$$\Delta\eta = 0.0330 \times N_z^{-1.3935} \quad R^2 = 0.8783 \quad (\text{Defocus})$$

$$\Delta\eta = 0.0335 \times N_z^{-2.0822} \quad R^2 = 0.9863 \quad (\text{In-focus})$$

So the relationship between error and sampling for in-focus reconstruction is approximately an inverse second-power relationship. One of the interesting features in this relationship is the noticeable "hump" in the error at the point where $N_z = 18$. The precise cause of this feature is unknown. It is possible that the error increase relates to the approximate location of the recording and probe beams becoming more accurate through the hologram as sampling

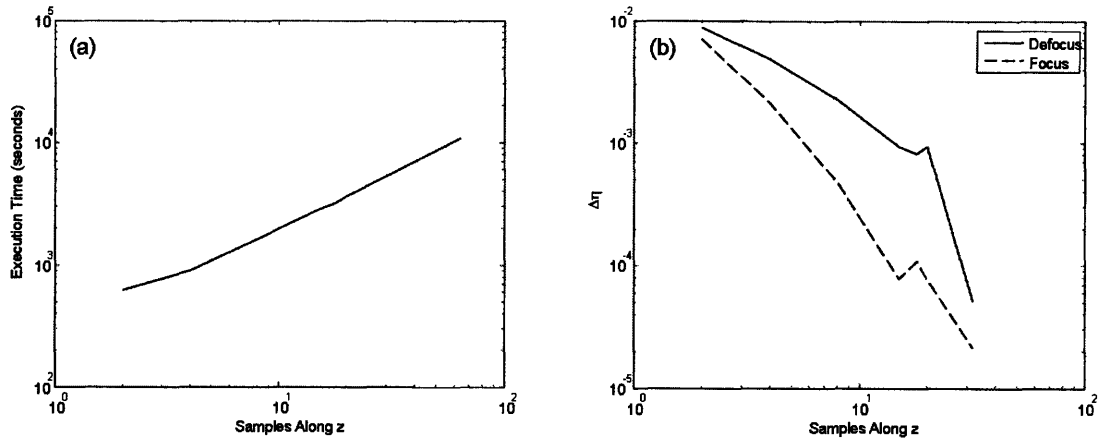


Figure 3-38: (a) Execution time of the simulation versus the number of sample points inside the hologram along \hat{z} . (b) Error in the efficiency calculation versus the number of sample points inside the hologram along \hat{z} for both gratings. As $\Delta z_p = 0$, The focus case represents grating #1, while the defocus case is grating #2.

increases, although again there is no specific reason for an increase in error at this specific sampling. The WD simulation is a very flexible and simple method for simulating VHI systems. While the accuracy of the WD method is inherently lower than RCW as there is no coupling of electric fields inside the grating, the simulated diffraction efficiency is at least within an order of magnitude of the experimental data. Accuracy is improved when assuming planar wavefronts in constructing and reading the hologram, such as in the angular selectivity study. The WD simulation is less accurate in simulating the depth selectivity, with higher accuracy toward the Bragg-matched peak. Generally lower accuracy exists away from the peak, especially at diffraction efficiencies below 50% of the peak value. Prior studies indicate more accuracy in depth selectivity with lower NA objectives, so it is possible that the method of simulating the various beam phase profiles with Zemax[®] is a source of inaccuracy. The Feb. 3 2005 version of Zemax[®] used here does not operate in an afocal mode but rather requires an artificial focal element in the system to generate a wavefront map. Later versions of Zemax[®] are capable of providing a wavefront map for an afocal system, however it is possible that this ad-hoc solution for the phase profile near the pupil is not as accurate, especially for a large NA system. Where aberrations are severe and dominate the phase topology however, the WD simulation

and experimental data begin to look more alike. It is in this domain of simulation that the WD simulation is most relevant, as the method can calculate the image plane intensity for any object function and any wavefront phase profile, subject to the inherent limitations of the 1st-order Born approximation.

Chapter 4

Discussion and Conclusions

4.1 Summary of results

In this work, the 3-D spatial-spectral heterodyning behavior inherent in VHI has been shown to be competitive with similar systems. A method of designing a resolution target that is able to simultaneously probe the sectioning capabilities of VHI for a hyperspectral volume has been introduced, and preliminary imagery of this target has provided insight into initial system performance metrics that have previously been qualitative or theoretical. The performance of the VH as a spatial filter was also examined in detail, both in theory and experiment. It has been shown here how wavelength shifts quantitatively affect the lateral position selectivity of the VH, such that reading the hologram with longer wavelengths than in recording provide a more detrimental effect to both the lateral selectivity and diffraction efficiency than even RCW simulations would predict. Additionally, these effects were examined in multiplex grating VHs showing the sensitivity of spherical gratings to these parameters, which was typically greater than in the case of planar gratings. The depth selectivity of VHI was also investigated, where the particular parameters of recording geometry, lateral probe position, and probe wavelength were discussed. It was found that longer probe wavelengths than used in recording reduced the depth discrimination capabilities of VHI. It was also found that lateral displacements of a point source caused a significant reduction in the depth discrimination as well. Finally, these effects were found to have a more substantial impact upon spherical gratings, related to the recording geometry. Taking this a step further, the effect of spherical aberration on the

multiplex grating VHI system was investigated. It was found experimentally that the spherical aberration, at low levels, has the potential to actually improve the diffraction response and depth selectivity. Whether this is an inherent aspect of VHI or simply a factor related to the specific use of a particular VH is not known, however the imaging through strong aberration was found to be deeply affected, with sharply reduced depth selectivity and diffraction response for both measured wavelengths. The final experiment that was performed was imaging of onion peel with a five-grating VHI system to determine the possibilities for reconstruction of a 3-D volume based on the 2-D information at the focal plane, and the examination of various image processing methods for their suitability in aiding in feature identification and image quality. In this work, a weak diffraction method for simulating the response of VHI was discussed as a possible method for better understanding more realistic aspects of VHI than have been simulated previously, such as aberration, multiplex gratings, and vignetting of the hologram aperture. Some basic equations governing the simulation were derived. Also discussed for the first time is the arc-like appearance of the Bragg slit in the image plane, which has been shown in experiment and numerical simulation. A paraxial equation has been derived which for the first time mathematically describes the source of this feature and its consequences for imaging. The weak diffraction simulation was implemented in Matlab[®], and it was shown how this simulation takes the powerful step of interfacing directly with the optical design code Zemax[®] for an accurate simulation of the non-diffractive optics in VHI. Initial studies of depth selectivity and the effect of objective lens aberrations were performed, however to re-create the experimental conditions, a new parallelized version of the simulation was written with pMatlab, and run on the grid computer LLGrid at MIT/Lincoln Laboratory. These simulations paralleled the efforts of the experiment, namely the angular selectivity, depth selectivity, and response to aberration were investigated at the experimental wavelengths and with multiplex gratings mimicking the real recording conditions. The simulation was found to capture the angular selectivity of the VH element quite well, and was even able to provide reasonable predictions of the peak diffraction efficiency of the VH, given the approximate nature of this parameter in simulation. In the case of depth selectivity, the prediction of the response magnitude of VHI versus depth was found to be inferior to RCW analysis, however the relative change between various probing conditions was still somewhat accurate. Better was the accuracy in the case

of response to aberration; with high levels of spherical aberration the weak diffraction model produced reasonable predictions of the changes to the defocus response curve. This shows that while still requiring improvement, the parallel weak diffraction model has the potential to be an accurate means of assessing arbitrary changes in the recording or imaging environment for VHI systems.

4.2 Discussion

In this work, attention has been paid to the somewhat arbitrary although well-known and generally used generic imaging metrics for evaluating the filtering behavior of the VH. Due to the somewhat unconventional images generated by VHI, it will be fruitful to have a short discussion about resolution as it may be defined for VHI. One of the oft-discussed issues in VHI is the degeneracy between spatial and spectral coordinates. A potential solution to this problem might include the use of a multiple-color detector array, so that the detector itself has some inherent spectral resolution. In other words, the spectral resolution of a single detector element can be augmented such that each element is by itself capable of discriminating a number of different wavelengths. In fact, an imaging CCD that claims to be a broadband intensity detector array actually does have the property of being spectrally selective to a degree, and therefore contributes spectral resolution. For example, a CCD array that is sensitive to visible wavelengths would not be expected to sense LWIR wavelengths. This is typical of any physical detector, so any detector will affect the spectral resolution of a system. So what, then, is a useful way to define the resolution of such a system? Perhaps the beginning of a useful definition might lie in examining the system from the point of view of information theory. Using this approach, it might be possible to determine the maximum achievable resolution or, more precisely, the maximum amount of mutual information available to classify a spatial-spectral source. Alternatively, one could determine the theoretical minimum covariance for a particular estimator. This minimum bound, also known as a Cramer-Rao lower bound, provides a very intuitive result in the case of this imaging system, as the bound has a direct relationship to the minimum dimensions of the volume-hyperspectral element. Unfortunately in terms of information processing the VHI system is spatially shift-variant and contains four degrees

of freedom (assuming a single-color detector array) necessitating a large system information matrix. However this method does have the benefit of allowing great detail in the way the system response is modeled, presumably creating a more optimal estimator. Also, a priori information about the image background might be applied to improve the estimator. Another issue encountered so far is evident is a striking feature of some of the VHI micrographs in section 2.6, particularly those involving the resolution target. One can easily see that not all out-of-focus light has been rejected from the fluorescent features of the source that lie outside any of the image planes. This is quite problematic, as this type of response, assuming an ideal VHI system, would be interpreted as a diffuse source at the depth encoded into the diffracted image slice, rather than out-of-focus light from other planes. While this might occur in media with multiple scattering properties (such as the onion peel, where this effect cannot be seen), the resolution target was specifically designed to avoid multiple scattering. A clue to the nature of this problem lies in the depth selectivity curves shown in section 2.4. The concept of a "perfect" VHI system would be one that has sharply delineated voxels, such that in the space domain each grating images a 3-D form of the 2-D "rect" function. In this sense, the response of each grating outside of its intended imaging volume could be considered noise. In the case of ample optical power received at the image plane such that statistical detector-related noise is not significant, this concept defines a system or application signal to noise ratio that can be used to determine the merit of a specific VHI configuration in imaging a specific object.

4.3 Future work

The concept of VHI has many potential areas of fruitful research possibilities. In terms of improving the capabilities of VHI as envisioned here, some possibilities include working to understand the extent to which the thick grating causes aberration with de-tuned probe beams. In simulation it has been shown that defocus can cause astigmatism in the reconstruction, even at the recording wavelength. Qualitatively, this has been observed in the reconstructions of the spherical gratings in multiplex holograms. It may be possible to construct a recording method that would conjugate those aberrations, leaving a diffraction-limited reconstruction for any grating. It will also be necessary to work at constructing holograms that are multiplexed

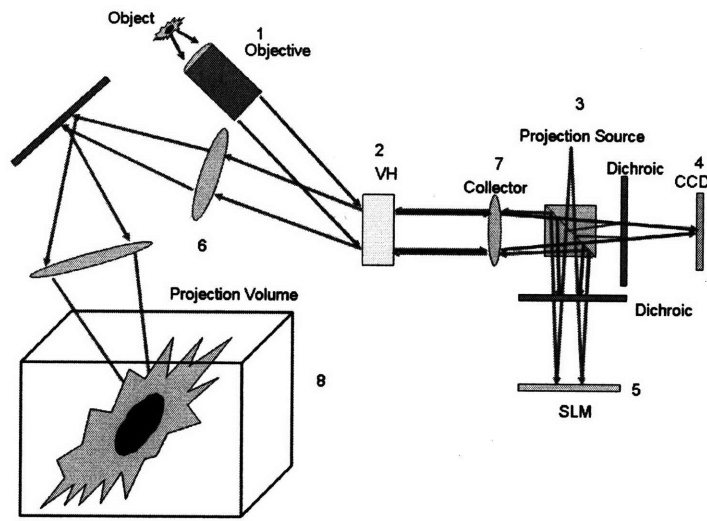


Figure 4-1: Configuration for the concept of the simultaneous VHI and VH projection device.

to a much greater degree than those described here for practical real-time medical imaging. Working to extend the limit of the number of possible gratings and the ability to simultaneously capture and process the response from such will be very important for this concept to succeed. There are other possibilities for VH optical elements beyond imaging and holographic data storage. One such possibility was disclosed by the author and Prof. Barbastathis at MIT [53]. This concept combined the VHI idea with a parallel projection method, such that parallel hyperspectral 3-D data from a long-wavelength illumination source would be recorded by a computer. This computer would then control a spatial light modulator, which would then project the illumination pattern of the image plane through the VH in the conjugate mode and at a shorter wavelength by means of a beam splitter. The change in wavelength allows the reconstruction of the object volume to be diffracted by the VH at a different global angle than that of the incoming light, and therefore reach a different optical path. In the envisioned application, imaging would take place through a microscope objective, while projection would be through a magnifying element. Reconstruction of the object intensity would then take place inside a larger volume of space, which could be a macroscopic volume of fluorescent material, as in figure. This concept could enable the real-time imaging of biological processes in real-time and 3-D. In conclusion, the possibilities presented by VHI and VH optical elements are

intriguing, and merit additional investigation. It is hoped that VHI will eventually enable low-cost and high fidelity 3-D medical imaging systems to improve the diagnosis and treatment of disease.

Bibliography

- [1] D. Gabor, "A new microscopic principle," *Nature* 161: 777-779 (1948).
- [2] G. Barbastathis, M. Balberg, and D. J. Brady, "Confocal microscopy with a volume holographic filter" *Opt. Lett.* 24(12): 811-813 (1999).
- [3] W. Liu, D. Psaltis, and G. Barbastathis. "Real-time spectral imaging in three spatial dimensions," *Opt. Lett.* 27(10): 854-856 (2002).
- [4] A. Sinha and G. Barbastathis, "Volume holographic imaging for surface metrology at long working distances," *Opt. Express* 11(24): 3702-3209 (2003).
- [5] A. Sinha, W. Liu, D. Psaltis, and G. Barbastathis, "Imaging using volume holograms," *Opt. Eng.* 43(9): 1959-1972 (2004).
- [6] I. Bányász, "Model of holographic recording in thermoplastic materials," *Appl. Opt.* 37(11): 2081-2086 (1998).
- [7] Y. Luo, P. J. Gelsinger, J. K. Barton, G. Barbastathis, and R. Kostuk, "Optimization of multiplexed holographic gratings in PQ-PMMA for spectral-spatial imaging filters," *Opt. Lett.* 33(6): 566-568 (2008).
- [8] B. L. Liang, Z. Q. Wang, G. G. Mu, J. H. Guan, and R. L. Fu, "Effect of the reading beam on the diffraction efficiency of volume grating in Ce:KNSBN," APCC/OECC '99. Fifth Asia-Pacific Conference on Communications and Fourth Optoelectronics and Communications Conference. (1999).

- [9] K. Y. Hsu, S. H. Lin, Y. N. Hsiao, and W. T. Whang, "Experimental characterization of phenanthrenequinone-doped poly(methylmethacrylate) photopolymer for volume holographic storage," *Opt. Eng.* 42(5): 1390–1396 (2003).
- [10] T. Woike, M. Imlau, S. Haussühl, R. A. Rupp, and R. Schieder, "Photorefractive behavior of Ba[Fe(CN₅)NO]·3H₂O in the red and near-infrared spectral range," *Phys. Rev. B.* 58(13): 8411-8415 (1998).
- [11] F. Kahmann, J. Höhne, R. Pankrath, and R. A. Rupp, "Hologram recording with mutually orthogonal polarized waves in Sr_{0.61}Ba_{0.39}Nb₂O₆:Ce," *Phys. Rev. B.* 50(4): 2474-2478 (1998).
- [12] T. Kojima and Y. Tomita, "Characterization of Index and Surface-Relief Gratings Formed in Methacrylate Photopolymers," *Opt. Review.* 9(5): 222-226 (2002).
- [13] CTIS Function. <http://www.optics.arizona.edu/descour/computed.htm>, accessed 4/18/2008.
- [14] C. J. R. Sheppard and T. Wilson, "The theory of the direct-view confocal microscope," *J. Microscopy* 124(2): 107-117 (1981).
- [15] H. U. Dodt and K. Becker, "Confocal microscopy in transmitted light," *Proc. SPIE* 5139: 79-87 (2003).
- [16] C. J. R. Sheppard and T. Wilson, "Depth of field in the scanning microscope," *Opt. Lett.* 3(3): 115-117 (1978).
- [17] I. J. Cox, C. J. R. Sheppard, and T. Wilson, "Improvement in resolution by nearly confocal microscopy," *Appl. Opt.* 21(5): 778-781 (1982).
- [18] D. W. Piston, "Imaging living tissues by two-photon excitation microscopy," *Trends in Cell Biology* 9: 66-69 (1999).
- [19] X. Michalet, et. al., "The Power and Prospects of Fluorescence Microscopies and Spectroscopies," *Annu. Rev. Biophys. Biomol. Struct.* 32: 161–182 (2003).

- [20] J. M. Schmitt, "Optical Coherence Tomography (OCT): A Review," *IEEE Journal of Selected Topics in Quantum Electronics* 5(4): 1205-1215 (1999).
- [21] E. A. Swanson, et. al., "In vivo retinal imaging by optical coherence tomography," *Opt. Lett.* 18(21): 1864-1866 (1993).
- [22] Evident Technologies - EviDot Specifications.
<http://www.evidenttech.com/products/evidots/evidot-specifications.html>, accessed 3/10/2008.
- [23] M. Montecchi and Q. Ingram, "Study of some optical glues for the compact muon solenoid at the large hadron collider of CERN," *Nuclear Instruments and Methods in Physics Research Section A: Accelerators, Spectrometers, Detectors, and Associated Equipment* 465: 329-345 (2001).
- [24] M. Bruchez, et al., "Semiconductor nanocrystals as fluorescent biological labels," *Science* 281: 2013-2016 (1998).
- [25] A. Waggoner, "Covalent Labeling of Proteins and Nucleic Acids with Fluorophores," *Methods in Enzymology* 246: 362-373 (1995).
- [26] "Method of Determining the Resolution Power of Photographic Lenses" NBS circular 533-1953
- [27] D.K. Hamilton, T. Wilson, and C.J.R. Sheppard, "Experimental observations of the depth-discrimination properties of scanning microscopes," *Optics Letters* 6(12): 625-626 (1981).
- [28] U.S. Patent 3,013,467. Filed Nov. 7 1957. Patented Dec. 19 1961.
- [29] D. Huang, et al., "Optical Coherence Tomography," *Science* 254: 1178-1181 (1991).
- [30] F. Zernike, "Diffraction theory of the knife-edge test and its improved form, the phase-contrast method," *Physica I* 689-704 (1934).
- [31] M. Born and E. Wolf, *Principles of Optics* 7th ed. (Cambridge University Press, 1999), pp. 287-289, 524-543, 701-707.

- [32] S. C. Lee, W. Inami, and Y. Kawata, "Volume Holographic Device for Spherical Aberration Correction and Parallel Data Access in Three-Dimensional Memory," *Jpn. J. Appl. Phys.* 40: 1796-1797 (2001).
- [33] A. Sinha, W. Sun, T. Shih, and G. Barbastathis, "Volume holographic imaging in the transmission geometry," *Appl. Opt.* 43(4): 1533-1551 (2004).
- [34] G. Barbastathis, "Spatial and spectral filtering with weakly diffracting three-dimensional optical elements," Unpublished work.
- [35] J. W. Goodman, *Introduction to Fourier Optics* 3rd ed. (McGraw-Hill, 2005), pp. 10-26, 46-76, 97-103, 332, 350-356.
- [36] O. Momtahan, et al., "Spherical beam volume holograms for spectroscopic applications: modeling and implementation," *Appl. Opt.* 43(36): 6557-6567 (2004).
- [37] O. Momtahan, C. R. Hsieh, A. Adibi, and D. J. Brady, "Analysis of slitless holographic spectrometers implemented by spherical beam volume holograms," *Appl. Opt.* 45(13): 2955-2964 (2006).
- [38] H. Kogelnik, "Coupled-wave theory for thick hologram gratings," *Bell System Technical Journal* 48: 2909 (1969).
- [39] Tony Nichol, Pers. Comm. 10-17-2007.
- [40] M. Gu, *Advanced Optical Imaging System Theory* (Springer, 1999).
- [41] D. Malacara and M. Malacara, *Handbook of Optical Design* 2nd ed. (Marcel Dekker, 2004), pp. 73-102.
- [42] J. M. Watson, P. Wissmann, S. B. Oh, M. Stenner, and G. Barbastathis, "Computational optimization of volume holographic imaging systems," OSA Topical Meeting on Computational Optical Sensing and Imaging (COSI), Vancouver, BC; paper CMD3 (2007).
- [43] D. P. Coufal and G. T. Sincerbox eds., *Holographic Data Storage* (Springer, 2000).
- [44] G. Barbastathis, S. B. Oh, and P. Wissmann, "3-D Optics: Applications to Imaging," *Proc. of SPIE* 6392(63029G) (2006).

- [45] E. Popov and M. Nevière, *Light Propagation in Periodic Media* (Marcel Dekker, 2003).
- [46] MDO and Montage Program Background. (n.d.).
<https://montage.ece.arizona.edu/public/other/montagePR.pdf>, accessed 2/9/2007.
- [47] ZEMAX[®] Optical Design Program User's Guide, February 3, 2005 version. ZEMAX Development Corporation.
- [48] M. Frigo and S. G. Johnson, "The Design and Implementation of FFTW3," *Proc. of IEEE* 93(2), 216–231 (2005).
- [49] A. V. Oppenheim, R. W. Schaffer, and J. R. Buck, *Discrete-Time Signal Processing* 2nd ed. (Prentice Hall, 1999), pp. 582-588, 621.
- [50] N. T. Bliss, R. Bond, J. Kepner, H. Kim, and A. Reuther, "Interactive Grid Computing at Lincoln Laboratory," *Lincoln Laboratory Journal* 16(1): 165-216 (2006).
- [51] J. O. Smith. *Mathematics of the Discrete Fourier Transform (DFT) with Audio Applications* 2nd ed. online book (2007) <http://ccrma.stanford.edu/~jos/mdft/>, accessed 4/1/2008.
- [52] E. Hecht, *Optics* 4th ed. (Addison Wesley, 2002), pp. 115, 120, 494.
- [53] MIT case no. 12680

Appendix A

Matlab[®] Code Samples

This page left blank.

```

%%%%%%%%%%%%%%%%%%%%%%%%%%%%%%%%%%%%%%%%%%%%%%%%%%%%%%%%%%%%%%%%%%%%%%%%
% process_separate_VH_blocks.m
% script .m file
% Jonathan M. Watson 3/10/2008
%
% This script is central to the calculation of the VHI image plane
% response. It reads files generated from Zemax by
% generate_VH_probe_files.m and generate_VH_object_files.m and calculates
% the response with the VH_integrand function.
%%%%%%%%%%%%%%%%%%%%%%%%%%%%%%%%%%%%%%%%%%%%%%%%%%%%%%%%%%%%%%%%%%%%%%%%

%% Initialize pMatlab.

PARALLEL = 1;

% Load parallel simulation parameters.
load('VH_header.mat');
clear N_procs

if (PARALLEL)
    pMatlab_Init;
    Ncpus = pMATLAB.comm_size;

    % Rank is the unique number identifying the processor. The "leader" is
    % rank 0.
    my_rank = pMATLAB.my_rank;

    % Define the "map" for the distributed matrix that will be used to sum
    % the phase-shifted pupil plane amplitudes to reconstruct the image
    % plane.
    map1 = map([1 1 Ncpus], {}, 0:Ncpus-1);
else
    my_rank = 1;
end

% This parameter tells the simulation how many blocks are assigned to each
% processor. This can be any number from 1 to the total number of blocks.
cpu_frac = decimate_cpus;

%% Analysis.
% To be executed separately by each processor in the complex.
for n_5 = 1:cpu_frac

    % Determine the current block ID being worked on.
    who_am_i = my_rank*cpu_frac + n_5;

    % Load data files
    load(['VH_object_data_', num2str(who_am_i), '.mat']);
    load(['VH_probe_data_', num2str(who_am_i), '.mat']);
    proc_data.probe = probe_data;
    clear probe_data;

    q = zeros(Mpy, Mpx);

    % Use most efficient algorithm for 2-D fft for non-powers of two.
    fftw('planner', 'patient');

    % Create matrices for x-y spatial frequencies.
    [u, v] = meshgrid((-Mpx/2:Mpx/2-1), (-Mpy/2:Mpy/2-1));
    u = ifftshift(u);
    u = u.*du;
    v = ifftshift(v);
    v = v.*dv;

    % Calculate spectral radius.
    rho = (u.^2 + v.^2).*(1/uEC)^2;

```

```

% Create mask for the transfer function to eliminate any evanescent
% results.
H_mask      = true(Mpy,Mpx);
H_mask(rho>=1) = false;
clear('rho');

% Calculate the exponent of the transfer function, without the depth
% term.
H_kernel    = sqrt(1-((u.^2 + v.^2).*(1/uEC)^2)).*(-2*pi*nu(2)/lambda_read).*H_mask;

% Calculate the exponent of the phase shift for each block
q_kernel    = -2*pi.*(u.*blk.center(who_am_i,1) + v.*blk.center(who_am_i,2));
clear('u','v');

% Create the grid of spatial coordinates near the pupil.
[blk.xpp,blk.ypp] = meshgrid((-Nx/2+0.5):(Nx/2-0.5).*dxpp,((-Ny/2+0.5):(Ny/2-
0.5)).*dxpp);
blk.xpp      = (blk.xpp+blk.center(who_am_i,1));
blk.ypp      = single(blk.ypp+blk.center(who_am_i,2));

n_1 = 0;

% Perform integration
for z = -(Nz-1)/2:(Nz-1)/2

    n_1 = n_1 + 1;
    zpp = z*step_size_z;

    % Calculate the normalized intensity of each beam at coordinate
    % zpp.
    I_norm = exp(-(zpp+L/2)*absorb);

    % calculate the image plane response for this depth plane.
    q = q + VH_integrand(proc_data,I_norm,zpp,mux,theta,reference_angle,...
        lambda,lambda_read,nu,simple_ref,probe_angle,Nx,Ny,delta_nu,...
        step_size_z,n_1,simple_sig,Mpx,Mpy,R_ref,R_sig,R_prb,dot_radius,do_offsets,...
        simple_probe,blk.xpp,blk.ypp,L1).*exp(H_kernel.*i*zpp).*H_mask;

end

clear('H_mask','H_kernel');

% Apply block phase shift.
q = q.*exp(q_kernel.*i);

clear('blk','q_kernel');

% finish up
% each processor saves its own coded data file

q = fftshift(q);

% Save only a portion of the image plane to reduce memory requirement.
x_indices{1} = (floor(Mpx*4.2/16)+850):(ceil(Mpx*6/16)-500);
x_indices{2} = (floor(Mpx*10/16)+500):(ceil(Mpx*11.8/16)-850);

top_limit = floor(Mpy/2-35);
bottom_limit = ceil(Mpy/2+35);

qq(:, :, n_5) = q(top_limit:bottom_limit,x_indices{1});
rr(:, :, n_5) = q(top_limit:bottom_limit,x_indices{2});

end

clear q

disp(['formed qq, size ',num2str(size(qq))]);

```



```

disp(['formed rr, size ',num2str(size(rr))]);

% Generate the distributed matrix.
q_D = zeros(size(qq,1),size(qq,2),Ncpus*cpu_frac,map1);
disp('Done creating dmat');

% Put local portions of dmat into the global dmat.
q_D = put_local(q_D,qq);
disp('Done put local');

% Now put the entire global dmat into the leader memory.
qp = agg(q_D);
disp('Done agg q_D');
clear qq

% The leader processor sums the 3-D stack of block contributions.
if my_rank == 0
    q = sum(qp,3);
    clear qp;
end

% Now do the same with the other portion of the image plane selected.
r_D = zeros(size(rr,1),size(rr,2),Ncpus*cpu_frac,map1);
disp('Done creating dmat');
r_D = put_local(r_D,rr);
disp('Done put local');
rp = agg(r_D);
disp('Done agg r_D');
clear rr
if my_rank == 0
    r = sum(rp,3);
    clear rp;
    q = horzcat(q,r);
    save_str = datestr(now);
    save(['q_box',save_str([1:14,16,17,19,20]),'_',...
        '100.mat'],'q');
end

% Finalize the pMATLAB program.
disp('SUCCESS');

if (PARALLEL)
    pMatlab_Finalize;
end

!echo finished > done.txt

%%%%%%%%%%%%%%%%%%%%%%%%%%%%%%%%%%%%%%%%%%%%%%%%%%%%%%%%%%%%%%%%%%%%%%%%
%%%%%%%%%%%%%%%%%%%%%%%%%%%%%%%%%%%%%%%%%%%%%%%%%%%%%%%%%%%%%%%%%%%%%%%%
% VH_integrand.m
% function .m file
% Jonathan M. Watson 3/10/2008
%
% This function has numerous inputs, but only one output; the image plane
% field contribution from the object at the location zpp.
%
% Inputs:
% 1. proc_data: # of block being processed
% 2. I_norm: normalized intensity for the beams at zpp
% 3. zpp: axial coordinate in pupil space
% 4. mux: number of multiplexed gratings
% 5. theta: 1x2 matrix of internal recording angles
% 6. reference_angle: internal angle of reference beam
% 7. lambda: freespace recording wavelength
% 8. lambda_read: freespace probe wavelength
% 9. nu: 1x2 matrix of index of refraction for write and read wavelengths

```

```

% 10.simple_ref: binary; do simple (non-Zemax) reference beam
% 11.probe_angle: internal angle of probe beam
% 12.Nx: size of the non-zero data along x
% 13.Ny: size of the non-zero data along y
% 14.delta_nu: change in index of refraction from recording
% 15.step_size_z: width of depth slice
% 16.n_1: # of current depth slice
% 17.simple_sig: binary; do simple (non-Zemax) signal beam
% 18.Mpx: total size of block along x
% 19.Mpy: total size of block along y
% 20.Rr: 1x2 matrix of semimajor and semiminor axis of reference beam edge
% 21.Rs: 1x2 matrix of semimajor and semiminor axis of signal beam edge
% 22.Rp: 1x2 matrix of semimajor and semiminor axis of probe beam edge
% 23.dot_radius: semiminor axis of center obscuration of probe beam
% 24.do_offsets: binary; false is do idealized cylinder model
% 25.X: matrix of x coordinates in pupil space
% 26.Y: matrix of y coordinates in pupil space
% 27.L1: structure of objective lens parameters; L1.f is focal length
% (that's all you need in the structure).
%%%%%%%%%%%%%%%%%%%%%%%%%%%%%%%%%%%%%%%%%%%%%%%%%%%%%%%%%%%%%%%%%%%%%%%%

function q = VH_integrand(proc_data,I_norm,zpp,mux,theta,reference_angle,...
    lambda,lambda_read,nu,simple_ref,probe_angle,Nx,Ny,delta_nu,step_size_z,n_1,...
    simple_sig,Mpx,Mpy,Rr,Rs,Rp,dot_radius,do_offsets,simple_probe,X,Y,L1)

% Initialize the field variables.
q = zeros(Mpy,Mpx);
g = zeros(Ny,Nx);

% Generate the object function.
epsilon = VH_object_fresnel(proc_data,X,Y,Nx,Ny,zpp,mux,theta(2),reference_angle,...
    lambda,nu,simple_ref,simple_sig,n_1,Rr,Rs,do_offsets,lambda_read,step_size_z,...
    delta_nu,I_norm,L1);

% Determine the center of the probe beam at this depth plane in x-y
% coordinates.
if do_offsets
    center_of_probe_beam = zpp*tan(probe_angle);
else
    center_of_probe_beam = 0;
end

% Define the edges of the probe beam with a binary mask.
probe_mask = circap5(X,Y,Rp(1),Rp(2),dot_radius/cos(probe_angle),...
    dot_radius,center_of_probe_beam);

if simple_probe

    % If an idealized case is necessary, the probe beam can be generated
    % using these formulas instead of generating a wavefront map with Zemax
    % and interpolating.
    if L1.defocus
        P = probe_mask.*defocused_plane_wave(X-
center_of_probe_beam,Y,zpp,L1.defocus/nu(2),lambda_read/nu(2),probe_angle,L1.f);
    else
        P = exp(i*2*pi/lambda_read*nu(2)*(cos(probe_angle)*zpp + ...
            sin(probe_angle).*(X))).*probe_mask;
    end
end

% Interpolate Zemax wavefront map.
P = VHI_interp_wfm(proc_data.probe.wfm{n_1}(:,,:),Nx,Ny,zpp,probe_angle,...
    lambda_read,nu(2),X);

end

clear('X','Y');

```

```

% Calculate the weak diffraction response g.
g(probe_mask) = (P(probe_mask).*epsilon(probe_mask))*I_norm;

% Calculate the Fourier transform of the weak diffraction g.
clear('P','epsilon','probe_mask');
q((Mpy/2-Ny/2):(Mpy/2+Ny/2-1),(Mpx/2-Nx/2):(Mpx/2+Nx/2-1)) = g;
clear('g');
q = fft2(q);

return;

%%%%%%%%%%%%%%%%%%%%%%%%%%%%%%%%%%%%%%%%%%%%%%%%%%%%%%%%%%%%%%%%%%%%%%%%
%%%%%%%%%%%%%%%%%%%%%%%%%%%%%%%%%%%%%%%%%%%%%%%%%%%%%%%%%%%%%%%%%%%%%%%%
% VH_object_fresnel.m
% function .m file
% Jonathan M. Watson 3/10/2008
%
% This function has numerous inputs, but only one output; the phase object
% function at axial location z.
%
% Inputs:
% 1. proc_data: # of block being processed
% 2.X: matrix of x coordinates in pupil space
% 3.Y: matrix of y coordinates in pupil space
% 4.Nx: size of the non-zero data along x
% 5.Ny: size of the non-zero data along y
% 6. z: axial coordinate in pupil space
% 7. mux: number of multiplexed gratings
% 8. theta_sig: internal angle of signal beam
% 9. theta_ref: internal angle of reference beam
% 10.lambda: freespace recording wavelength
% 11.nu: index of refraction for write wavelength
% 12.s_r: binary; do simple (non-Zemax) reference beam
% 13.s_s: binary; do simple (non-Zemax) signal beam
% 14.n_1: # of current depth slice
% 15.Rr: 1x2 matrix of semimajor and semiminor axis of reference beam edge
% 16.Rs: 1x2 matrix of semimajor and semiminor axis of signal beam edge
% 17.do_offsets: binary; false is do idealized cylinder model
% 18.lambda_read: freespace probe wavelength
% 19.step_size_z: width of depth slice
% 20.delta_nu: change in index of refraction from recording
% 21.I_norm: normalized intensity for the beams at z
% 22.L1: structure of objective lens parameters; L1.f is focal length
% (that's all you need in the structure).
%%%%%%%%%%%%%%%%%%%%%%%%%%%%%%%%%%%%%%%%%%%%%%%%%%%%%%%%%%%%%%%%%%%%%%%%
%%%%%%%%%%%%%%%%%%%%%%%%%%%%%%%%%%%%%%%%%%%%%%%%%%%%%%%%%%%%%%%%%%%%%%%%

function obj = VH_object_fresnel(proc_data,X,Y,Nx,Ny,z,mux,theta_sig,...
    theta_ref,lambda,nu,s_r,s_s,n_1,Rr,Rs,do_offsets,lambda_read,...
    step_size_z,delta_nu,I_norm,L1)

% Initialize variables.
obj = zeros(Ny,Nx);
object_mask = false(Ny,Nx);
n_5 = 1;

% Create a unique interference pattern for each grating in the hologram
% object, then add the intensities from each.
for n = 1:mux

    % If the model uses offset beams, calculate the x-y coordinate of the
    % beam center.
    if do_offsets
        center_of_ref_beam = z*tan(theta_ref(n));
        center_of_signal_beam = z*tan(theta_sig);
    else
        center_of_ref_beam = 0;

```

```

        center_of_signal_beam = 0;
    end

    % Create the binary mask defining the edge of the interference pattern.
    const_mask = circap4(X,Y,[Rr(n,1),Rs(1)],...
        [Rr(n,2),Rs(2)], [0,0], [0,0],...
        [center_of_ref_beam,center_of_signal_beam]);

    % Update mask as beams are added.
    object_mask = object_mask | const_mask;

    % Generate the phase profile for the reference beam.
    if s_r
        Es = exp(i*2*pi/lambda*nu(1)*(cos(theta_ref(n))*z + ...
            sin(theta_ref(n)).*(X)));
    else
        Es = VHI_interp_wfm(proc_data.ref(n).wfm{n_1}(:, :),Nx,Ny,z,...
            theta_ref(n),lambda,nu(1),X);
    end

    n_5 = n_5 + 1;

    % Generate the phase profile for the signal beam.
    if s_s
        if L1.mux_def(n)
            Er = defocused_plane_wave(X,Y,z,...
                L1.mux_def(n),lambda*nu(1),theta_sig,L1.f);
        else
            Er = exp(i*2*pi/lambda*nu(1)*(cos(theta_sig)*z + ...
                sin(theta_sig).*(X)));
        end
    else
        Er = VHI_interp_wfm(proc_data.sig(n).wfm{n_1}(:, :),Nx,Ny,z,...
            theta_sig,lambda,nu(1),X);
    end

    n_5 = n_5 + 1;

    % Create interference pattern.
    obj(const_mask) = obj(const_mask) + ...
        (2+(Es(const_mask).*conj(Er(const_mask)))+...
        Er(const_mask).*conj(Es(const_mask)))/.4;

end

% Generate phase object function.
obj = object_mask.*exp(obj*i*2*pi*nu(2)/lambda_read*step_size_z*delta_nu*I_norm);

return;

%%%%%%%%%%%%%%%%%%%%%%%%%%%%%%%%%%%%%%%%%%%%%%%%%%%%%%%%%%%%%%%%%%%%%%%%
%%%%%%%%%%%%%%%%%%%%%%%%%%%%%%%%%%%%%%%%%%%%%%%%%%%%%%%%%%%%%%%%%%%%%%%%
% generate_VH_object_files.m
% function .m file
% Jonathan M. Watson 3/10/2008
%
% This function is used to generate the probe beam data file read by
% process_separate_VH_data_files.m.
%
% Inputs:
% 1. stand_alone_mode: binary; operate this function inside of a loop
% 2. probe_config: set to one.
% 3. L1_defocus: set to zero.
% 4. Nz: number of discrete hologram axial slices
% 5. do_offsets: binary; false is the idealized cylinder model
%%%%%%%%%%%%%%%%%%%%%%%%%%%%%%%%%%%%%%%%%%%%%%%%%%%%%%%%%%%%%%%%%%%%%%%%
%%%%%%%%%%%%%%%%%%%%%%%%%%%%%%%%%%%%%%%%%%%%%%%%%%%%%%%%%%%%%%%%%%%%%%%%

```

```

function generate_VH_object_files(stand_alone_mode,probe_config,L1_defocus,Nz,do_offsets)

%% Initialization Code --
% This should be done a single time for each batch on the local system,
% then provided as a data file for the individual processors.

if stand_alone_mode
    addpath('C:\MDO\modules\MZDDE\');
    zDDEstart;
    zDDEinit;
    pause(0.1);
end

%% Load simulation parameters and perform initial calculations.
load_parameters;
VHI_init_obj;
lens_data;
VHI_do_geometry;

%% Init + Object Generation

% Calculate the centers of each block in pupil coordinates.
[blk.center_x,blk.center_y] = ...
    meshgrid((-blk.Nx/2+.5):(blk.Nx/2-.5))*(Nx)*dxpp,...
    ((-blk.Ny/2+.5):(blk.Ny/2-.5))*(Ny)*dxpp);
blk.center      = [reshape(blk.center_x,blk.N,1),reshape(blk.center_y,blk.N,1)];
blk.R           = sqrt(sum(blk.center.^2,2));

% Calculate the positions of the block corners.
blk.crnrs      = [blk.center(:,1)-(Nx/2*dxpp),blk.center(:,1)+(Nx/2-1)*dxpp),...
    blk.center(:,2)-(Ny/2*dxpp),blk.center(:,2)+(Ny/2-1)*dxpp];
blk.N_use = blk.N;
blk.empty = [];

clear('edge_ref_x','edge_ref_y','n_3');

blk.valid(1:blk.N) = 1:blk.N;
blk.center(blk.empty,:) = [];
blk.R(blk.empty) = [];
blk.crnrs(blk.empty,:) = [];

%% generate wavefront data files

N_procs = blk.N_use;
n_1 = 0;

% Get the raw wavefront map from Zemax for the reference and signal beams.
for n_2 = 1:mux
    if ~simple_sig
        do_reference = 0;
        sig_data(:, :, n_2) =
VHI_get_const_wfm(n_2,nu(1),parax_loc_sig,signal_filename,theta(2)/D2R,do_reference);
    end
    if ~simple_ref
        do_reference = 1;
        ref_data(:, :, n_2) =
VHI_get_const_wfm(n_2,nu(1),parax_loc_ref,reference_filename,theta(1)/D2R,do_reference);
    end
end

% Convert recording angles from external to internal.
theta = asin(sin(theta)/nu(1));

% Step through each depth plane that will be calculated.
for z = -(Nz-1)/2:(Nz-1)/2

```

```

n_1 = n_1 + 1;
zpp = z*step_size_z;

n_5 = 1;
for n_2 = 1:mux
    if ~simple_ref
        do_reference = 1;
        [ref_wfm{n_2}, small_dx_obj(n_5), center_pt_obj(:, :, n_5)] = ...
            VHI_process_wfm(ref_data(:, :, n_2), zero_pad_ref(n_2), ...
                Rx, blk.Nx, blk.Ny, reference_angle(n_2), zpp, do_offsets);
    end
    n_5 = n_5 + 1;
    if ~simple_sig
        do_reference = 0;
        [sig_wfm{n_2}, small_dx_obj(n_5), center_pt_obj(:, :, n_5)] = ...
            VHI_process_wfm(sig_data(:, :, n_2), zero_pad_sig, ...
                Rx, blk.Nx, blk.Ny, theta(2), zpp, do_offsets);
    end
    n_5 = n_5 + 1;
end

% Store the wfm blocks in appropriate data structures.
for n_4 = 1:N_procs
    for n_2 = 1:mux
        if ~simple_ref
            processor_data(n_4).ref(n_2).wfm{n_1}(:, :) = ...
                ref_wfm{n_2}(:, :, blk.valid(n_4));
        else
            processor_data(n_4).ref = [];
        end
        if ~simple_sig
            processor_data(n_4).sig(n_2).wfm{n_1}(:, :) = ...
                sig_wfm{n_2}(:, :, blk.valid(n_4));
        else
            processor_data(n_4).sig = [];
        end
    end
end

disp(['Layer ', num2str(n_1), ' complete']);

end

clear('mask', 'ref_wfm', 'sig_wfm', 'ewald_sphere');

%% Save data.
for n_4 = 1:N_procs
    proc_data = processor_data(n_4);
    save(['VH_object_data_', num2str(n_4), '.mat'], 'proc_data');
end
clear('processor_data', 'proc_data');
for n_4 = 1:N_procs
    save(['VH_object_data_', num2str(n_4), '.mat'], '-append');
end
save('VH_header.mat', 'N_procs', 'decimate_cpus', 'Mpx', 'Mpy');
save('Radius.mat', 'Rx', 'Ry');
fclose('all');

%%%%%%%%%%%%%%%%%%%%%%%%%%%%%%%%%%%%%%%%%%%%%%%%%%%%%%%%%%%%%%%%%%%%%%%%
%%%%%%%%%%%%%%%%%%%%%%%%%%%%%%%%%%%%%%%%%%%%%%%%%%%%%%%%%%%%%%%%%%%%%%%%
% generate_VH_probe_files.m
% function .m file
% Jonathan M. Watson 3/10/2008
%
```

```

% This function is used to generate the probe beam data file read by
% process_separate_VH_data_files.m.
%
% Inputs:
% 1. stand_alone_mode: binary; operate this function inside of a loop
% 2. probe_config: select a lateral displacement of the probe point in the
% Zemax lens file. Create the lens file with probe displacements as
% separate field points along y.
% 3. L1_defocus: defocus of the probe point
% 4. Nz: number of discrete hologram axial slices
% 5. dot_radius: semiminor axis of probe beam apodization
% 6. do_offsets: binary; false is the idealized cylinder model
% 7. angle_2_change: change of angle for the probe beam in radians
%%%%%%%%%%%%%%%%%%%%%%%%%%%%%%%%%%%%%%%%%%%%%%%%%%%%%%%%%%%%%%%%%%%%%%%%

function generate_VH_probe_files(stand_alone_mode,probe_config,L1_defocus,...
    Nz,dot_radius,do_offsets,angle_2_change)

%% Initialization Code --
% This should be done a single time for each batch on the local system,
% then provided as a data file for the individual processors.

if stand_alone_mode
    addpath('C:\MDO\modules\MZDDE\');
    zDDEStart;
    zDDEInit;
    pause(0.1);
end

load('Radius.mat');

%% Load simulation parameters and perform initial calculations.
load_parameters;
VHI_init_probe;
lens_data;
VHI_do_geometry;

%% Init + Object Generation

% Calculate the centers of each block in pupil coordinates.
[blk.center_x,blk.center_y] = ...
    meshgrid((-blk.Nx/2+.5):(blk.Nx/2-.5))*(Nx)*dxpp,...
            ((-blk.Ny/2+.5):(blk.Ny/2-.5))*(Ny)*dxpp);
blk.center = [reshape(blk.center_x,blk.N,1),reshape(blk.center_y,blk.N,1)];
blk.R      = sqrt(sum(blk.center.^2,2));

% Calculate the positions of the block corners.
blk.crnrs = [blk.center(:,1)-(Nx/2*dxpp),blk.center(:,1)+(Nx/2-1)*dxpp],...
            blk.center(:,2)-(Ny/2*dxpp),blk.center(:,2)+(Ny/2-1)*dxpp];
blk.N_use = blk.N;
blk.empty = [];

clear('edge_ref_x','edge_ref_y','n_3');

blk.valid(1:blk.N) = 1:blk.N;
blk.center(blk.empty,:) = [];
blk.R(blk.empty) = [];
blk.crnrs(blk.empty,:) = [];

%% generate wavefront data files

N_procs = blk.N_use;
n_1 = 0;

% Get the raw wavefront map from Zemax.
wfm = VHI_get_probe_wfm(lambda,lambda_read,L1,...
    (bragg_angle + angle_2_change)/D2R,nu(2),probe_filename,...

```

```

    parax_loc_sig,probe_config);

% Step through each depth plane that will be calculated.
for z = -(Nz-1)/2:(Nz-1)/2
    n_1 = n_1 + 1;
    zpp = z*step_size_z;

    % If we let Zemax force a wavefront map instead of generating it
    % manually, then break the wfm apart into individual sections for each
    % block.
    if ~simple_probe
        [probe_wfm, small_dx_probe, center_pt_probe] = ...
            VHI_process_wfm(wfm,zero_pad_prb,Rx,blk.Nx,...
                blk.Ny,probe_angle,zpp,do_offsets);
    end

    % Store the wfm blocks in appropriate data structures.
    for n_4 = 1:N_procs
        if ~simple_probe
            processor_data(n_4).probe.wfm{n_1}(:, :) = probe_wfm(:, :, blk.valid(n_4));
        else
            processor_data(n_4).probe = [];
        end
    end
end

end

clear('mask','probe_wfm','ewald_sphere','blk');

%% Save data.
for n_4 = 1:N_procs
    probe_data = processor_data(n_4).probe;
    save(['VH_probe_data_',num2str(n_4),'.mat'],'probe_data');
end
clear('processor_data','probe_data');
for n_4 = 1:N_procs
    save(['VH_probe_data_',num2str(n_4),'.mat'],'-append');
end
fclose('all');

%%%%%%%%%%%%%%%%%%%%%%%%%%%%%%%%%%%%%%%%%%%%%%%%%%%%%%%%%%%%%%%%%%%%%%%%
%%%%%%%%%%%%%%%%%%%%%%%%%%%%%%%%%%%%%%%%%%%%%%%%%%%%%%%%%%%%%%%%%%%%%%%%
% VHI_get_const_wfm.m
% function .m file
% Jonathan M. Watson 3/10/2008
%
% This function is used to generate the wavefront map with Zemax that will
% be used by generate_VH_obj_files.m. The output is a matrix of data
% provided by Zemax.
%
% Inputs:
% 1. zmx_config: configuration # defining the specific grating in mux
% 2. nu: refractive index at construction wavelength
% 3. parax_loc: surface number of paraxial lens for afocal wfm calculation
% 4. file_name: string; name of Zemax lens file
% 5. beam_angle: angle of probe beam
% 6. do_reference: binary; true if calculating reference beam wfm
%%%%%%%%%%%%%%%%%%%%%%%%%%%%%%%%%%%%%%%%%%%%%%%%%%%%%%%%%%%%%%%%%%%%%%%%
%%%%%%%%%%%%%%%%%%%%%%%%%%%%%%%%%%%%%%%%%%%%%%%%%%%%%%%%%%%%%%%%%%%%%%%%

function [wave] =
VHI_get_const_wfm(zmx_config,nu,parax_loc,file_name,beam_angle,do_reference)

% Load the lens file into Zemax
zLoadFile(file_name);
pause(0.25)
zPushLens;

```



```

zGetRefresh;
pause(0.25)

% If the reference beam is being calculated, then the mux parameter is the
% field point, otherwise the mux parameter is a configuration setting
% different defocus positions for the point source in the signal arm.
if do_reference
    FieldData = zGetField(zmx_config);
    zSetField(1,FieldData(1),FieldData(2),1,0,0,0,0);
else
    zSetConfig(zmx_config);
end

% Set correct focal length for paraxial lens in PMMA.
zSetSurfaceParameter(parax_loc,1,zGetSurfaceData(parax_loc,3)/nu);

% Rotate the hologram to the recording angle.
zSetSurfaceParameter(parax_loc-2,3,beam_angle);

% Update the lens file.
zPushLens;
zGetRefresh;
pause(0.25)

% Get the wfm from Zemax, and check the validity of the data.
invalid_wfm = 1;
while invalid_wfm
    zGetTextFile('C:\MDO\projects\strawman_map3.wfm', 'wfm', ...
        'C:\MDO\projects\settings.txt', 0);
    pause(7)
    zmxWaveMap = ReadZemaxWaveMap('C:\MDO\projects\strawman_map3.wfm');
    if ~isempty(zmxWaveMap.data) && all(size(zmxWaveMap.data)==zmxWaveMap.grid)
        invalid_wfm = 0;
    end
end
wave = zmxWaveMap.data;

% Reset lens file to original state.
if do_reference
    zSetField(1,0,0,1,0,0,0,0);
else
    zSetConfig(1);
end
zPushLens;
zGetRefresh;

return;

%%%%%%%%%%%%%%%%%%%%%%%%%%%%%%%%%%%%%%%%%%%%%%%%%%%%%%%%%%%%%%%%%%%%%%%%
%%%%%%%%%%%%%%%%%%%%%%%%%%%%%%%%%%%%%%%%%%%%%%%%%%%%%%%%%%%%%%%%%%%%%%%%
% VHI_get_probe_wfm.m
% function .m file
% Jonathan M. Watson 3/10/2008
%
% This function is used to generate the wavefront map with Zemax that will
% be used by generate_VH_probe_files.m. The output is a matrix of data
% provided by Zemax.
%
% Inputs:
% 1. lambda: external construction wavelength
% 2. lambda_rd: external probe wavelength
% 3. L1: data structure for objective lens
% 4. beam_angle: angle of probe beam
% 5. nu: refractive index at probe wavelength
% 6. file_name: string; name of Zemax lens file
% 7. parax_loc: surface number of paraxial lens for afocal wfm calculation

```

```

% 8. zmx_config: field point # used for probe beam
%%%%%%%%%%%%%%%%%%%%%%%%%%%%%%%%%%%%%%%%%%%%%%%%%%%%%%%%%%%%%%%%%%%%%%%%

function [wave] = VHI_get_probe_wfm(lambda,lambda_rd,L1,beam_angle,nu,...
    file_name,parax_loc,zmx_config)

% Load the lens file into Zemax.
zLoadFile(file_name);
pause(0.25)
zPushLens;
zGetRefresh;
pause(0.25)

% Use the field point desired for off-axis point sources, and defocus the
% objective to the level desired in the L1 structure.
zSetConfig(1);
zSetWave(1, lambda_rd, 1);
FieldData = zGetField(zmx_config);
zSetField(1,FieldData(1),FieldData(2),1,0,0,0,0);
zSetSurfaceData(0, 3, (L1.f + L1.defocus)*1e-3);

% Set correct focal length for paraxial lens in PMMA.
zSetSurfaceParameter(parax_loc,1,zGetSurfaceData(parax_loc,3)/nu);

% Rotate the hologram to the probe beam angle.
zSetSurfaceParameter(parax_loc-2,3,beam_angle);

% Update the lens file.
zPushLens;
zGetRefresh;
pause(0.25)

% Get the wfm from Zemax, and check the validity of the data.
invalid_wfm = 1;
while invalid_wfm
    zGetTextFile('C:\MDO\projects\strawman_map3.wfm', 'wfm',
'C:\MDO\projects\settings.txt', 0);
    pause(5);
    zmxWaveMap = ReadZemaxWaveMap('C:\MDO\projects\strawman_map3.wfm');
    if ~isempty(zmxWaveMap.data) && all(size(zmxWaveMap.data)==zmxWaveMap.grid)
        invalid_wfm = 0;
    end
end
wave = zmxWaveMap.data;

% Reset lens file to original state.
zSetSurfaceData(0, 3, L1.f*1e-3);
zSetWave(1, lambda, 1);
zSetField(1,0,0,1,0,0,0,0);
zPushLens;
zGetRefresh;

return;

%%%%%%%%%%%%%%%%%%%%%%%%%%%%%%%%%%%%%%%%%%%%%%%%%%%%%%%%%%%%%%%%%%%%%%%%

%%%%%%%%%%%%%%%%%%%%%%%%%%%%%%%%%%%%%%%%%%%%%%%%%%%%%%%%%%%%%%%%%%%%%%%%
% VHI_init_obj.m
% script .m file
% Jonathan M. Watson 3/10/2008
%
% This script performs some of the initial calculations necessary before
% Zemax can be asked to provide a wavefront map. Here, some of the
% simulation parameters are calculated directly from the lens file. This
% file is used for the recording optics.
%%%%%%%%%%%%%%%%%%%%%%%%%%%%%%%%%%%%%%%%%%%%%%%%%%%%%%%%%%%%%%%%%%%%%%%%

```

```

% Convert angles to radians.
D2R      = pi/180;
theta    = theta.*D2R;

%% Signal Beam

% Load the lens file for the signal arm.
zLoadFile(signal_filename);
zPushLens;
zGetRefresh;
pause(0.1);

% Get the recording wavelength.
lambda    = zGetWave(1);
lambda(2) = [];
lambda_read = zGetWave(2);
lambda_read(2) = [];
mu = lambda_read/lambda;

% The number of configurations in the signal arm determines the number of
% multiplex gratings will be recorded.
config_data = zGetConfig;
mux = config_data(2);

% Find out if field displacements are in position or angle.
field_type_sig = zGetField(0);
zSetConfig(1);

% Get data for all surfaces.
SURFS = zsGetSurfaceDataVector;
n_SURFS = length(SURFS);

s_match = 0;
parax_loc_sig = n_SURFS;

% Find the location of the paraxial lens that allows Zemax to provide an
% afocal wavefront map.
while ~s_match
    if strcmp('PARAXIAL',SURFS(parax_loc_sig).type)
        s_match = 1;
    end
    parax_loc_sig = parax_loc_sig - 1;
    if parax_loc_sig < 0
        error('no paraxial lens in system; no afocal solution!');
    end
end

% Find the distance from the back of the last real lens.
BFD_afoc = zGetSurfaceData(parax_loc_sig-3,3);

% Get the semiminor radius of the beam spot.
R_sig(2) = zGetSurfaceData(parax_loc_sig-1,5);

% Rotate the hologram to the recording angle.
zSetSurfaceParameter(parax_loc_sig-2,3,theta(2)/D2R);
zPushLens;
zGetRefresh;

% Get the semimajor radius of the beam spot.
R_sig(1) = zGetSurfaceData(parax_loc_sig-1,5);

%% Reference Beam

% Load the lens file for the signal arm.
zLoadFile(reference_filename);
zPushLens;
zGetRefresh;

```

```

pause(0.1);

% Get data for all surfaces.
SURFS = zsGetSurfaceDataVector;
n_SURFS = length(SURFS);

% Find the location of the paraxial lens that allows Zemax to provide an
% afocal wavefront map.
s_match = 0;
parax_loc_ref = n_SURFS;
while ~s_match
    if strcmp('PARAXIAL',SURFS(parax_loc_ref).type)
        s_match = 1;
    end
    parax_loc_ref = parax_loc_ref - 1;
    if parax_loc_ref < 0
        error('no paraxial lens in system; no afocal solution');
    end
end

% Find the distance from the back of the last real lens.
BFD_ref_afoc = zGetSurfaceData(parax_loc_ref-3,3);

% Get the semiminor radius of the beam spot.
Ry_ref = zGetSurfaceData(parax_loc_ref-1,5);

% Find out if field displacements are in position or angle.
field_type_ref = zGetField(0);

% For each field, trace the chief ray through the optics and calculate the
% angle that the chief ray makes with the optical axis. This determines the
% change in recording angle.
for n_34 = 1:mux
    FieldData_ref = zGetField(n_34);
    if ~field_type_ref(1)
        trace_data = zGetTraceDirect(1,0,0,parax_loc_ref-
2,0,0,0,0,sind(FieldData_ref(2)),cosd(FieldData_ref(2)));
    else
        trace_data = zGetTraceDirect(1,0,0,parax_loc_ref-2,0,FieldData_ref(2),0,0,0,1);
    end
    reference_angle(n_34) = asin(sin(theta(1)) +
atan(trace_data(7)/trace_data(8))/nu(1));
end

% Reset the lens file.
for n_35 = 1:mux
    zSetField(n_35,0,0,1,0,0,0,0,0);
end
zPushLens;
zGetRefresh;

% Get the semimajor radius of the beam spot for each multiplexed reference
% beam.
for n_36 = 1:mux
    zSetSurfaceParameter(parax_loc_ref-2,3,asin(sin(reference_angle(n_36))*nu(1))/D2R);
    zPushLens;
    zGetRefresh;
    R_ref(n_36,:) = [zGetSurfaceData(parax_loc_ref-1,5),Ry_ref];
end

%% Simulation Boundary

% Determine the location where the signal and reference beams intersect.
z_intersect = (R_ref(:,1)-R_sig(1))./(tan(theta(2))-tan(theta(1)));

% find the maximum extent of the interference pattern in pupil coordinates.
if any(z_intersect > -(L/2*1e-3))

```

```

    Rx = R_sig(1) + max(z_intersect)*tan(theta(2));
else
    Rx = min([max(R_ref(:,1))-L/2*1e-3*tan(theta(1)),R_sig(1)-L/2*1e-3*tan(theta(2))]);
end

Ry = min([R_ref(:,2);R_sig(2)]);

clear('SURFS');

% Determine the minimum amount of zero padding for each beam that allows
% the full object to be simulated.
zero_pad_ref = (Rx-R_ref(:,1))./Rx;
zero_pad_sig = (Rx-R_sig(1))/Rx;

% Convert to microns.
R_ref = R_ref.*1e3;
R_sig = R_sig*1e3;
Rx = Rx*1e3;
Ry = Ry*1e3;

%%%%%%%%%%%%%%%%%%%%%%%%%%%%%%%%%%%%%%%%%%%%%%%%%%%%%%%%%%%%%%%%%%%%%%%%
%%%%%%%%%%%%%%%%%%%%%%%%%%%%%%%%%%%%%%%%%%%%%%%%%%%%%%%%%%%%%%%%%%%%%%%%
% VHI_init_probe.m
% script .m file
% Jonathan M. Watson 3/10/2008
%
% This script performs some of the initial calculations necessary before
% Zemax can be asked to provide a wavefront map. Here, some of the
% simulation parameters are calculated directly from the lens file. This
% file is used for the probe optics.
%%%%%%%%%%%%%%%%%%%%%%%%%%%%%%%%%%%%%%%%%%%%%%%%%%%%%%%%%%%%%%%%%%%%%%%%
%%%%%%%%%%%%%%%%%%%%%%%%%%%%%%%%%%%%%%%%%%%%%%%%%%%%%%%%%%%%%%%%%%%%%%%%

% Convert angles to radians.
D2R      = pi/180;
theta    = theta.*D2R;

%% Probe Beam

% Load the lens file for the probe optics.
zLoadFile(probe_filename);
zPushLens;
zGetRefresh;
pause(0.1);

% Get the probe wavelength.
lambda      = zGetWave(1);
lambda(2)   = [];
lambda_read = zGetWave(2);
lambda_read(2) = [];
mu = lambda_read/lambda;

% Find out if field displacements are in position or angle.
config_data = zGetConfig;
field_type_sig = zGetField(0);
zSetConfig(1);
FieldData_Orig = zGetField(1);

% Get the field data for the probe beam that will be used.
FieldData = zGetField(probe_config);
zSetField(1,FieldData(1),FieldData(2),1,0,0,0,0);

% Store the original external angle.
theta_orig = theta(2);

% Convert external angle to internal.
theta = asin(sin(theta)/nu(1));

```

```

zPushLens;
zGetRefresh;

% Get data for all surfaces.
SURFS = zGetSurfaceDataVector;
n_SURFS = length(SURFS);

% Find the location of the paraxial lens that allows Zemax to provide an
% afocal wavefront map.
s_match = 0;
parax_loc_sig = n_SURFS;
while ~s_match
    if strcmp('PARAXIAL',SURFS(parax_loc_sig).type)
        s_match = 1;
    end
    parax_loc_sig = parax_loc_sig - 1;
    if parax_loc_sig < 0
        error('no paraxial lens in system; no afocal solution');
    end
end

% Find the distance from the back of the last real lens.
BFD_afoc = zGetSurfaceData(parax_loc_sig-3,3);

% For the desired field, trace the chief ray through the optics and
% calculate the angle that the chief ray makes with the optical axis.
if ~field_type_sig(1)
    trace_data = zGetTraceDirect(2,0,0,parax_loc_sig-2,0,0,0,0,...
        sind(FieldData(2)),cosd(FieldData(2)));
else
    trace_data = zGetTraceDirect(2,0,0,parax_loc_sig-2,0,FieldData(2),0,0,0,1);
end

% Calculate the Ewald (K) sphere solution for the angle required for
% Bragg-matched reconstruction. All angle offsets are defined with respect
% to this angle.
if do_conj
    d_vector = [cos(theta(2))-cos(theta(1)), sin(theta(2))-sin(theta(1))].*...
        nu(1)/lambda;
else
    d_vector = [cos(theta(1))-cos(theta(2)), sin(theta(1))-sin(theta(2))].*...
        nu(1)/lambda;
end
ewald_sphere = @(x) (d_vector(1)+cos(x)*nu(2)/lambda_read)^2+(d_vector(2)+...
    sin(x)*nu(2)/lambda_read)^2-(nu(2)/lambda_read)^2;
bragg_angle = asin(sin(fzero(ewald_sphere,theta_orig))*nu(2));
probe_angle = asin(sin(bragg_angle + angle_2_change + ...
    atan(trace_data(7)/trace_data(8))/nu(2));

% Get the semiminor radius of the beam spot.
R_prb(2) = zGetSurfaceData(parax_loc_sig-1,5)*1e3;

% Rotate the hologram to the recording angle.
zSetSurfaceParameter(parax_loc_sig-2,3,(bragg_angle + angle_2_change)/D2R);
zPushLens;
zGetRefresh;

% Get the semimajor radius of the beam spot.
R_prb(1) = zGetSurfaceData(parax_loc_sig-1,5)*1e3;

% Determine the minimum amount of zero padding for this beam that allows
% the full object to be simulated.
zero_pad_prb = (Rx-R_prb(1))/Rx;

%%%%%%%%%%%%%%%%%%%%%%%%%%%%%%%%%%%%%%%%%%%%%%%%%%%%%%%%%%%%%%%%%%%%%%%%
%%%%%%%%%%%%%%%%%%%%%%%%%%%%%%%%%%%%%%%%%%%%%%%%%%%%%%%%%%%%%%%%%%%%%%%%

```

```

% VHI_interp_wfm.m
% function .m file
% Jonathan M. Watson 3/10/2008
%
% This function has numerous inputs, but only one output; the phase front
% generated by Zemax interpolated for the correct dimensions of each block.
%
% Inputs:
% 1. wfm: matrix portion of the Zemax wavefront map assigned to this block
% 2. Nx: size of the non-zero data along x
% 3. Ny: size of the non-zero data along y
% 4. z: axial coordinate in pupil space
% 5. theta: internal angle of beam
% 6. lambda: freespace recording wavelength
% 7. nu: index of refraction for write wavelength
% 8. X: matrix of x coordinates in pupil space
%%%%%%%%%%%%%%%%%%%%%%%%%%%%%%%%%%%%%%%%%%%%%%%%%%%%%%%%%%%%%%%%%%%%%%%%

function wave = VHI_interp_wfm(wfm,Nx,Ny,z,theta,lambda,nu,X)

% We want Matlab to ignore the NaNs here.
warning('off','MATLAB:chckxy:IgnoreNaN');

% Find the portions of the wavefront.
find_mask = false(size(wfm));
find_mask(abs(wfm) < eps) = true;

% Initialize the wave function.
wave = zeros(size(X));

% Set the zeros of the wfm to NaNs. Even for flat wavefronts, Zemax
% provides a wavefront displacement value larger than eps.
wfm(find_mask) = NaN;

% Convert exterior wavelength to interior.
lambda = lambda/nu;

% Convert wfm to distance.
wfm = wfm.*lambda;

% Calculate interpolation step size.
non_zeros_x = size(wfm,2);
delta_interp_x = (non_zeros_x-1)/(Nx-1);
non_zeros_y = size(wfm,1);
delta_interp_y = (non_zeros_y-1)/(Ny-1);
xS = 1:delta_interp_x:non_zeros_x;
yS = (1:delta_interp_y:non_zeros_y)';

% Interpolate wfm
i_wfm = interp2(wfm,xS,yS,'*linear');

% Create binary mask for the interpolated mask to reject NaNs.
out_mask = true(size(i_wfm));
out_mask(isnan(i_wfm)) = false;

% Create wavefront function.
wave(out_mask) = exp(((i_wfm(out_mask) + z)*cos(theta) +...
    X(out_mask)*sin(theta))*(i*2*pi/lambda));

return;

%%%%%%%%%%%%%%%%%%%%%%%%%%%%%%%%%%%%%%%%%%%%%%%%%%%%%%%%%%%%%%%%%%%%%%%%
%%%%%%%%%%%%%%%%%%%%%%%%%%%%%%%%%%%%%%%%%%%%%%%%%%%%%%%%%%%%%%%%%%%%%%%%
% VHI_process_wfm.m
% function .m file
% Jonathan M. Watson 3/10/2008

```

```

%
% This function takes a wavefront map from Zemax and calculates the proper
% dimensions of the wfm for each block. This function then cuts the wfm
% into the appropriate pieces for each block.
%
% Outputs:
% 1. wave: sectioned wavefront map.
% 2. delta_x: calculated step size from the Zemax wfm.
% 3. center_pt: location of the center of each wfm section in pupil
% coordinates.
%
% Inputs:
% 1. wfm: matrix of wavefront topology from Zemax
% 2. zero_pad: required amount of zero padding to simulate the entire
% object.
% 3. Rx: semimajor radius of the beam spot
% 4. N_x: number of blocks in the domain over x
% 5. N_y: number of blocks in the domain over y
% 6. beam_angle: beam angle
% 7. z: pupil axial coordinate of this hologram slice
% 8. do_offsets: binary; false if idealized cylindrical geometry
%%%%%%%%%%%%%%%%%%%%%%%%%%%%%%%%%%%%%%%%%%%%%%%%%%%%%%%%%%%%%%%%%%%%%%%%
function [wave, delta_x, center_pt] = VHI_process_wfm(wfm,zero_pad,Rx,N_x,...
    N_y,beam_angle,z,do_offsets)

% Find the size of the Zemax wfm, usually 512x512.
wfm_dims = size(wfm);

% Find the dimensions of the wfm that contain data
if do_offsets
    non_zeros_x = find(wfm(:,wfm_dims(2)/2));
    non_zeros_y = find(wfm(wfm_dims(1)/2,:));
else
    non_zeros_x = 1:wfm_dims(2);
    non_zeros_y = 1:wfm_dims(1);
end

% Trim the wfm to new dimensions M_x and M_y.
wfm = wfm(non_zeros_x,non_zeros_y);
M_x = length(non_zeros_x);
M_y = length(non_zeros_y);

% Find the dimensions of the final wfm.
zero_pad_dims = 2*round(zero_pad*M_x/2)+[M_x,M_y];

% Find the offset of the beam center if not using idealized model.
if do_offsets
    x_offset = -round(z*tan(beam_angle)/(Rx/(zero_pad_dims(1)/2)));
else
    x_offset = 0;
end

if zero_pad_dims(1) >= M_x

    % zero-pad the full wfm matrix
    wfm_p = padarray(wfm,[(zero_pad_dims(1)-M_x)/2,(zero_pad_dims(1)-M_x)/2]);
    [M_x,M_y] = size(wfm_p);
    wfm_s = zeros(M_x,M_y);

    % Generate a new wfm matrix with shifted indices.
    if x_offset >= 0
        left_edge = M_x - x_offset;
        right_edge = 0;
        wfm_s(1:left_edge,:) = wfm_p(x_offset+1:end,:);
    else
        right_edge = 1 - x_offset;

```



```

        left_edge = 0;
        wfm_s(right_edge:end,:) = wfm_p(1:end+x_offset,:);
    end

    wfm_p = wfm_s;

else
    wfm_s = zeros(size(wfm));

    % Generate a new wfm matrix with shifted indices.
    if x_offset >= 0
        left_edge = M_x - x_offset;
        right_edge = 0;
        wfm_s(1:left_edge,:) = wfm(x_offset+1:end,:);
    else
        right_edge = 1 - x_offset;
        left_edge = 0;
        wfm_s(right_edge:end,:) = wfm(1:end+x_offset,:);
    end

    % Now trim the shifted matrix to the proper size.
    wfm_p = wfm_s;
    clip_length = (M_x-zero_pad_dims(1))/2;
    wfm_p(end-(clip_length+1):end,:) = [];
    wfm_p(:,end-(clip_length+1):end) = [];
    wfm_p(1:(clip_length-1),:) = [];
    wfm_p(:,1:(clip_length-1)) = [];

end

[M_x,M_y] = size(wfm_p);
non_zeros_x = 1:M_x;
non_zeros_y = 1:M_y;

% Solve for the small amount of zero padding necessary to provide the
% discretization of the blocks with a single pixel of overlap between each
% to ensure continuity in the solution.
beta_x = ceil((M_x+2*(N_x-1))/N_x)*N_x-(M_x+2*(N_x-1));
small_dim_x = (M_x+2*(N_x-1)+beta_x)/N_x;
left_pad = floor(beta_x/2);
beta_y = ceil((M_y+2*(N_y-1))/N_y)*N_y-(M_y+2*(N_y-1));
small_dim_y = (M_y+2*(N_y-1)+beta_y)/N_y;
top_pad = floor(beta_y/2);

% Pad the entire Zemax wfm to the appropriate amount.
i_wfm = zeros(M_y+beta_y,M_x+beta_x);
i_wfm(1+top_pad:top_pad+M_y,1+left_pad:left_pad+M_x) = ...
    wfm_p(non_zeros_x,non_zeros_y)';

% Cut the wavefront map into sections for each block number, and store in a
% 3-D matrix.
n_3 = 0;
for n_1 = 1:N_x
    for n_2 = 1:N_y
        n_3 = n_3 + 1;
        wave(:, :, n_3) = i_wfm((1:small_dim_y-1)+(small_dim_y-2)*(n_2-1), ...
            (1:small_dim_x-1)+(small_dim_x-2)*(n_1-1));
        center_pt(n_3, :) = [small_dim_y/2+(small_dim_y-2)*(n_2-1)-M_y/2, ...
            small_dim_x/2+(small_dim_x-2)*(n_1-1)-M_x/2];
    end
end

% Estimate the Zemax step size and the center point of each block.
delta_x = Rx/(M_x/2);
center_pt = center_pt.*delta_x;

return

```

```

%%%%%%%%%%%%%%%%%%%%%%%%%%%%%%%%%%%%%%%%%%%%%%%%%%%%%%%%%%%%%%%%%%%%%%%%
%%%%%%%%%%%%%%%%%%%%%%%%%%%%%%%%%%%%%%%%%%%%%%%%%%%%%%%%%%%%%%%%%%%%%%%%
% VHI_do_geometry.m
% script .m file
% Jonathan M. Watson 3/10/2008
%
% This script performs some of the initial calculations necessary before
% Zemax can be asked to provide a wavefront map. Here, the geometric
% calculations are performed to determine the required number of blocks,
% block sizes, zero-padding, and domain dimensions.
%%%%%%%%%%%%%%%%%%%%%%%%%%%%%%%%%%%%%%%%%%%%%%%%%%%%%%%%%%%%%%%%%%%%%%%%

% Evanescent cutoff freq.
uEC      = nu(2)/lambda_read;

% Horizontal dimension of the whole domain.
Mx       = ceil(2*Rx/dxpp);

%% Work on the x-direction

% Initial guess of the number of blocks needed along x.
blk.Nx   = floor(block_ratio_x*ceil(2*Mx/Mpx)/2);

% Zero pad the entire domain slightly to make sure the blocks will each
% have the same number of elements.
while Mx/blk.Nx ~= round(Mx/blk.Nx)
    Mx = Mx + 1;
end

% Intermediate guess of the number of blocks needed along x.
blk.Nx   = floor(block_ratio_x*ceil(2*Mx/Mpx)/2);

while Mx/blk.Nx ~= round(Mx/blk.Nx)
    Mx = Mx + 1;
end

% Final guess of the number of blocks needed along x.
blk.Nx   = floor(block_ratio_x*ceil(2*Mx/Mpx)/2);

% Number of non-zero block values along x.
Nx       = Mx/blk.Nx;

% If the number of non-zeros must be larger than the requested block
% dimensions, something has gone wrong.
if Nx > Mpx
    error('Increase block ratio or block size.');
```

```

while My/blk.Ny ~= round(My/blk.Ny)
    My = My + 1;
end

% Intermediate guess of the number of blocks needed along y.
blk.Ny = floor(block_ratio_y*ceil(2*My/Mpy)/2);

% Zero pad the entire domain slightly to make sure the blocks will each
% have the same number of elements.
while My/blk.Ny ~= round(My/blk.Ny)
    My = My + 1;
end

% Final guess of the number of blocks needed along y.
blk.Ny = floor(block_ratio_y*ceil(2*My/Mpy)/2);

% Number of non-zero block values along y.
Ny = My/blk.Ny;

% If the number of non-zeros must be larger than the requested block
% dimensions, something has gone wrong.
if Ny > Mpy
    error('Increase block ratio or block size.');
```

```

end

% Adjust values to even numbers.
if Ny/2 ~= round(Ny/2)
    My = My + blk.Ny;
    blk.Ny = floor(block_ratio_y*ceil(2*My/Mpy)/2);
    Ny = My/blk.Ny;
end

% Adjust values to even numbers.
if Mpy/2 ~= round(Mpy/2)
    Mpy = Mpy+1;
end

%% Finish up.

% Total number of blocks.
blk.N = blk.Nx*blk.Ny;

% X and Y-freq. step.
du = 1/(Mpx*dxpp);
dv = 1/(Mpy*dxpp);

% delta_z
step_size_z = L/Nz;

% X and Y dimension of domain in pupil.
xpp_max = Mpx/2*dxpp;
ypp_max = Mpy/2*dxpp;

% Step size and domain dimensions in object space.
x_max = lambda_read*L1.f/(2*dxpp);
dx = lambda_read*L1.f/(2*xpp_max);
y_max = lambda_read*L1.f/(2*dxpp);
dy = lambda_read*L1.f/(2*ypp_max);

% Step size and domain dimensions in image plane.
xp_max = x_max*(-L2.f/L1.f);
d xp = dx*(-L2.f/L1.f);
yp_max = y_max*(-L2.f/L1.f);
d yp = dy*(-L2.f/L1.f);

%%%%%%%%%%%%%%%%%%%%%%%%%%%%%%%%%%%%%%%%%%%%%%%%%%%%%%%%%%%%%%%%%%%%%%%%%
```